Seismic Performance Evaluation Method of Wide Pile-Supported Wharfs Considering Kinematic and Inertial Forces

Christino Boyke Surya Permana

(Degree)
博士（工学）
(Date of Degree)
2023-09-25
(Date of Publication)
2025-12-17
(Resource Type)
doctoral thesis
(Report Number)
甲第8738号
(URL)
https://hdl.handle.net/20.500.14094/0100485922

Doctoral Dissertation

Seismic Performance Evaluation Method of Wide Pile-Supported Wharfs Considering Kinematic and Inertial Forces

(慣性力とキネマティック荷重を考慮した幅広桟橋の耐震性能照査法)

By

Christino Boyke Surya Permana

(July, 2023)

Graduate School of Engineering
Kobe University

Seismic Performance Evaluation Method of Wide Pile-Supported Wharfs Considering Kinematic and Inertial Forces

(慣性力とキネマティック荷重を考慮した幅広桟橋の耐震性能照査法)

Christino Boyke Surya Permana

Supervisor: Professor Takashi Nagao

A thesis submitted to the
Faculty of the Graduate School of Engineering
Kobe University in partial fulfillment of
the requirement for the degree of
DOCTOR OF PHILOSOPHY IN ENGINEERING

Graduate School of Engineering
Department of Civil Engineering
Kobe University
Kobe, Japan

July, 2023

ABSTRACT

In Indonesia, earthquakes have damaged port facilities and other infrastructure. The pile-supported wharf (PSW) is one of the most vulnerable port facilities to earthquake damage. Its seismic resistance should be carefully assessed to reduce the risk of seismic damage to a PSW. This research proposes a novel method for evaluating the seismic performance of PSW in Indonesia. A new seismic performance assessment for wharves using frame analysis (FA) that considers inertial force, kinematic force, and PSW damping coefficient is proposed to achieve this objective. This study suggested a method to calculate kinematic force using soil reaction from the P-Y curve in conjunction with soil displacement. This study also proposed using a 1D site-specific analysis in design practice for estimating the maximum soil displacement required to calculate the kinematic force. Through statistical processing, this study also suggested earthquake ground motions (EGMs) to design PSW in Indonesia. This research also compared the proposed EGMs to those in the Indonesian seismic code (SNI 1726).

EGM and Indonesian soil data were analyzed considering those mentioned above. Deconvolution analysis was used to assess the EGM occurrences in bedrock. The EGMs data were scaled to match peak ground acceleration comparable to the EGMs in the rock site class as specified by the SNI 1726. A seismic response analysis incorporating nonlinear characteristics of soil was performed, and 144 EGMs were obtained at port locations. Taking into account the variance in the derived EGMs, this research suggests site-specific EGMs for the seismic design of PSW. The difference between the proposed EGMs and those in the SNI 1726 is notable.

This research investigates the effect of ground displacement on the PSW with a mild slope. The study used finite element analysis (FEA) focusing on a wide PSW. The analysis is separated into two different scenarios. In the first scenario, the PSW was modeled without consideration for the slope of the soil, whereas in the second scenario, the slope was taken into account. This research also investigates the waveform period's influences on PSW's seismic response. Two waveforms with different duration were used. The analysis results revealed significant effects of soil slope displacement and waveform variations on the performance of PSW.

The Frame analysis (FA) method is acknowledged for its effectiveness and low requirements for computer resources. Nevertheless, compared to FEA, FA's ability to conduct a seismic performance assessment of PSWs is inadequate, especially its ability to consider kinematic force from ground displacement due to earthquakes. This research develops a two-dimensional (2D) FA method for analyzing PSW performance that considers both inertial and kinematic forces. Both FA and FEA were conducted, and the outcomes were compared. First, the spectral acceleration (SA) evaluation method for calculating inertial force was discussed. Using the SA evaluation result, an equation was proposed for estimating a damping coefficient based on a PSW's natural period and width. Next, the analysis focused on the PSW model considering the soil slope. The calculation method for obtaining kinematic force using ground displacement value in conjunction with the P-Y curve was proposed. This research also proposed a method to predict the soil slope displacement during an earthquake using 1D seismic response analysis. Using the suggested method and accounting for inertial and kinematic forces, the FA could produce bending moments of piles similar to those analyzed using FEA.

ACKNOWLEDGEMENT

I offer my most sincere gratitude to my supervisor Professor Takashi Nagao, for his guidance, enthusiasm, and encouragement. The opportunities he has afforded me throughout my studies, many of which go beyond the scope of this thesis, are helping me grow toward my goal. Gratefulness will never be enough to express my gratitude toward him.

I want to express my gratitude to my seniors at Marine Transportation Engineering Department ITS, especially Dr. Setyo Nugroho, Dr. Tri Achmadi, Dr. Firmanto Hadi, and Dr. IGN Sumanta Buana, for giving me examples, inspiring and motivating me to become a good researcher.

I would like to express my gratitude to Dr. Mudji Irmawan, Dr. Lamidi, and Dr. Andreas Bambang, the board of directors at PT. ITSC, which provided tremendous financial support during my study in Japan and provided engineering software to be used in this research.

I would like to acknowledge the member of Professor Nagao's Laboratory, especially Afif Navir, for the great atmosphere and shared the same sense of duty during my study.

I want to thank Rosita Ardila, my wife, my best friend, and my life partner, for the love, support, and years of her life she has been giving me and for taking care of the love of our life, Abril and Bisma.

Last but not least, I would like to thank my family and friends for their endless love and support, without whom I would have never completed this work. In particular, I would like to thank my mother, mother, and father-in-law for supporting my family in Indonesia. I also thank all my Marine Transportation Engineering Department ITS colleagues, especially Pratiwi, Hasan, Dwi, Takim, Eka, and Dika, for their support and encouragement.

TABLE OF CONTENTS

CHAPTER 1. INTRODUCTION

1.1 Background

The pile-supported wharf (PSW) is a vital port facility accommodating shipload transfer and ship berthing. A typical PSW consists of a pile foundation, concrete deck, and auxiliary structures like a trestle bridge. Numerous PSWs are constructed in seismically active regions vulnerable to destruction and function loss. For instance, the Loma Prieta earthquake in 1989 caused critical damage to the Port of Oakland, including lateral spreading and pile head failure [1]. During the 2010 Haiti earthquake, the Port of Port-au-Prince was severely damaged when the PSW was significantly displaced to the sea, submerging the container crane [2]. Other earthquakes, such as the Kobe earthquake in 1995 [3], the Kocaeli earthquake in 1999 [4], and the Samos earthquake in 2020 [5], also resulted in the destruction of port facilities and the disruption of the logistic process. PSW's inability to function might directly influence the functioning of the whole port infrastructure, resulting in substantial economic losses. Therefore, its performance must be appropriately evaluated to mitigate the risk of an earthquake to a PSW.

Indonesia is one of the earthquake-prone countries that rely on its marine transportation, including ports, and Sumatra Island is one of its seismically active regions. Two geological features characterize the seismic activity in Sumatra: the Sunda megathrust, an inter-plate subduction zone between the Indo-Australian and Eurasian plates, and the Sumatra fault, which separates Sumatra into two zones [6]. Earthquakes have caused damage to Indonesia's port facilities, including the 2004 Sumatra–Andaman Islands earthquake [7], the 2007 South Sumatra earthquake [8], the 2009 West Sumatra earthquake [9], and the 2010 Mentawai earthquake [10]. The installation of port facilities on soft coastal soils makes them more susceptible to earthquakes. Thus, developing a fast and reliable method to assess the PSW seismic performance in this region is essential.

A PSW consists of a frame and earth-retaining structure. As ground displacement occurs in the earth-retaining structure during an earthquake, the seismic response analysis of PSWs must consider this impact. When earthquakes occur, the PSWs are exposed to the PSW deck's inertial force and the ground displacement's kinematic force. The kinematic force is typically more devastating since the lateral resistance of the pile is decreased during large earthquakes [11]. When piles are constructed in a soil slope, kinematic force generates a substantial bending moment [12]. Comparing PSWs with and without soil slopes, PSWs with slopes have shorter natural periods. In addition, since the spectral acceleration (SA) amplitude is typically large in the short period range, ignoring the mild soil slope in seismic analysis can lead to potentially unsafe results, even when the kinematic force is minor.

Figures 1.1 – 1.2 show the typical damage at the pile-supported wharf. Typically, the maximum bending moment occurred at the top of the pile connected to the deck. When the bending moment exceeds the pile bending moment capacity, severe damage to the pile could occur. Figure 1.1 displays the pile damaged in a PSW on Andaman Island during the 2004

Sumatra–Andaman Islands earthquake [13]. The concrete pile below the deck was destroyed, leaving only the reinforcement rebar attached to the deck. Figure 1.2 shows similar pile damage in a PSW in Indonesia during the 2004 Sumatra–Andaman Islands earthquake [14].

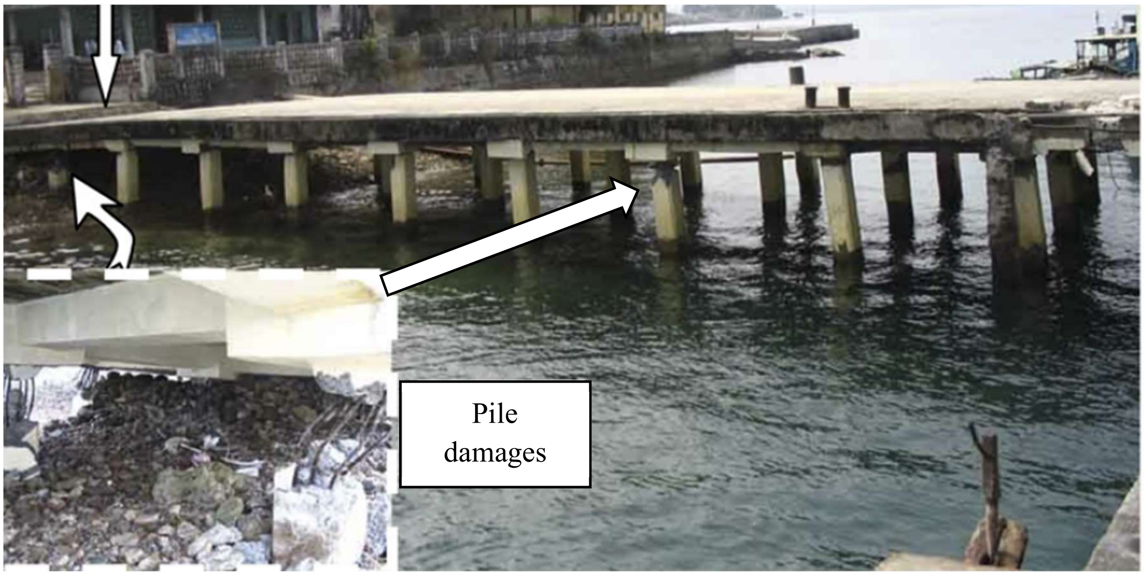

Figure 1.1 The pile damaged in a PSW in Andaman Island

Figure 1.2 The pile damaged in a PSW in Indonesia

Numerous studies have examined PSW's seismic performance in the past. The results of a finite element analysis (FEA) of the soil-structure system for PSWs that have 31 m width or less revealed that ground displacement had a significant impact on the seismic performance of the piles [15–18]. Su et al. [15] performed a full 3D FEA considering soil-structure interaction on a 31 m-wide PSW with a soil slope ratio of 1:1.5 (vertical to horizontal). They found that soil slope deformation substantially affects the seismic response of PSW. Torkamani et al. [16] examined the seismic performance of a PSW by applying a 2D finite-difference model using eight waveform data. The PSW had a width of 28 meters and a slope ratio of 1:2. Results indicated that the porosity of loose sand was the primary factor in the residual displacement variance of the PSW. At the same time, the internal friction angle of loose sand was the dominant factor in the differential settlement of the PSW. Hamrouni et al. [17] examined the PSW performance during the 1989 Loma Prieta earthquake using 2D FEA. The results revealed that substantial lateral ground displacement occurred in the top area of the embankment as a result of the liquefaction of loose sand, which influenced the displacement of the piles. Nagao and Lu [18] performed a series of 2D FEAs on a PSW and demonstrated that the residual displacement of a PSW is primarily due to subsoil deformation.

It is possible to analyze the PSW's seismic performance accurately using FEAs. However, FEA is rarely utilized in design practice as it is time-consuming and demands sophisticated simulation software. In contrast, frame analysis (FA) is a more straightforward procedure for evaluating the seismic performance of PSWs. Therefore, FA is the widely used method used in design practice. Only the PSW is modeled in FA; thus, soil spring elements are employed to account for soil–structure interaction.

In FA, the inertial force approximated from the SA is employed in the PSW deck as a static load. The SA's values depend on the damping coefficient generally taken as 0.03–0.05 in design practice, with an average PSW width of 20–60 m [19,20]. Regarding PSWs exceeding 100 m in width, the typically used damping coefficient may not be applicable. Therefore, it is required to develop an approach for calculating the damping coefficient of wide PSWs.

In the absence of studies on the impacts of the damping coefficient and the kinematic force on the seismic performance of a PSW on a mild slope, this research intended to obtain a procedure for predicting these variables to be used in FA. This research evaluates the seismic performance of a widely used PSW in Indonesia. In this research, the PSW consists of a trestle and a pier with a combined width of 165 meters. The slope ratio beneath the trestle bridge is 1:5 (i.e., mild slope), and according to seismic design practice, the effect of ground displacement is insignificant. Consequently, analysis modeling of only the PSW component and neglecting the mild soil lope has frequently been performed [21–23], although the result of this procedure has not been validated.

In general, only inertial force has been considered in PSW seismic design utilizing FA; the impact of kinematic force on a mild soil slope is often neglected. In addition, the variation in damping coefficient due to the difference in PSW width is frequently ignored in design practice, which may result in overdesign. It is believed that the damping coefficient used to compute SA varies with the width of the PSW. Therefore, a method for determining the optimal damping coefficient for estimating SA based on the width of the PSW by analyzing PSW cross-sections of varying widths and conducting FEA was proposed. In addition, a method for determining the kinematic force to be used in FA without relying on the findings of FEA was proposed.

1.2 Objectives and scope of research

This research aims to develop a new approach to conducting seismic performance assessment of PSW in Indonesia. A new seismic performance assessment for wharves using FA that considers inertial force, kinematic force, and PSW damping coefficient is proposed to achieve this objective. This research also proposed earthquake ground motions (EGMs) for the seismic design of PSW in Indonesia using a statistical approach and compared these EGMs with those in the present design code.

The findings of this study contribute to risk mitigation efforts for port systems, which require knowledge of wharf seismic performance. These findings can provide engineers and decision-makers with reliable tools to help determine whether a wharf's seismic performance in its current configuration is acceptable and what potential changes may be required. The research tasks that were accomplished as part of this research are as follows:

1. A site-specific seismic response analysis for port sites in Sumatra, Indonesia used to determine the EGMs for seismic performance analysis.
2. 2D FEA (i.e., with or without slope consideration) to study the impact of ground deformation on the performance of the wide PSW. Additionally, two short- and long-duration waveforms were employed as motion inputs to investigate waveform duration's effects on the PSW's response.
3. Propose an approach to calculate the optimal damping coefficient for estimating SA based on the width of the PSW by conducting FEA to analyze cross sections of the PSW with varying widths.
4. Propose an approach for calculating the kinematic force used in FA by utilizing the FEA findings.
5. Propose an approach for calculating the kinematic force used in FA by utilizing the 1D analysis findings.

1.3 Outline of dissertation

This thesis is composed of seven chapters, including this chapter, with the following content:

Chapter 2 provides a literature review of various research on seismic performance assessment methodologies. The chapter will discuss each method's analysis concept, advantages, and disadvantages.

Chapter 3 presents a site-specific seismic response analysis for port sites in Sumatra to determine the input waveforms used in the following study.

Chapter 4 contains details of a seismic performance assessment of a wide PSW considering soil slope and waveform duration.

Chapter 5 contains details of the seismic performance assessment of PSW using the 2D frame analysis method, considering both inertial and kinematic forces.

Chapter 6 contains the application of seismic performance assessment of PSW using 2D frame analysis with 1D analysis to determine kinematic force.

Chapter 7 contains the summary and significant conclusions of this work. It also reflects the transferability of the method, describes the present study's limitations and provides recommendations for future work.

1.4 Publications

The work presented in this dissertation has yielded several journal publications. The following journal publications have already been published and are included for reference:

Boyke, C.; Refani, A.N.; Nagao, T. Site-Specific Earthquake Ground Motions for Seismic Design of Port Facilities in Indonesia. Appl.Sci. 2022, 12, 1963. https://doi.org/ 10.3390/app12041963

This publication draws primarily on content presented in Chapter 3

Boyke, C.; Nagao, T. Seismic Performance Assessment of Wide Pile-Supported Wharf Considering Soil Slope and Waveform Duration. Appl. Sci. 2022, 12, 7266. https://doi.org/10.3390/ app12147266

This publication draws primarily on content presented in Chapter 4

Boyke, C.; Nagao, T. Seismic Performance Assessment of Pile-Supported Wharfs: 2D Frame Analysis Method Considering Both Inertial and Kinematic Forces. Appl. Sci. 2023, 13, 3629. https:// doi.org/10.3390/app13063629

This publication draws primarily on content presented in Chapter 5

CHAPTER 2. LITERATURE REVIEW

2.1 Introduction

This chapter explores the available seismic performance assessment methods in the literature, focusing on empirical and analytical techniques. This chapter first reviews the methods commonly used for performance assessment and then shows the advantages and disadvantages of each presented method.

2.2 Physical simulation methods

2.2.1 Shaking table and centrifuge test

Shaking table and centrifuge tests were well-known physical simulation methods for assessing the seismic performance of a PSW, particularly the piles having the kinematic force from the ground slope during an earthquake. Dobry et al. [24] conducted six centrifuge model tests on single-pile foundations to investigate the effect of kinematic force on pile bending moment and the largest bending moments (Mmax) often occurred at the borders between liquefied and non-liquefied soil layers. In the majority of cases, the bending moment values at such boundaries peaked and subsequently dropped during shaking. The pile's lateral soil pressure per unit area was constant at 10.3 kPa.

Li et al. [12] designed and implemented a centrifugal shake table test on a PSW on a sand layer soil slope to study the liquefied soil pressure imposed on a single pile. The bending moment at the pile bottom appears larger than at the top, indicating that the bottom has a notable consolidation effect. In addition, they discovered that the Japan Road Association (JRA) formulas for calculating kinematic load overestimated the soil pressure in PSW piles when compared with test results. Tang et al. [25] conducted a shake table test to examine the behavior of a reinforced concrete pile on a sheet-pile wall induced by liquefaction-induced lateral displacement. Haigh and Madabhushi [26] also conduct centrifuge tests to study the soil-pile interaction, measuring a 16 kPa homogeneous soil pressure on piles in a liquefiable stratum.

Current lateral soil pressure models have been suggested based on test findings; however, major discrepancies have been identified between the soil pressures reported by the previous research. Consequently, choosing the proper kinematic force used for PSW design is complicated. In addition, the proposed soil pressure models were generated mainly from the results of single-pile testing. Based on FEA finding for PSW pile groups on a soil slope, the soil lateral kinematic forces decrease with distance from the slope's crest [27]. Therefore, soil pressure methods based on single-pile tests are inapplicable to pile group PSW; a different approach must be developed to predict the kinematic forces working on PSW piles on a soil slope.

2.2.2 On-site test

Boroschect et al. [20] conducted an on-site experimental evaluation to find the dynamic properties of a PSW. This study summarizes the outcomes of several experiments to determine the damping coefficients of a 20 m wide PSW section subjected to seismic excitation. The experiment was created with two main goals in mind: (1) to find the fundamental damping of the PSW using micro vibration waves formed by tides, wind, and microtremors; and (2) to estimate the dynamic properties as a function of response amplitude by applying lateral deformation of varying amplitudes to the PSW using a pull instrument. Even though the PSW was planned as a sequence of independent deck segments, the research discovered that the non-structural element significantly impacts the dynamic behavior, especially in the longitudinal axis of the PSW. Therefore, sliding connections must be provided for non-structural parts, or their effect must be included in the PSW design. Based on an analysis of the PSW at various excitation levels, it was found that the behavior of the PSW is relatively linear, with a damping coefficient of about 3%. The damping value is an average damping coefficient value for analyzing PSW structures subject to working loads and low-magnitude earthquakes. However, it is possible that the widely used damping coefficient may not be appropriate for PSWs longer than 100 meters. Therefore, a new approach must be developed for calculating the damping coefficient of wide PSWs.

2.3 Numerical simulation methods

2.3.1 Non-linear Static Analysis (NLSA) - Pushover Analysis (POA)

The NLSA procedure, commonly known as POA, is a method in which a structure model is subjected to a lateral load such as a seismic force. Displacement of the structure is calculated by applying monotonically increased lateral forces until the model's displacement exceeds or reaches the allowable displacement. This method is widely used in design practice and is presented in ATC 40 [28] and FEMA 356 [29].

ATC 40 [28] presents the POA method as the capacity spectrum method (CSM). This method evaluates a force-displacement relationship in the acceleration-displacement response spectrum (ADRS) format. It is known as the capacity curve. The design response spectra are then converted to ADRS format to obtain a demand curve. This process allows the capacity curve to be compared to the demand curve at a certain structure's performance point, which corresponds to the target displacement. The obtained target displacement is compared with story drifts corresponding to the displacement limit (Table 2.1) to determine the structure's performance level.

Table 2.1 Displacement limits according to ATC 40 [28]

Inter story Drift Limit	**Performance Level**			
	Immediate Occupancy	**Damage Control**	**Life Safety**	**Structural Stability**
Maximum Total Drift Ratio	1%	1%–2%	2%	0.33 V/P
Maximum Inelastic Drift Ratio	0.5%	0.5%–1.5%	No limit	No limit

Note: V is total lateral shear force, and P is total gravity load

The displacement coefficient method (DCM) is presented in FEMA 356 [29]. The DCM method differs from the CSM method in estimating the target displacement, which does not require the capacity and demand curve in ADRS format. Instead, the target displacement ($\boldsymbol{ut}$) can be calculated using the following equation:

$$\boldsymbol{ut = C_0 . C_1 . C_2 . C_3 . SA . \frac{T_e^2}{4\pi^2}} \qquad \text{(Eq.2.1)}$$

where C_0 = adjustment factor to relate spectral displacement of an equivalent SDOF (Single Degree of Freedom) system to the building roof displacement MDOF (Multi Degree of Freedom). Roof displacement is selected because the target displacement is aimed to represent the maximum displacement during the design earthquake, which most likely occurs on the roof.

C_1 = adjustment factor to relate expected maximum inelastic displacements to maximum displacements calculated for the linear elastic response.

C_2 = adjustment factor to consider the effect of stiffness and strength deterioration at beam and column on maximum displacement response.

C_3 = adjustment factor to represent increased displacements due to dynamic P-Δ effects.

SA = spectral acceleration.

Te = effective fundamental period.

ASCE 61-14 [30] is a code that presents a POA method for wharf structures. In this code, the displacement capacity is obtained by POA when the first strain limit in pile materials is reached. The allowable material strains for operating level earthquake (OLE), contingency level earthquake (CLE), and design earthquake (DE) are listed in Table 2.2. At the same time, displacement demand can be calculated by simplified methods such as the substitute structure method [31] or by response spectra analysis and NLTHA.

Table 2.2. Strain limits of steel pipe pile according to ASCE 61-14 [30]

Pile / Hinge Location	Component	Performance Level of Pile Hinges		
		Minimal Damage (MD)	**Controlled and Repairable Damage (CRD)**	**Life Safety Protection (LS)**
Steel Pipe Pile / Top of Pile	Concrete	$\varepsilon c \leq 0.010$	$\varepsilon c \leq 0.025$	-
	Reinforcing Steel	$\varepsilon s \leq 0.015$	$\varepsilon s \leq 0.6\varepsilon_{smd} \leq 0.06$	$\varepsilon s \leq 0.8\varepsilon_{smd} \leq 0.08$
Steel Pipe Pile / In-Ground	Steel pipe	$\varepsilon s \leq 0.010$	$\varepsilon s \leq 0.025$	$\varepsilon s \leq 0.035$
Steel Pipe Pile / Deep in Ground (>10 x Pile Diameter)	Steel pipe	$\varepsilon s \leq 0.010$	$\varepsilon s \leq 0.035$	$\varepsilon s \leq 0.050$

Note: εc = concrete compressive strain; εs = strain in steel pipe pile (tension or compression); ε_{smd} = strain at peak stress of dowel reinforcement.

Zacchei et al. [32] presented an example of the POA application to the CSM method. They performed a POA of a pile-supported wharf in a new oil tanker's port using a 3-D finite element method against a ground motion of peak ground acceleration of 0.55 g. Shafieezadeh et al. [33] conducted a vulnerability assessment of pile-supported wharves using the POA. They used non-linear pile-deck elements with fiber sections to capture non-linear displacements in a pile–deck connection. The wharf deck was defined by rigid beam elements, and the subsurface condition beneath the wharf was represented by P–Y spring elements. The parameters of P–Y spring elements were determined using the soil properties of each layer.

The POA method has gained popularity in earthquake engineering due to its simplicity and ability to capture the non-linear behavior of structural elements. The POA can explain the elastic-plastic behavior of wharves. The precision of the results depends on the appropriateness of the mechanical characteristics of structural elements. One of the shortcomings of this method is its inability to consider the effect of the soil deformation related to the response of the wharf. Furthermore, while the POA can account for the non-linear force-displacement characteristics of various wharf components, such as piles and pile-deck connections, it cannot account for the dynamic interaction between soil and structure.

2.3.2 Finite Element Analysis (FEA) - Non-linear Time History Analysis (NLTHA)

The FEA is a widely used method of representing physical cases using the numerical technique. NLTHA can be utilized in FEA for nonlinear-dynamic structural response under seismic acceleration time history loading. Using soil-structure FEA, the seismic performance evaluation of PSWs may be appropriately studied. Using this approach, Boyke and Nagao [27], Nagao and Lu [18], and Lei Su et al. [15] have investigated the seismic responses of PSWs. In FEA, the structure and soil layer are modeled, and complicated problems, such as the soil-structure interaction in the case of lateral deformation due to earthquakes, are resolved. However, FEA is rarely employed in design practice due to its complexity and time-consuming nature.

2.3.3 Finite Element Analysis (FEA) – Incremental Dynamic Analysis (IDA)

One of the advanced methods in conducting NLTHA is incremental dynamic analysis (IDA), the advanced method to calculate global collapse capacity based on extending a single NLTHA into an incremental one. IDA is a series of non-linear dynamic analyses of a specific structure subjected to ground motions of varying intensities. IDA aims to provide information about the structure's behavior, from elastic to inelastic to collapse. The IDA result can be shown in structural response parameters versus intensity measure curves [34]. The steps for determining the global collapse capacity specified using the IDA technique are listed in FEMA-351 [35].

Several researchers have begun using IDA as the primary method in their research. For example, Sobban et al. [36] studied the dynamic buckling of a cylindrical steel tank subjected to horizontal and vertical ground motions. Utilizing both POA and IDA, they determined the tank's buckling capacity. The buckling capacity curves and critical buckling loads calculated using POA were compared to the IDA outcomes. Soltani and Amirabadi [37] researched the effect of the unknown orientation of earthquakes, called the directional uncertainty, on pile-supported wharves. The POA and incremental dynamic analysis (IDA) were used in their research to develop a fragility curve in each earthquake orientation. Nazri and Saruddin [38] created fragility curves for steel and concrete frames using near-field and far-field ground motion records. As input, they used seven ground motion records for near-field and seven records for far-field. Five performance levels set by FEMA-356 [29] were used as structural performance benchmarks in generating the IDA curve.

The primary advantage of IDA is that it can reflect the actual dynamic behavior of structures and take into account varied intensities of recorded ground motion. However, this procedure is time-consuming because producing each IDA curve requires several NLTHA. Therefore, it is not cost-effective because the IDA procedure is time-consuming [39].

2.3.4 Frame Analysis (FA)

FA is the typical design approach because it is a more uncomplicated technique for investigating the seismic response of the frame structure (i.e., PSW). FA has limitations, including the inability to account for ground deformation due to earthquakes and the modeling of solely the PSW; hence, soil spring components are utilized to account for soil–structure interaction. The magnitude of SA depends on the damping coefficient, and the value frequently used in PSW engineering design is 0.03–0.05, with a typical PSW width between 20 and 60 meters [19,20]. The widely assumed damping coefficient may not be acceptable for PSWs with a width greater than 100 meters. Therefore, a technique for calculating the damping coefficient of wide PSWs must be developed.

CHAPTER 3. SITE-SPECIFIC SEISMIC EARTHQUAKE GROUND MOTION FOR THE DESIGN OF PORTS IN INDONESIA

3.1 Introduction

Evaluation of earthquake ground motions (EGMs) is required for port structure design in Indonesia and other high-seismicity nations to prevent seismic disasters. The Indonesian port facility seismic design code is SNI 1726:2019, "Seismic Design Criteria for Buildings and Other Structures" (SNI) [40]. The SNI was constructed based on ASCE 7–16 [41] and the Indonesian Seismic Hazard Maps 2017 (ISHM) [42]. The ISHM was created using an improved probabilistic seismic hazard analysis (PSHA). In the PSHA, the EGMs relating to a specific exceedance probability were evaluated using seismic data from 1900 to 2016 surrounding the target region. Only a single EGM probability exceedance in the SNI is mentioned (i.e., 2 percent in 50 years, with 2475 years as a return period) [40]. The exceedance probability relates to the EGM for evaluating the structural performance level of life safety protection as specified in ASCE 7–16. At a rock site, the ISHM displays peak ground accelerations (PGAs) and spectral accelerations (SAs) at periods of 0.2 s and 1 s, respectively, as descriptive values of the EGMs. Notably, the waveforms employed by the PSHA have not been disclosed.

The degree of EGM amplification at a site with a sedimentary layer varies according to the condition of the ground. The SNI classifies the ground characteristic into six site classes (Table 3.1). Site class SF relates to the exceptionally soft ground where a building is forbidden; hence, seismic design is unnecessary. The research of Stewart and Seyhan [43] identifies the amplification factor for each site type. Stewart and Seyhan [43] modeled the ground using the average shear wave velocity value in the top 30 meters (Vs30) and investigated seismic response. The average from the analysis output for each ground condition was then utilized to estimate the seismic design amplification factor.

The EGMs must be established for seismic design using a site-specific approach [44]. Kim et al. [45], Nguyen et al. [46], and Nagao [47] are examples of research on site-specific EGMs for Korea, Vietnam, and Japan, respectively. No site-specific EGMs have been researched to update the EGMs in the SNI. The SNI EGMs may be sufficient regarding the PGAs for ground with thin sedimentary layers because they were developed using PSHA, considering Indonesian seismicity, and the EGM amplification has a minimal impact. However, its validity at sites with sedimentary layers has not been confirmed. First, the ground models of Stewart and Seyhan [43] were oversimplified, and ground data from the United States, Japan, and other regions outside of Indonesia were used. The amplification properties of EGMs are heavily reliant on the ground profile. During a massive earthquake, soft ground displays a non-linear response. The degree of non-linear response varies heavily on the topography. Second, the EGMs are controlled by source, path, and site amplification types. Analyzing the observed ground motions in Indonesia is necessary to examine the EGMs for design in Indonesia.

Table 3. 1. Site class in the SNI 1726:2019

Site class	$Vs30$ (m/s)	$\bar{N}$	$\overline{Su}$ (kPa)
SA	>1500	-	
SB	750–1500	-	
SC	350–750	>50	≥100
SD	175–350	15–50	50–100
SE	<175	<15	<50
	Any location with more than 3 meters of soil that possesses the following properties: - $PI > 20$; $w \geq 40\%$ - $\overline{Su} < 25$ kPa		
SF	- For soils with a high potential to collapse during an earthquake - Peats and highly organic clays > 3 m - Very high-plasticity clays > 7.5 m ; $PI > 75$ - Very thick, soft/medium-stiff clays > 35 m ; $\overline{Su} < 50$ kPa)		

Note: SA is a hard rock, SB is a rock, SC is very dense soil and soft rock, SD is stiff medium soil, SE is soft clay soil, SF is particular soil requiring site response analysis and special geotechnical site investigation, PI is plasticity index, w is moisture content $\overline{Su}$ is undrained shear strength.

This chapter proposes site-specific EGMs for the design of the Indonesian port structure. The soil comprises shallow and deep subsurfaces, and the EGM amplification is notably more significant in deep subsurfaces than in shallow ones. Therefore, a site-specific EGM evaluation should appropriately consider the effect of the deep subsurface [44,47,48]. In addition, EGMs can be estimated based on physics-based models [49–52] if the data on the 3D soil structure is available. However, there are no data on this; therefore, this study will only focus on shallow subsurface amplification and examine site amplification factors using borehole data.

In coastal locations, port structures are built on soft ground; hence SD and SE site classifications are targeted. The EGM recordings in Indonesia are gathered, and the impacts of the shallow subsurface at the observation locations are minimized by calculating the incident EGMs at the bedrock using seismic response analysis.

The amplitude of the EGM at the bedrock is modified so that the PGA value matches that of the SNI bedrock. Next, data from the port's boreholes are gathered to generate soil models. The EGMs in the port area were computed using a seismic response analysis of 144 analysis that accounted for the non-linear properties of the shallow subsurface. Through statistical processing of the attained EGMs, this research proposes EGMs for the seismic design of Indonesia's port structure and compares these new EGMs to those in the SNI.

3.2 Methods

3.2.1 Incident EGM at the bedrock

Although Indonesia has experienced several significant earthquakes in the past, few EGM data are accessible, and EGM data for port zones are lacking. In addition, the recorded EGMs were influenced by the soil layer at the seismograph equipment site; consequently, they cannot be used for the seismic design of the port structure by merely modifying the amplitude of the recorded EGMs. Through seismic response analysis, the effect of the shallow subsurface must be eliminated, and the incident EGM at the bedrock must be analyzed. This research collected nine EGM data (Figure 3.1, Table 3.2) and soil data from the selected sites. All were big earthquakes with a moment magnitude (Mw) of at least 6.0. However, due to the long hypo-central distances, the PGAs were small.

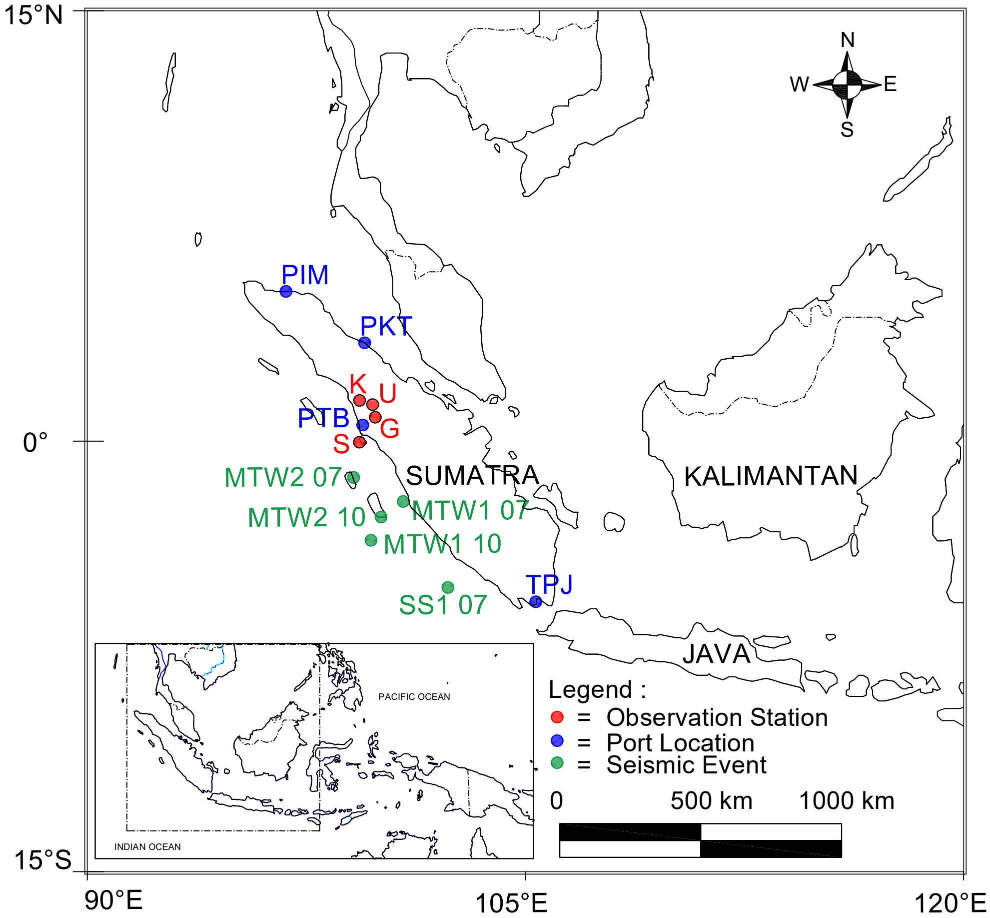

Figure 3.1 Map.

Table 3.2 EGM data.

No.	Seismic Events	Site class	Observation station	PGA (g)	Ground motion code
1	Mentawai 1, 2010 (Mw 7.8 —focal depth: 20.1 km)	SC SD SD	Gadut; Kuranji; Unand	0.037 0.026 0.037	MTW1 10 G MTW1 10 K MTW1 10 U
2	Mentawai 2, 2010 (Mw 6.3 —focal depth: 26 km)	SC SD SD	Gadut; Kuranji; Unand	0.039 0.025 0.043	MTW2 10 G MTW2 10 K MTW2 10 U
3	Southern Sumatra, 2007 (Mw 8.4 —focal depth: 34 km)	SD	Sikuai Island	0.037	SS1 07 S
4	Mentawai 1, 2007 (Mw 7.9 —focal depth: 30 km)	SD	Sikuai Island	0.110	MTW1 07 S
5	Mentawai 2, 2007 (Mw 7.0 —focal depth: 22 km)	SD	Sikuai Island	0.014	MTW2 07 S

The EGM records observed included two horizontal component records. This study separated the two horizontal components to maximize the small amount of EGM recordings. Thus, there were 18 EGM records. Before the seismic response analysis could be done, baseline correction was conducted, and EGM data had to be tapered. Figure 3.2 depicts the Fourier spectra of the EGMs'east–west direction component. The Fourier spectra of MTW 1 07 S exhibit significant amplitudes in the frequency range higher than 1 Hz since it has a higher peak ground acceleration of 0.12 g than the other EGMs of 0.015–0.04 g. Predominant frequencies range from 0.5 Hz to 4 Hz, indicating that EGMs with various frequency characteristics have been represented.

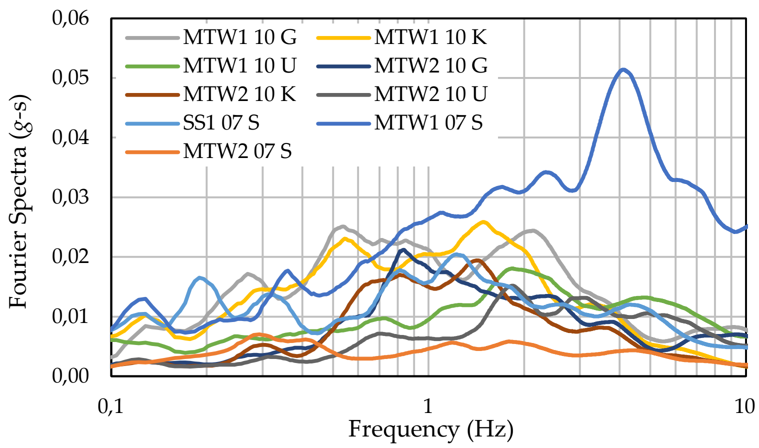

Figure 3.2 Fourier spectra.

A frequency domain seismic response analysis accounting for non-linear soil characteristics was conducted to calculate the incident EGMs at the bedrock using ground surface EGM (deconvolution). Figure 3.3 depicts the nonlinear soil properties used in this research. The dashed line represents the characteristics of sandy soil. The solid line represents cohesive soil. The blue line represents the normalized shear modulus (G/Gmax), whereas the red line represents the damping coefficient. For the shear modulus and damping coefficient dependences on the shear strain, Seed and Idriis [53] for sandy soil and Vucetic and Dobry [54] for cohesive soil were used. The DEEPSOIL programs [55] were utilized for the simulation.

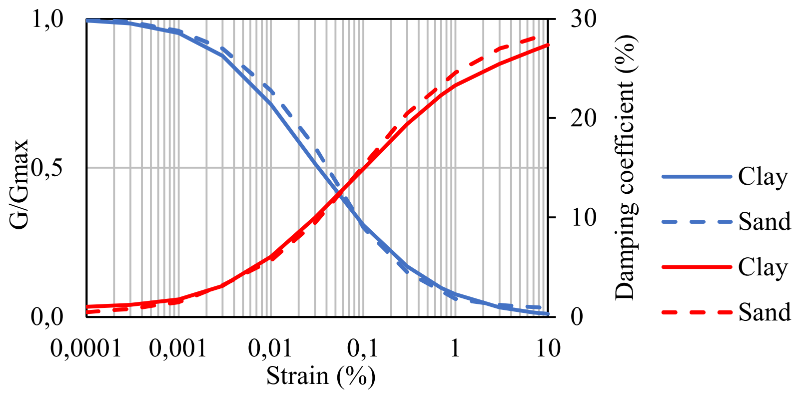

Figure 3.3 Nonlinear characteristics of the soil

The obtained soil data only included the unit weight and the N-values from the standard penetration test; therefore, the S-wave velocity of every single soil layer was estimated with the correlation formula recommended by Imai and Tonouchi [56]. The soil properties of the Sikuai Island observation station are illustrated in Table 3.3. The sixth layer's hard clay silt was considered the bedrock at this location. Figure 3.4 shows the Fourier spectrum and time history of the EGM at the surface and bedrock concerning the east–west component of MTW1 07 S. The predominant amplitude of 4 Hz in the EGM at the surface was a result of the shallow subsurface; however, the predominant frequency in the incident EGM at the bedrock was unknown.

Table 3.3 Shallow subsurface data.

Layer	Soil type	Thickness (m)	Unit weight (kN/m³)	*Vs* (m/s)
1	Silt sediment	4	17	80
2	Silt clay	18	16	141
3	Clayey silt	8	16	161
4	Sandi Silt	8	20	186
5	Clayey Silt	8	23	195
6	Hard Clay Silt	6	25	361

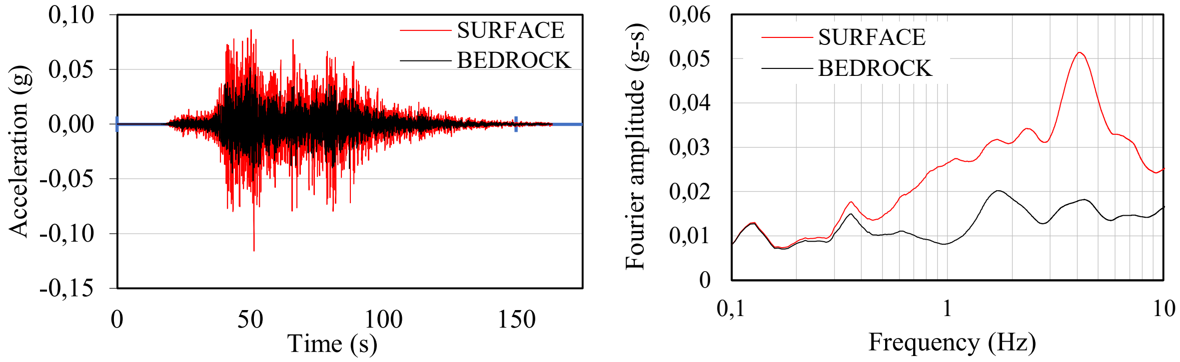

Figure 3.4. Time history waveforms and Fourier spectra.

Then, the PGA of the incident EGM on the bedrock was matched to the SNI at site class SC (i.e., very dense soil); the matched PGA was 0.40 g. Figure 3.5 displays the SA for the east–west component of MTW1 07 S, which was matched to the SA of the SNI for site class SC. In this instance, the SA at the bedrock for periods less than 0.3 s was greater than that of the SNI, whereas the SA was smaller than the SNI for periods greater than 0.3 s. The individual SA has a different amplitude than the SA of the SNI. Figure 3.4 depicts a comparatively large Fourier amplitude in the high-frequency region of the bedrock EGM, which is caused for the substantial SA of MTW1 07 S in the extremely short period range.

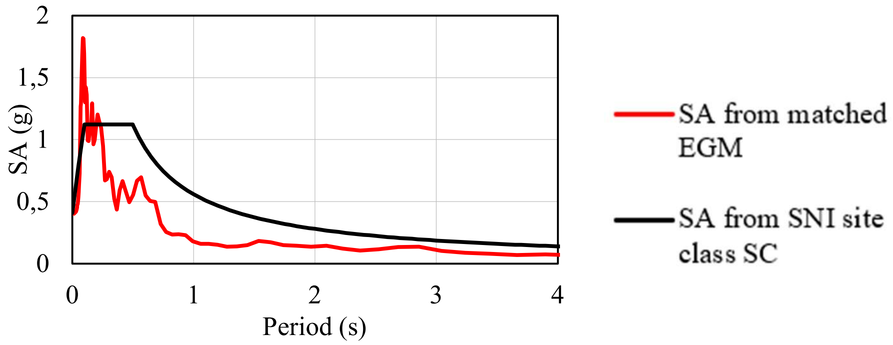

Figure 3.5. Comparison of SAs.

3.2.2 EGMs in port sites

This research focused on port locations in Sumatra: Port of Teluk Bayur (PTB), Tarahan Powerplant Jetty (TPJ), Pupuk Iskandar Muda Jetty (PIM), and Port of Kuala Tanjung (PKT) (Figure 3.1). The collection of two boring data per site resulted in eight data. Figure 3.6 exemplifies four soil profiles. The S-wave velocities were calculated using the N-values as in the preceding section. The bedrock depths ranged between 10 and 50 meters. The SD site class consisted of only the PIM. The classification for the remaining three sites was SE site. This indicates that most site classes for Indonesian port locations are SE.

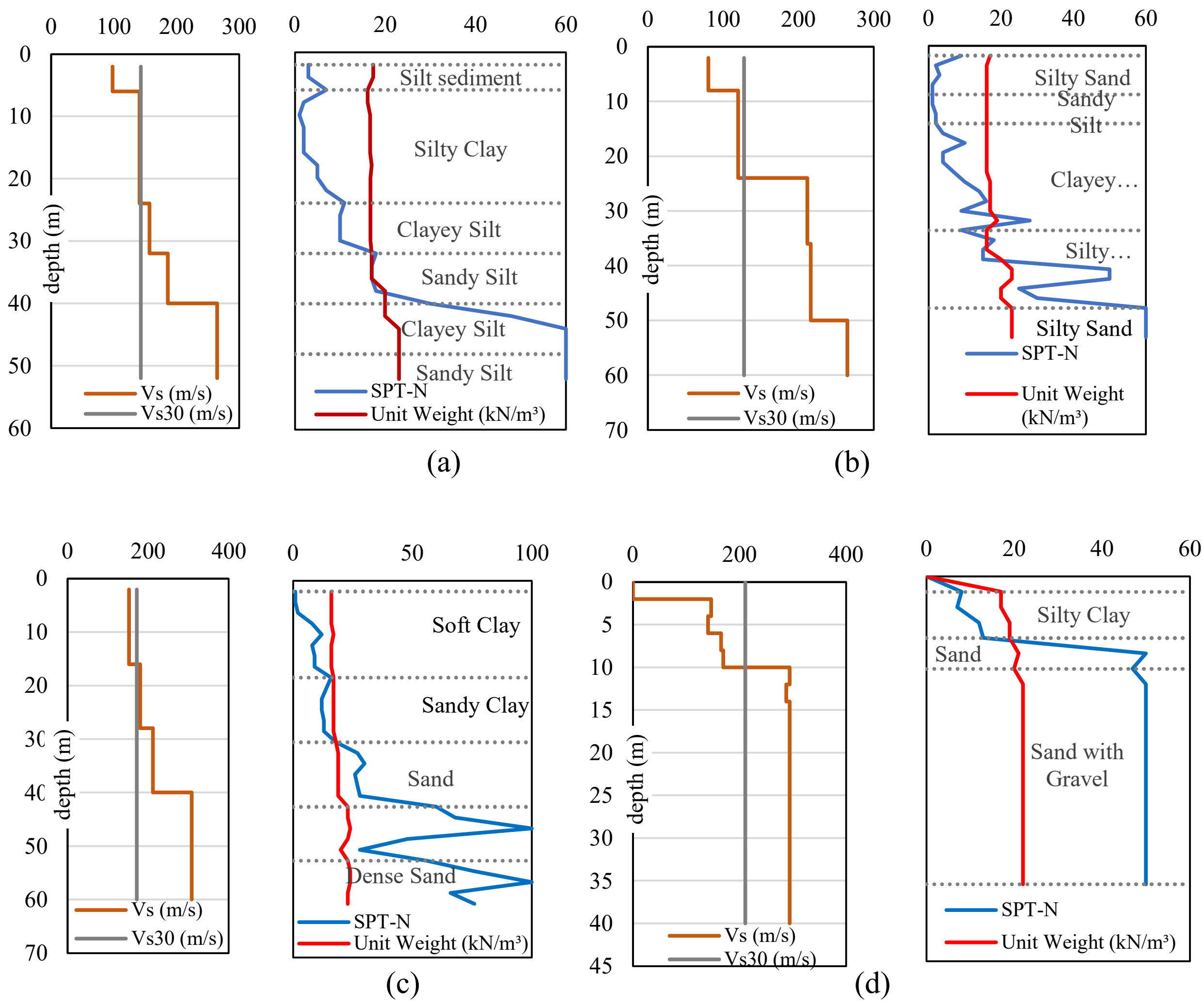

Figure 3.6. Soil data at observed port location: (a) PTB; (b) TPJ; (c) PKT; and (d) PIM.

Figure 3.7 illustrates the target location transfer functions. The transfer function at SD (i.e., PIM) revealed a dominant frequency of 1.92 Hz with a factor of 4.03 amplification. The predominant frequencies at SE stretched between 0.96 Hz and 1.26 Hz, representing shorter values than those at SD. The maximum values at the predominant frequencies varied between 3.36 and 3.94. The transfer functions were calculated using the original soil shear modulus (i.e., before the earthquake). Using the 18 incident EGMs at the bedrock and the eight shallow subsurface data, the 144 EGMs on the ground surfaces were analyzed using a seismic response analysis that accounted for the nonlinear soil properties. There were 38 and 106 EGMs for site classes SD and SE, respectively.

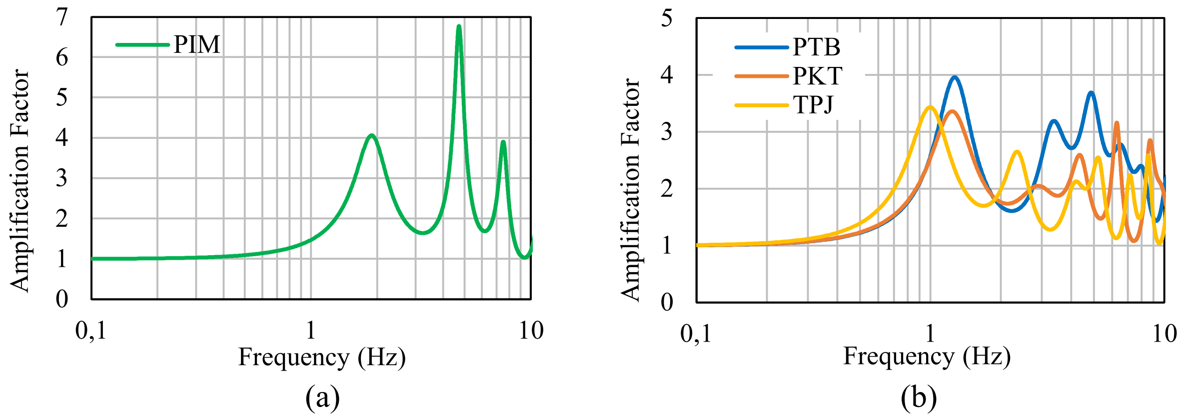

Figure 3.7. Transfer function: site classes (a) SD and (b) SE.

3.3 Results and discussion

3.3.1 EGM results

Figure 3.8 illustrates the obtained SAs for every site class. The blue line represents each SA. The black line indicates the median SAs. The red line depicts the mean + standard deviation (SD) of SAs. The SA distribution for SD and SE site classes was substantial. Specifically, the spreading was high in the period band of less than 1.0 s for SD and 1.5 s for SE. The natural period of a wharf is typically less than 1.5 s; thus, this finding indicates that the SA distribution in the natural period zone of the wharf is high.

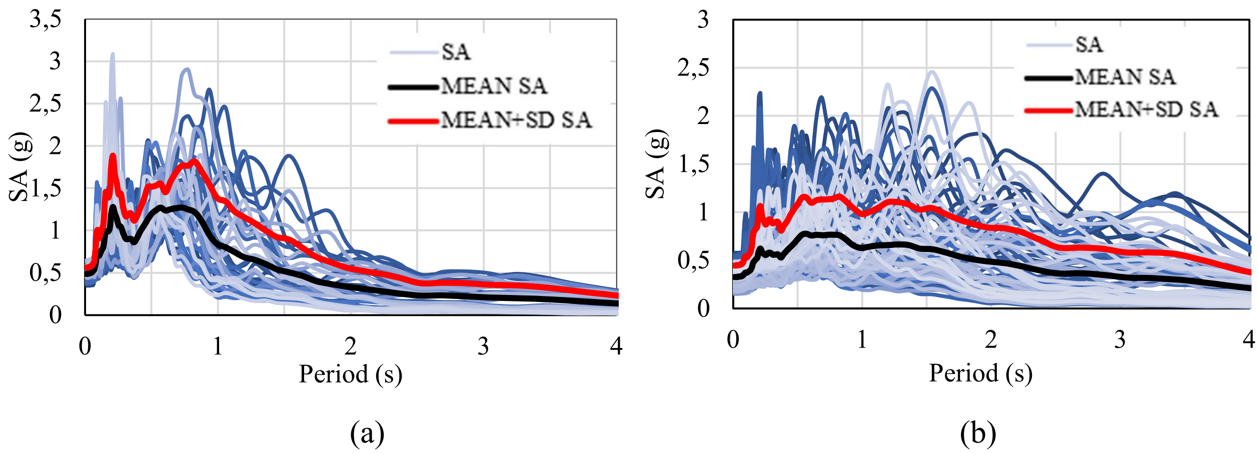

Figure 3.8. SAs in (a) SD and (b) SE.

The following was the cause of this substantial SA spreading. Figure 3.9 shows the large and small SA findings and the mean + SD SA. A large SA exhibited high values in the SD class's 0.7–1.0 s period band. Compared to the mean + SD SAs, the SAs in the remaining period bands were relatively small. A similar observation was made about the SE class. In the 1.0–1.5 s period band, the SAs were significant, but not in another period. However, in low SAs, the SAs displayed small values relative to the mean + SD SAs for the whole period range. This indicates that the characteristics of the shallow subsurface amplification had a substantial influence on the SA amplitudes.

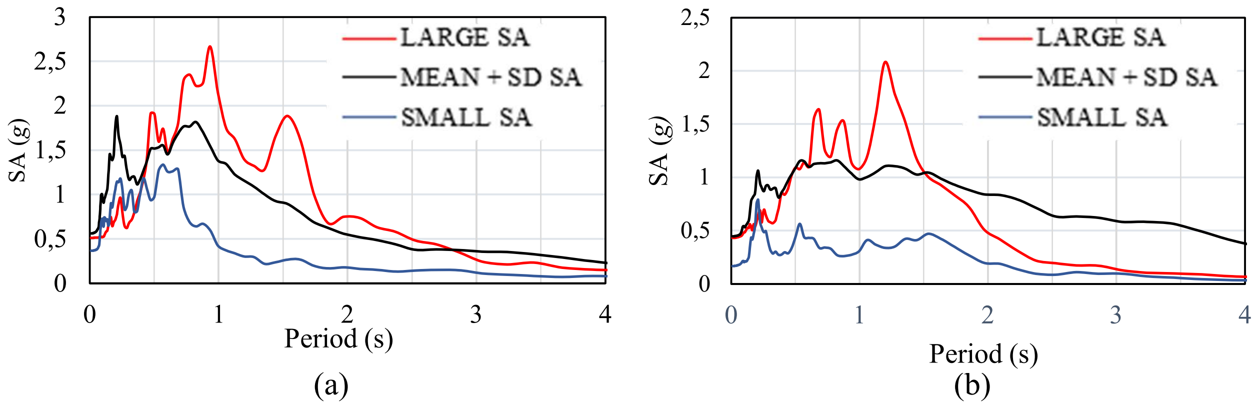

Figure 3.9. Comparison of the SAs (a) SD and (b) SE

Figure 3.10 depicts the Fourier spectrum of incident EGMs, the transfer function of the shallow subsurface, and the Fourier spectrum of EGMs at the surface. In instances when the SAs obtained high values, the predominant frequencies of the incident EGMs at the bedrock corresponded with those of the transfer functions, producing significant SAs at a certain period. When the SAs became very small, not only were the Fourier spectra of the incident EGMs small, but the two predominant frequencies did not coincide, resulting in small SAs.

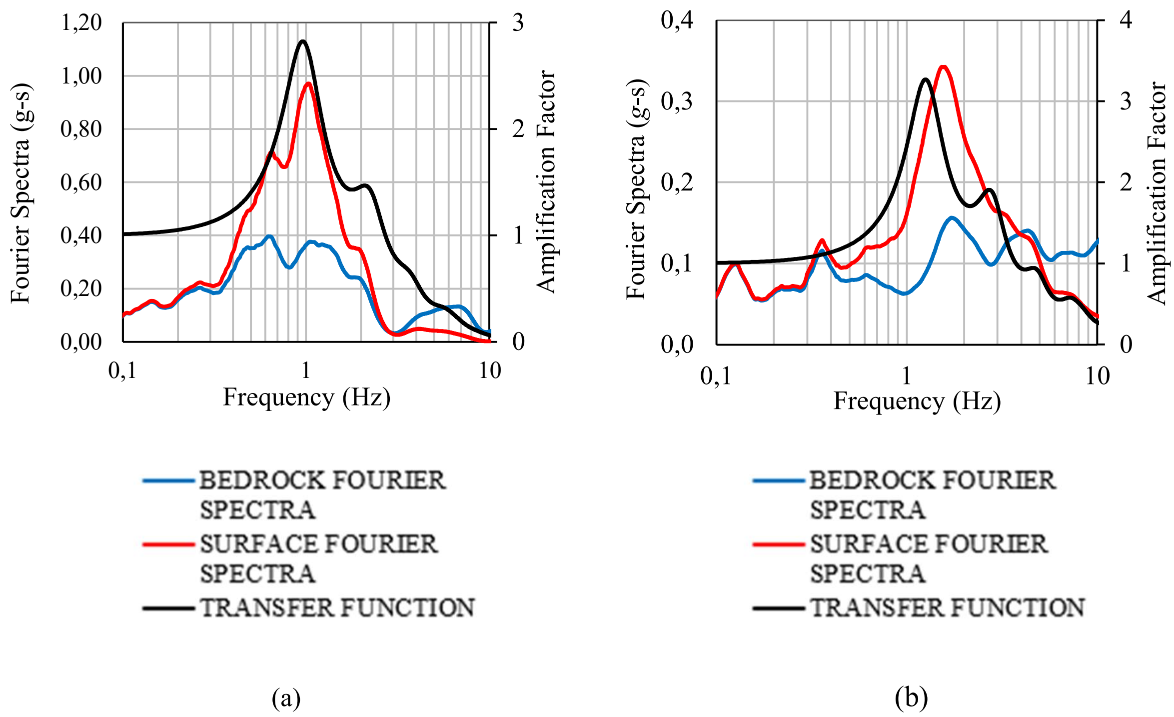

Figure 3.10. *Cont.*

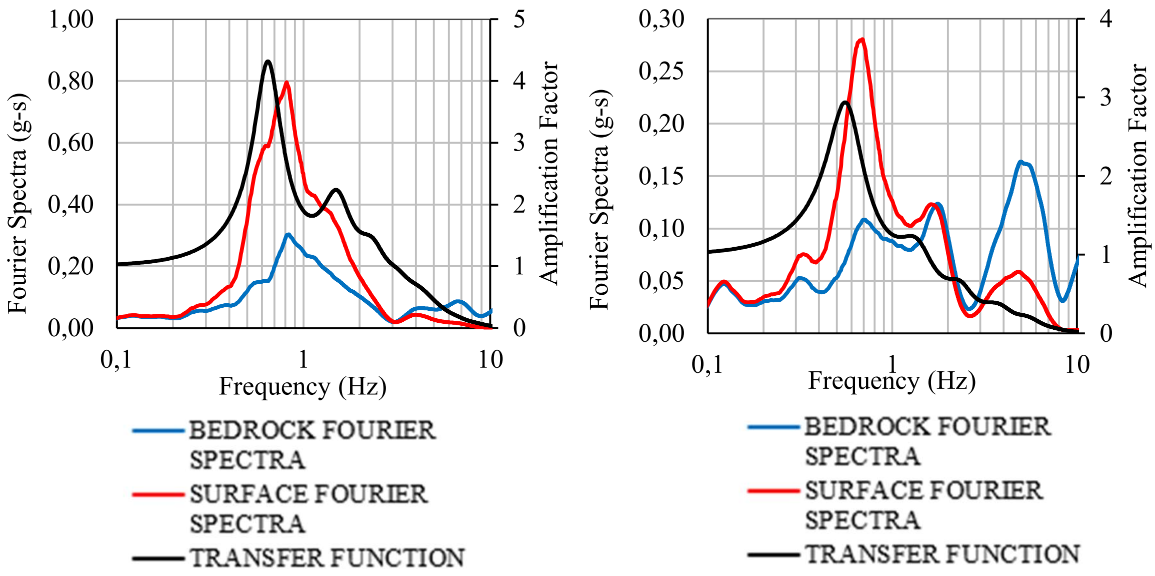

(c) (d)

Figure 3.10. Comparison of the spectra in (a) site class SD; large SA, (b) site class SD; small SA, (c) site class SE; large SA, (d) site class SE; small SA.

The SA variance was quite large; consequently, site-specific EGMs for seismic design must be determined based on individual ground conditions utilizing methodologies presented in this research. In many circumstances, however, the soil properties at selected sites were not collected in detail. In such a scenario, the degree of coincidence between the natural period of the port structure and the shallow subsurface must be evaluated. During major earthquakes, attention must be paid to the decrease in the shear stiffness of soft soils, as this will increase the natural period of the shallow subsurface. Figure 3.11 compares the transfer functions before and during an earthquake at the points explained in Figure 3.9. (a). During an earthquake, the natural frequency falls from 1.28 Hz to 0.92 Hz. When the natural period of the port structure and the shallow subsurface coincide, the SA becomes very large.

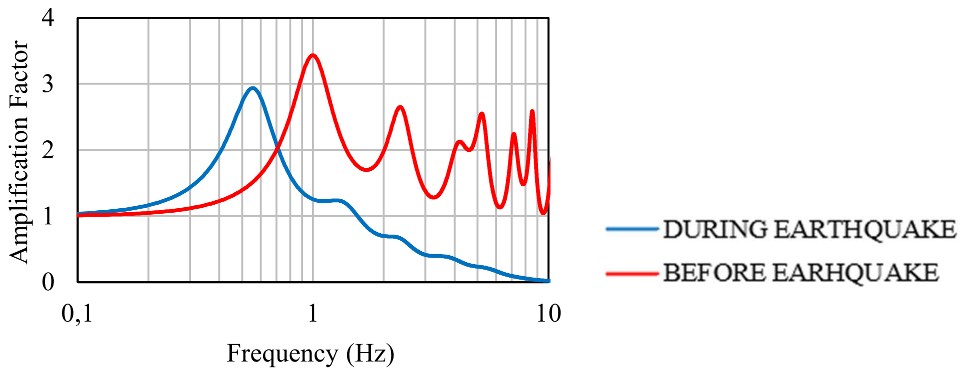

Figure 3.11. Comparison of the transfer functions.

The normalized modulus reduction and damping coefficient curves are two fundamental dynamic soil parameters needed to conduct an equivalent-linear seismic site response study and determine soil amplification (Figure 3.3). It is widely known that soft ground amplifies EGM and produces more severe damage than hard ground. The soft layer amplified the low-frequency EGM more than the hard layer [57]. Additionally, the thickness of the soft layers substantially enlarged the PGA. Figure 3.3 demonstrates that the sand layer's normalized modulus reduction curve and damping coefficient are slightly more significant than the clay layer's. Consequently, the EGM was amplified more in the clay layer than in the sand layer due to the greater values of the damping coefficient and modulus reduction in the sand layer.

3.3.2 SAs for seismic design of port structures

The seismic design SAs must be set on the conservative side because the SA dispersion was so large. Nagao [47] stated that the SAs for the seismic design of Japanese highway bridges correspond to the mean + SD level of the SAs, except for the short period range. As stated previously, the seismic design SAs in the SNI are the average EGMs with a return period of 2475 years, which is incredibly long compared to the design working life of infrastructures. In light of this, as an engineering judgment, this study proposes the SAs for the seismic design of the port structure in Indonesia by aiming for the average SAs envelope. For seismic design, the typical shape of the SAs is as follows: the SA increases linearly in a very short period range, followed by a flat curve, and decreases inversely proportional to the period in a long period range. For developing the SA for site Class SD (Figure 3.12 a), first, the two points where the SA reached their maximum values were selected. These two chosen points were the peaks of the average SA curve that occurred at 0.2 and 0.8 s periods. The decreasing curve was set as inversely proportional to the period. They do not become faithful traces of the envelope values but have similar concepts applied in design codes. For SD, the formula is $SA=0.7/(T–0.25)$ at a period longer than 0.8 s. A similar step was used in developing SA for site class SE. The first point (i.e., at 0.3 s) of the maximum SA value was obtained as the intersection of the flat curve (i.e., the flat line that touches the maximum value of the average SA curve) and the linearly increase curve (i.e., the curve that connects the SA at 0 s period and maximum SA under 0.3 s period). In comparison, the second point (i.e., at 1.2 s) was obtained as the intersection of the flat curve and the decreasing curve (i.e., set as $1.1/(T + 0.2)$). Figure 3.12 depicts the proposed SAs along with the average SAs, mean + SD SAs, and SNI SAs for each site class. Also shown in Table 3.4 are the proposed SAs.

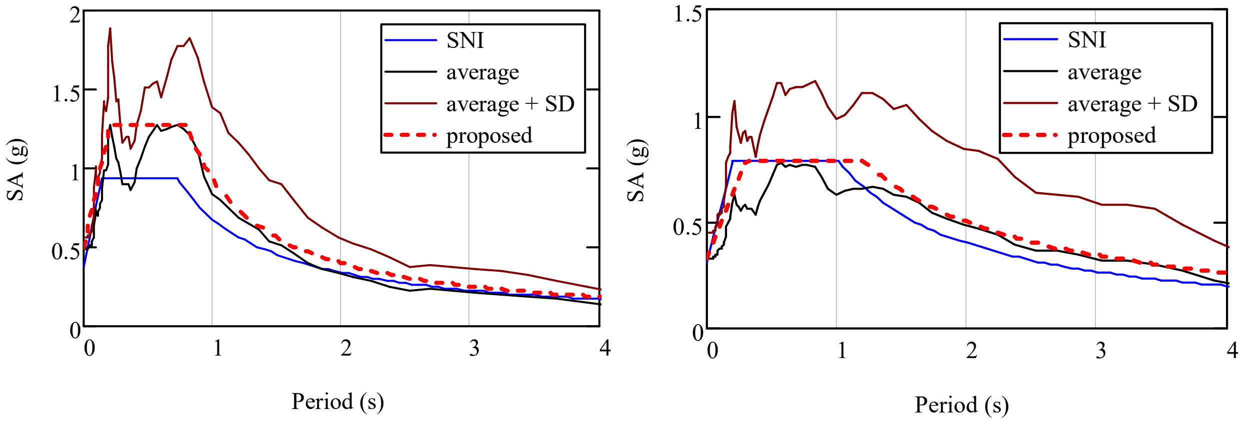

(a) (b)

Figure 3.12. Proposed SAs in site classes (a) SD and (b) SE.

Table 3.4 Proposed SAs.

Site class	Period; T (s)	SA (*g*)
SD	0	0.50
	0.2	1.28
	0.8	1.28
	>0.8	0.7/(T – 0.25)
SE	0	0.33
	0.3	0.79
	1.2	0.79
	>1.2	1.1/(T + 0.2)

3.3.3 Comparison of the proposed SA and SNI

Regarding site class SD, the proposed SA was larger than the SNI in the period range of 0.2–2.0 s, which is the natural period range for the vast majority of port structures. In the period range of 0.2–0.8 s, the proposed SA had a maximum value of 1.28 g, whereas the SNI SA had a maximum value of 0.93 g. The proposed SA had a maximum value that was 1.38 times greater than the SNI. Figure 3.5 demonstrates that for periods of 0.3 s or longer, the SA at the bedrock was smaller than that of the SNI. This discrepancy in SAs suggests that the SNI underestimated the amplification factor of the EGMs for site class SD.

In the period range of 1.0 s or less, there was no apparent difference between the two SAs for site class SE. Nonetheless, the proposed SA was more significant than the SNI for 1,0 s or more extended periods. At 1.5 s, the proposed SA (equal to 0.65 g) was 1.20 times greater than the SNI (equal to 0.54 g). During massive earthquakes, the natural frequency of the shallow subsurface decreases due to the nonlinear soil properties. The variation in the natural period is large for the soft soil condition (i.e., for site class SE). This research appropriately accounted for the nonlinear soil characteristics in the analysis, which explains why there is a discrepancy in the long-period SAs. Using the proposed SAs, an acceptable seismic design of the port structure was developed for both site classes.

CHAPTER 4. SEISMIC PERFORMANCE EVALUATION OF WIDE PILE-SUPPORTED WHARF WITH THE INFLUENCE OF SOIL SLOPE AND WAVEFORM DURATION

4.1. Introduction

A PSW comprises an upper structure (i.e., beam and slab) and foundation elements. Because soil displacement happens in the foundation component during seismic activity, it is essential to account for this effect when analyzing the seismic response of PSWs. Numerous studies have previously examined the seismic performance of PSWs. Su et al. [15] conducted a complete 3D soil-structure finite element analysis on a 31 m-wide PSW with a soil slope ratio of 1:1.5 (vertical to horizontal). They demonstrated the substantial effect of ground slope deformation on the PSW seismic response. Torkamani et al. [16] investigated the seismic performance of a PSW by applying a 2D finite-difference model to eight seismic waveforms. The PSW had a width of 28 meters and a slope ratio of 1:2. The outcomes indicated that the porosity of loose sand contributed the most to the residual displacement variation of the PSW. In contrast, the internal friction angle of loose sand contributed the most to the differential settlement. Using 2D FEA, Hamrouni et al. [17] investigated the performance of a PSW in the 1989 Loma Prieta earthquake. The findings specified that the liquefaction of loose sand caused significant lateral soil displacement in the upper portion of the embankment, affecting the piles' deformation. Nagao and Lu [18] performed 2D FEAs on a PSW and demonstrated that the residual displacement of a PSW is primarily due to subsoil deformation.

Ground motion properties such as amplitude, frequency characteristics, and waveform duration have been identified as fundamental components affecting structure response [58–60]. Amplitude and frequency characteristics are typically considered by spectral acceleration (SA), which is widely accepted by the engineering community as the principal basis for structure design and evaluation. In contrast, waveform duration has taken less focus, specifically in PSW's seismic response evaluation. Numerous research, including Barbosa et al. [61], Ou et al. [62], Romney et al. [63], Mantawy and Anderson [64], and Chandramohan [65], have utilized nonlinear dynamic analyses to evaluate the effect of the waveform duration on structures, particularly buildings, and bridges. Although waveform duration has a negligible impact on peak demands like peak story drifts and peak member forces, it significantly impacts cumulative damage metrics, like residual displacement and accumulated plastic strain, as found by the general conclusion of these studies.

Pushover analysis [66–68] is a standard method for assessing the seismic performance of a PSW. This analysis calculates the seismic performance of PSWs located on the horizontally stratified ground with a high degree of accuracy; however, it cannot consider the impact of soil deformation produced by seismic activity. Using pushover analysis, the performance point and fragility curves of a PSW can be assessed.

In light of the lack of study on the effect of soil displacement and waveform duration on the seismic performance of a PSW with a mild soil slope, this chapter aims to conduct the seismic performance of a widely used PSW in Indonesia. The PSW under consideration consists of a trestle bridge and a wharf with a total width of 165 meters. The slope under the trestle bridge is mild, with a slope ratio of 1:5, and the impact of soil displacement is considered negligible in seismic design practice.

This chapter aims to give a more comprehensive method for evaluating the seismic performance of wide PSWs. The 2D soil-structure system FEA with/without consideration of a soil slope to examine the effect of ground deformation on the seismic performance of a wide PSW is developed in this chapter. Moreover, two short- and long-duration waveforms were utilized as motion inputs to investigate the effects of the duration on the seismic response of the PSW.

4.2. Methods

4.2.1 Target PSW

The case study in this chapter was a PSW with a frame structure constructed in Indonesia using a steel pipe pile foundation and reinforced concrete deck. Due to the mild slope of the seabed, the PSW was constructed far from the coastline to achieve the depth requirements for container ships; thus, a trestle is required to connect the PSW to the land.

Figure 4.1 depicts the PSW target and ground configurations. The dimensions of the PSW are 80 m x 300 m, connected to a trestle measuring 85 m x 13 m and a causeway measuring 60 m in width. The crown height of the PSW is +4.00 m low water spring (LWS), and the deck is supported by 15 rows of vertical steel pipe piles with diameters (Ø) of 1100 and 1200 mm that sit on a seabed that is 13 m below LWS. The trestle consists of a reinforced concrete deck and 17 rows of Ø 1000 mm steel pipe piles that rest on a mild soil slope with a ratio of 1:5. The trestle and PSW were linked and integrated against earthquakes.

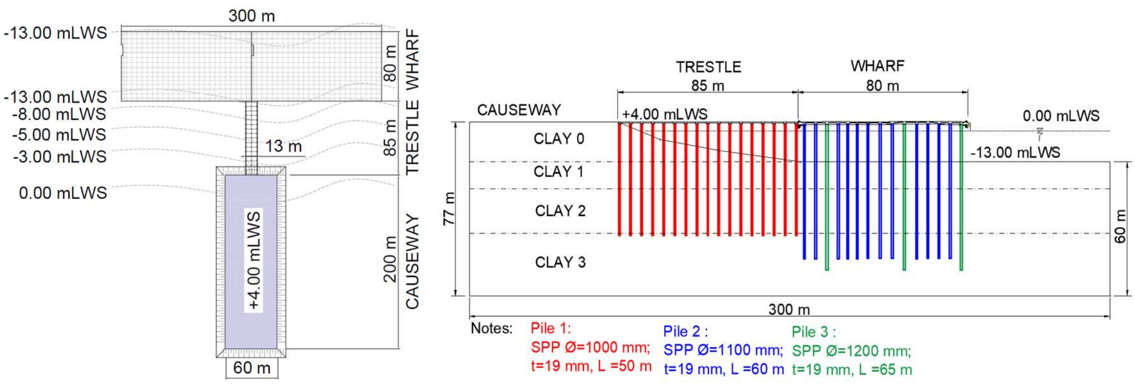

(a) plan view (b) side view

Figure 4.1. PSW configuration.

The soil properties resulting from a soil investigation are displayed in Table 4.1. The soil layer contains four silty clay layers, with Clay 0 being soft clay at the landside surface and Clay 3 being stiff ground at the pile's base. The shear wave velocity (Vs) of each soil layer was calculated using the correlation equation proposed by Imai and Tonouchi [56] with the N-value observed from the standard penetration test (N-SPT). The ground's natural frequency was determined to be 0.94 Hz. This site falls into site class E (soft ground) according to the Indonesian seismic code SNI 1719 2019 (SNI) [40].

Table 4.1 Soil properties.

Layer code	N-SPT	Layer thickness (m)	Soil type	Specific gravity *(GS)*	Water content (*Wn(*%))	Unit weight (γn(kN/m³))	Void ratio (*e*)	Liquid limit (*LL(*%))	Plastic limit (*PL(*%))	Shear wave velocity (*Vs*(m/s))
Clay 0	5–8	17	Soft Clay	2.60	29.67	13.34	1.44	49.5	21.8	162.1
Clay 1	10	12	Medium Stiff Silty Clay	2.61	33.67	14.12	1.43	52.6	24	197.7
Clay 2	11–16	20	Medium Stiff Silty Clay	2.62	41.84	14.32	1.41	52.7	23	210
Clay 3	30–60	28	Very Stiff Silty Clay	2.63	38.08	14.51	1.4	52.5	22	332

4.2.2 Finite element modeling

A 2D FEA model was developed using PLAXIS 2D [69]. Fifteen nodal-point triangular elements were used to construct PSW models, which were then analyzed as plane strain models. The FEA used two consecutive loading phases corresponding to the actual condition: static (i.e., only account for PSW and soil self-weight) and seismic wave loading phases. During the static phase, the boundary conditions for the side boundaries were set to be normally fixed, whereas the boundary conditions for the bottom boundary were fully fixed. Regarding the seismic wave phase, the side and bottom boundaries were defined using free-field and compliant base boundaries [70]. The fine mesh was chosen as the mesh coarseness to transfer waveforms in a high-frequency range.

The hardening soil small-strain (HSS) model accounted for the soil nonlinearity. The HSS model is a variation of the hardening soil model that considers the increased stiffness of soils at small strains [70], which is depicted by two material parameters of G_0^{ref} (the small-strain shear modulus) and $\gamma^{0.7}$ (the shear strain level at which the small-strain shear modulus has declined to around 70% of its initial value) [71]. In this chapter, the drainage condition is modeled as undrained, which yields superior numerical simulation performance in the seismic load compared to other drainage conditions. The plate elements were used to represent the deck. The piles were depicted using an embedded beam row option. This feature enables the 2D modeling of piles with a specified out-of-plane spacing and has been verified using 3D FEA models and measurements from actual tests [72–74].

The 2D FEA was divided into two scenarios to enable a more precise comparison of the seismic performance of PSW between the two modeling approaches. In Scenario 1, the PSW was modeled without regard to the seabed's slope and displacement (Figure 4.2a). Scenario 2 considers the seabed slope and displacement (Figure 4.2b). Two distinct waveforms of differing durations were applied to each scenario as input motion. Therefore, four case analyses were conducted for this study.

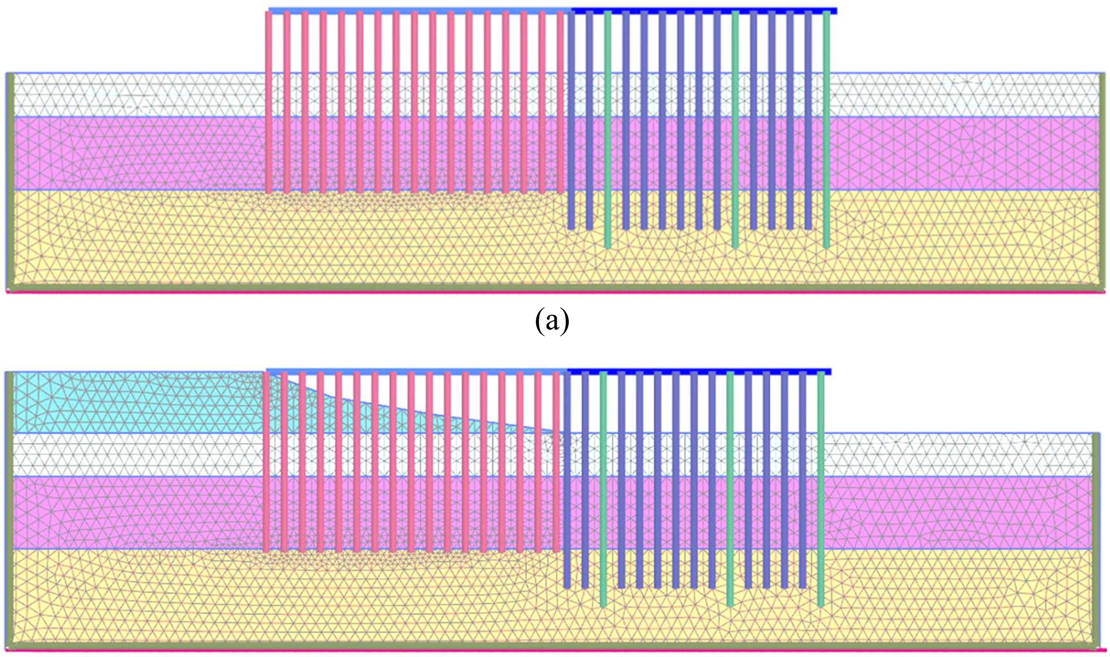

(a)

(b)

Figure 4.2. Finite element model. (a) Scenario 1; (b) Scenario 2.

Table 4.2 outlines the soil parameters utilized by the HSS model. The compression (Cc) and swelling (Cs) indices were computed based on Bowles [75] (Equations (4.1) and (4.2)). The initial void ratio (e_{init}) was calculated as a function of Wn [76] (Equation (4.3)). The $\gamma^{0.7}$ was estimated using Equation (4.4) based on its correlation with PL [77]. The G_0^{ref} was estimated in correlation with the N-SPT value using Imai and Tonouchi [56] (Equation (4.5)).

$$C_c = 0.007\,(LL - 7) \qquad \text{(Eq.4.1)}$$

$$C_s = 1/5\ \mathrm{C_c} \qquad \text{(Eq.4.2)}$$

$$e_{init} = 0.0197\,Wn + 0.2143 \qquad \text{(Eq.4.3)}$$

$$\gamma^{0.7} = 1.10^{-4} + 5.10^{-4}\,PL \qquad \text{(Eq.4.4)}$$

$$G_0^{ref} = 14.12\,N^{0.68}\ \text{(MPa)} \qquad \text{(Eq.4.5)}$$

Table 4.2 Input parameters for the HSS model.

Parameter	Unit	Clay 0	Clay 1	Clay 2	Clay 3
$\gamma\ sat$	kN/m^3	16.24	16.31	16.40	16.47
$\gamma\ unsat$	kN/m^3	13.35	14.11	14.29	14.53
C_c		0.0297	0.0319	0.0320	0.0319
C_s		0.00595	0.00638	0.00640	0.00637
e_{init}		0.77	0.88	1.10	1.00
C'_{ref}	kN/m^2	2.5	5	10	20
ϕ'		23	25	27	35
Ψ		0	0	0	0
$\gamma^{0.7}$		0.00021	0.00022	0.00022	0.00021
$G_0{}^{ref}$	kN/m^2	42,206.6	67,620.9	93,085.6	228,677.6

Note: $\gamma\ sat$ is saturated soil unit weight, $\gamma\ unsat$ is unsaturated soil unit weight, C'_{ref} is effective cohesion, ϕ' is effective internal friction angle, and Ψ is dilatancy angle.

Table 4.3 outlines the pile parameters utilized in the embedded beam row element. The pile was modeled as an elastoplastic circular tube beam and subdivided into three piles: 1 for the trestle pile and 2 and 3 for the wharf piles. The piles had a yield strength of 2.4×10^5 kN/m^2 and Young's modulus of 2.0×10^8 kN/m^2. Lateral resistance (T_{lat}) was estimated using Equation (4.6), using the correlation relating undrained cohesion (Cu) and Ø [78]. Axial (F_{max}) and skin (T_{skin}) resistance were determined based on Décourt [79]. T_{skin} in Equation (4.7) was determined considering the pile base friction coefficient (β) [80] average N-SPT value at embedded pile depth (NS), pile cross-sectional area (A_p), and embedded pile depth (L). F_{max} (Equation (4.8)) was determined considering pile base coefficient (α) [80], average N-SPT value in between 4$Ø$ under and 4$Ø$ above pile tip (NP), characteristic soil coefficient (K) [80], and A_p. T_{lat} and T_{skin} values were set to increase linearly from the pile head to the pile tip in this model.

$$T_{lat} = 9\ Cu\ Ø \qquad \text{(Eq 4.6)}$$

$$T_{skin} = \beta\ (NS/3 + 1)\ A_p\ L \qquad \text{(Eq 4.7)}$$

$$F_{max} = \alpha\ NP\ K\ A_p \qquad \text{(Eq 4.8)}$$

Table 4.3 Input parameters for embedded beam row elements.

Parameter	Unit	Pile 1	Pile 2	Pile 3
$Ø$	m	1	1.1	1.2
t	m	0.019	0.019	0.019
A_p	m^2	0.585	0.651	0.717
I	m^4	0.00705	0.0107	0.0129
M_p	kN·m	4392	5522	6583
N_p	kN	140,544	156,000	170,400
$T_{skin,start}$	kN/m	130	149	162
$T_{skin,end}$	kN/m	440	500	577
F_{max}	kN	4780	5440	6020
$T_{lat,start}$	kN/m	108	118	130
$T_{lat,end}$	kN/m	2340	2673	2916
Z	m^3	1.83×10^{-2}	2.30×10^{-2}	2.74×10^{-2}

Note: t is thickness of pile, I is moment of inertia, M_p is plastic bending moment.

Table 4.4 outlines the material properties of the reinforced concrete decks, which are modeled as plate elements. The deck was modeled as an elastoplastic-isotropic material with a 35 MPa compressive strength., a Poisson's ratio of 0.2, and Young's modulus of 2.7×10^7 kN/m2. The live load per unit width and depth was set at 20 kN/m/m for the PSW and 10 kN/m/m for the trestle. Due to the more significant load a PSW must resist, the PSW deck had a greater dimension and capacity than the trestle.

Table 4.4 Input parameters for plates.

Parameter	Unit	Wharf	Trestle
b	m	1	1
h	m	1	0.7
A	m	1	0.7
I	m^4	0.0833	0.0200
M_p	kN·m	3503.5	1282.38
N_p	kN	16,721	8543

Note: b is width, h is height, and A is profile area.

4.2.3 Input waveforms

This chapter used two waveforms to investigate waveform duration's effect on PSW's seismic response: the short-duration waveform (SDW) and the long-duration waveform (LDW). Figure 4.3 depicts two waveforms observed in Indonesia [81] employed in this analysis. These waveforms were altered to match the target SA on SNI site class SE [81] (Figure 4.4). The following procedures have been implemented based on the observation that the frequency characteristics of a waveform's Fourier spectrum and SA are similar [47]. First, the Fourier spectrum and SA for every waveform were determined. The ratio between the target and calculated SA was then computed at each frequency. Next, the Fourier spectrum was multiplied by the ratio. The Fourier spectrum was then inverse-transformed to get time history data. The spectrum then became inverted. Time history data was attained by using Fourier transformation. SA was then computed and contrasted. It is important to note that the procedure preserved the Fourier phase spectra of the reference waveforms. Figure 4.4 illustrates the difference between the target SA and the obtained SA. The obtained SA corresponds to the value of the target SA, especially for periods of 1 s or longer.

Figure 4.5 depicts the waveforms that result from this method. The obtained waveforms have envelopes that are comparable to the reference waveforms. The waveforms obtained were those at the ground's surface. A frequency domain seismic response analysis accounting for nonlinear soil characteristics was conducted to attain input ground motions for FEA, and the incident waveforms at the bedrock were calculated (deconvolution). The Vucetic and Dobry [54] was referred for the shear modulus and damping coefficient depending on the shear strain. The incident waveforms at the bedrock are illustrated in Figure 4.6. At the bedrock, the maximum acceleration was smaller than at the surface. The SDW's maximum acceleration was 1.43 m/s/s at bedrock and 3.17 m/s/s at the surface. Regarding the LDW, the maximum acceleration was 1.58 m/s/s at bedrock and 3.20 m/s/s at the surface.

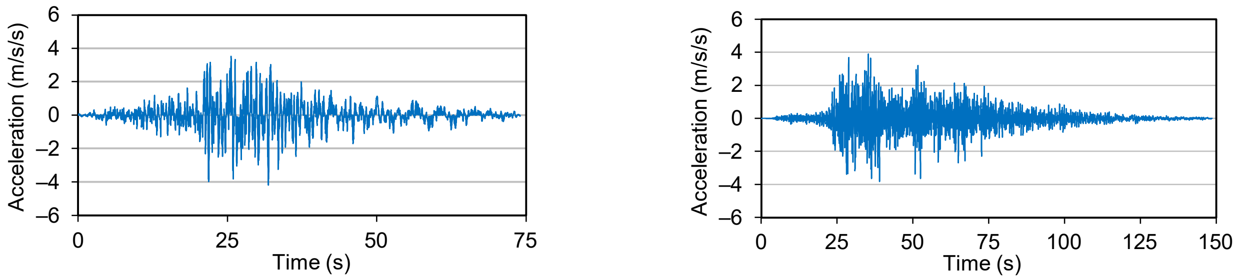

(a) (b)

Figure 4.3. Reference waveforms. (a) SDW; (b) LDW.

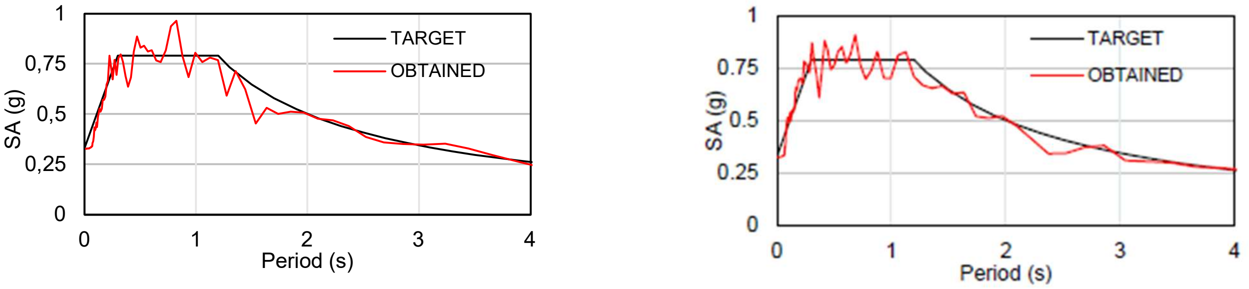

(a) (b)

Figure 4.4. Target and obtained SAs. (a) SDW; (b) LDW.

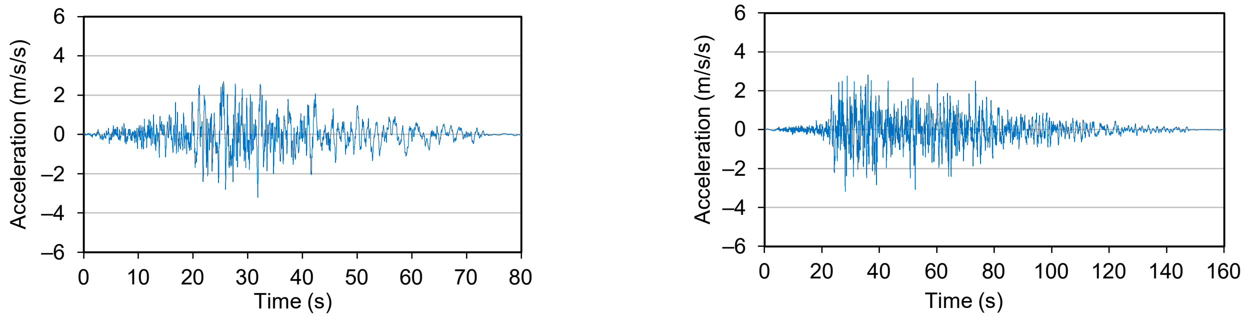

(a) (b)

Figure 4.5. Obtained waveforms. (a) SDW; (b) LDW.

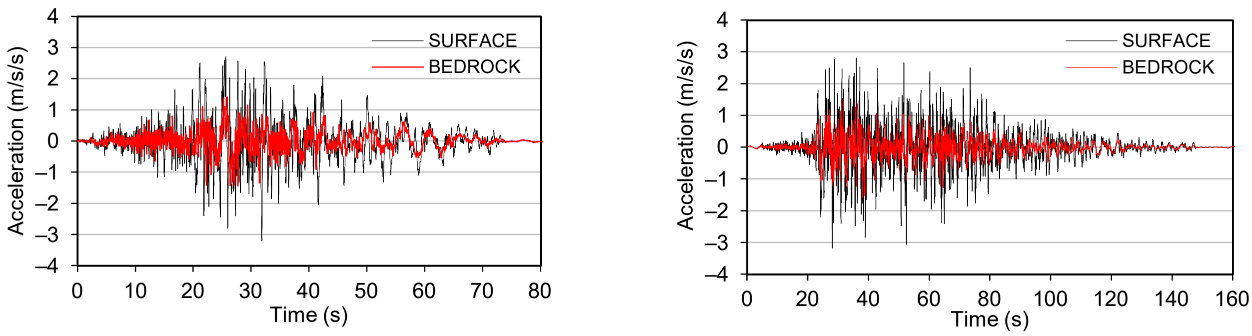

(a) (b)

Figure 4.6. Input waveforms. (a) SDW; (b) LDW.

4.3. Results and discussion

4.3.1. PSW response

Figure 4.7 shows the horizontal acceleration time history at the upper right (seaward) end of the PSW deck in scenario 1. The LDW generated a maximum acceleration of 0.8 g, more than the SDW at 0.55 g. The PSW and ground surface Fourier spectra in scenario 1 are shown in Figure 4.8. A log-triangle smoother [82] was used to smooth the Fourier spectrum. The predominant frequency of the PSW was 0.85 Hz, whereas that of the ground surface was 0.65 Hz. Therefore, the resonance impact was negligible.

Figure 4.7 illustrates the horizontal acceleration time history at the upper right (seaward) end of the PSW deck for Scenario 1. The LDW generated a most significant acceleration of 0.80 g, larger than the SDW's 0.55 g. The PSW and ground surface Fourier spectra for Scenario 1 are illustrated in Figure 4.8. Using a log-triangle smoother [82], the Fourier spectra were refined. The predominant frequency of the PSW was 0.85 Hz, while it was 0.65 Hz for the ground surface. Therefore, the effect of resonance was insignificant.

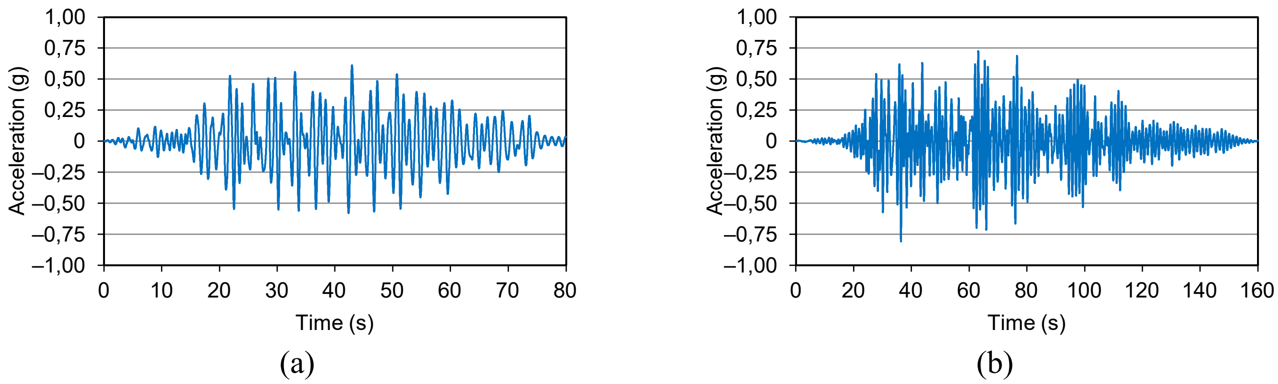

Figure 4.7. PSW time histories in Scenario 1. (a) SDW; (b) LDW.

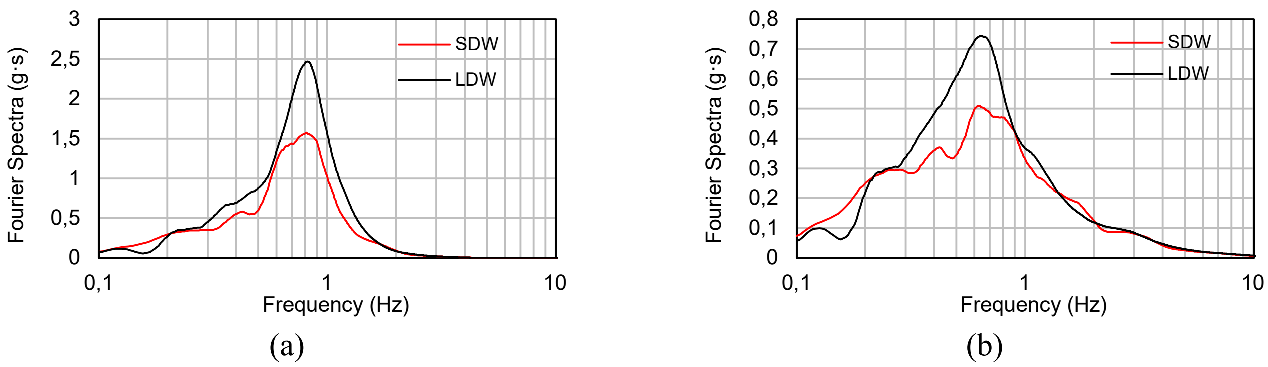

Figure 4.8. Fourier spectra in Scenario 1. (a) PSW; (b) ground surface.

Figure 4.9 depicts the time history of the PSW's acceleration in scenario 2. The maximum acceleration produced by the LDW was 0.65 g, which was greater than the SDW's 0.55 g. Figure 4.10 depicts the PSW and the landside's ground surface Fourier spectra for Scenario 2. Different frequency characteristics were observed between the PSW and the ground. For the PSW, the predominant frequency was 1.15 Hz, while for the ground surface, it was 0.85 Hz. In scenario 2, the PSW had a shorter natural period than in scenario 1. This is because, in scenario 2, the free length of the pile on the slope was shorter than in scenario 1. Figures 4.8a and 4.10a demonstrate that the maximum Fourier spectra of the PSW with the LDW were larger than those with the SDW. The difference is because the SDW and LDW have distinct phase characteristics.

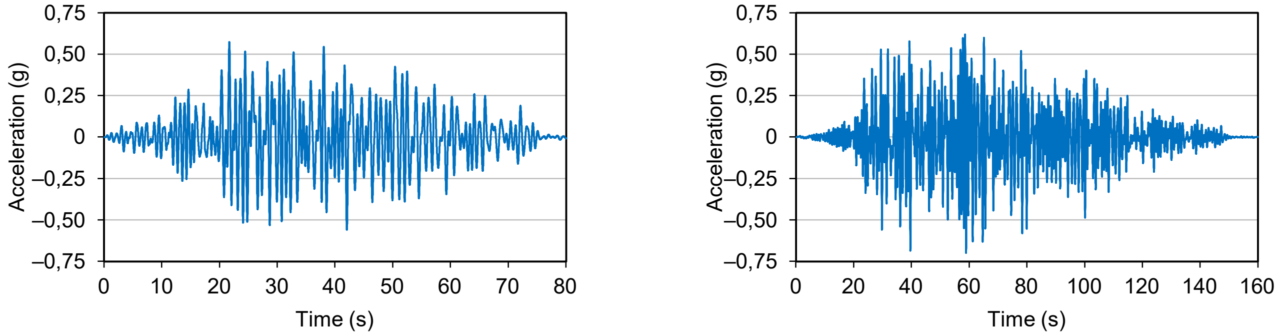

(a) (b)

Figure 4.9. PSW time histories in Scenario 2. (a) SDW; (b) LDW.

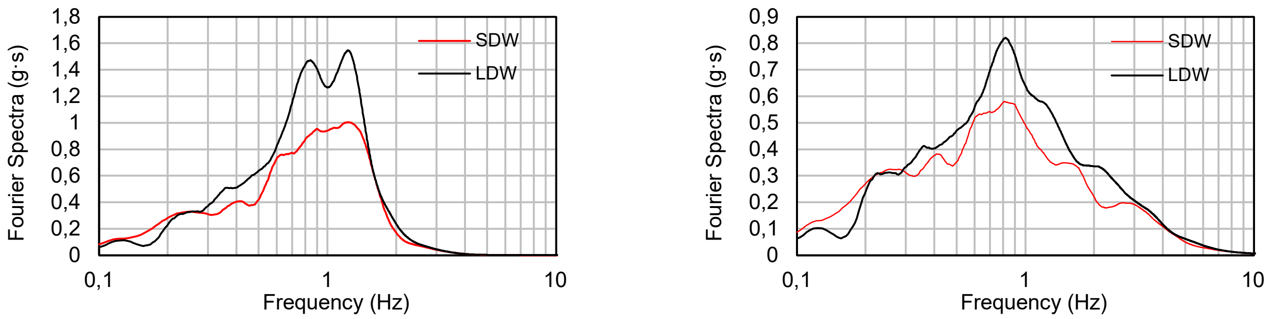

(a) (b)

Figure 4.10. Fourier spectra in Scenario 2. (a) PSW; (b) ground surface.

4.3.2. PSW displacement

Figure 4.11 illustrates the horizontal displacement time history of the PSW in Scenarios 1 and 2 owing to the SDW measured at the wharf deck's upper right (seaward) end. Here, the seaward displacement was defined as positive. Scenario 1 produced a maximum displacement of 0.55 m, less than scenario 2's maximum displacement of 0.95 m. In scenario 1, the PSW's residual displacement was 0.1 m, while in scenario 2, it was 0.6 m. Scenario 2 accounted for the residual displacement of the soil slope, whereas scenario 1 did not. The horizontal residual ground displacement contour map is shown in Figure 4.12. In scenario 1, the residual ground displacement nearby the

PSW was minor, around 0.4–0.1 m. In contrast, the residual ground displacement in Scenario 2 was significant, measuring between 1.2–0.5 m.

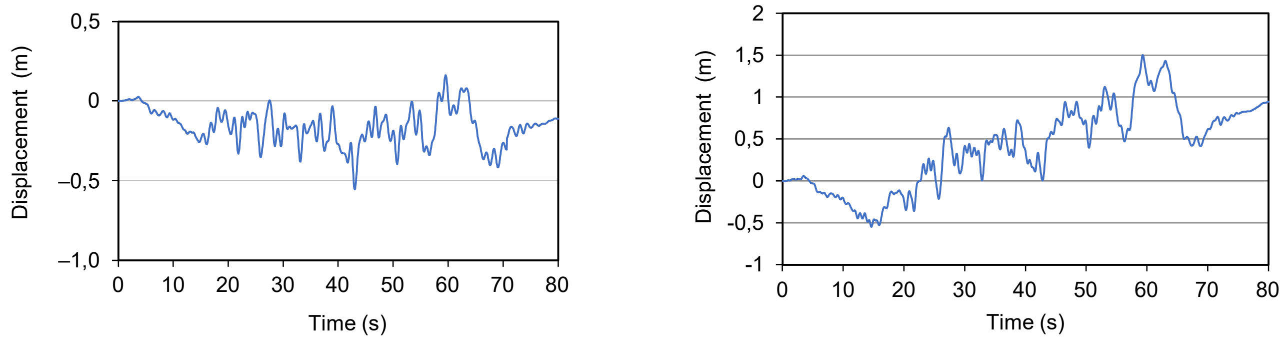

(a) (b)

Figure 4.11. PSW horizontal displacement due to the SDW. (a) Scenario 1; (b) Scenario 2.

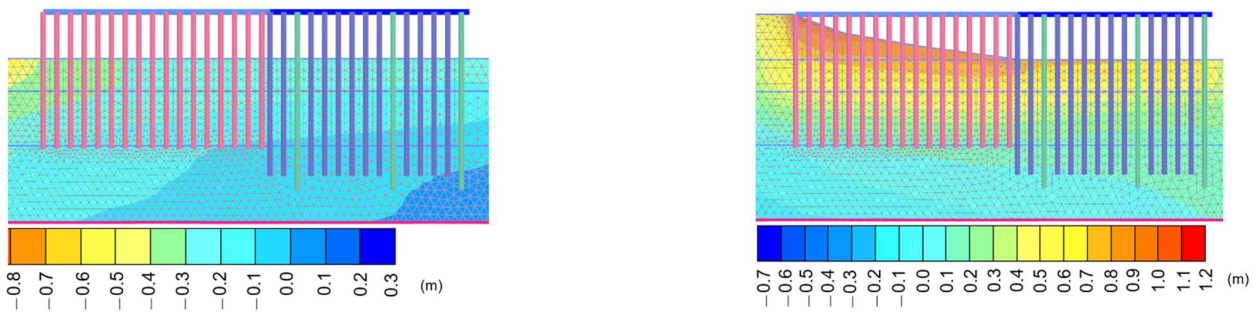

(a) (b)

Figure 4.12. Horizontal residual ground displacement due to the SDW. (a) Scenario 1; (b) Scenario 2

Figure 4.13 depicts the horizontal displacement history of the PSW in scenarios 1 and 2 due to the LDW. Scenario 1 had a maximum displacement of 0.85 m, less than Scenario 2's 1.35 m. Scenario 1's residual displacement was 0.15 m, while scenario 2's was 0.95 m. Figure 4.14 depicts the contour map of horizontal residual ground displacement by the LDW. In scenario 1, the residual ground displacement near the PSW was between 0.5 and 0.1 meters. In contrast, the residual ground displacement ranged from 2.0 to 0.8 m in scenario 2. The significant displacement of the PSW in scenario 2 resulted from significant ground displacement at the soil slope, which was neglected in scenario 1. The LDW produced a more significant residual PSW displacement than the SDW. In scenario 2, a comparison of the SDW and LDW results reveals that the displacement after 70 s is nearly identical to the residual displacement and that the LDW displacement did not increase significantly after 70 s. The LDW's phase characteristics were responsible for the more significant residual displacement. Various waveforms corresponding to the target SA can be generated; therefore, seismic design practice should consider waveforms with varying phase characteristics.

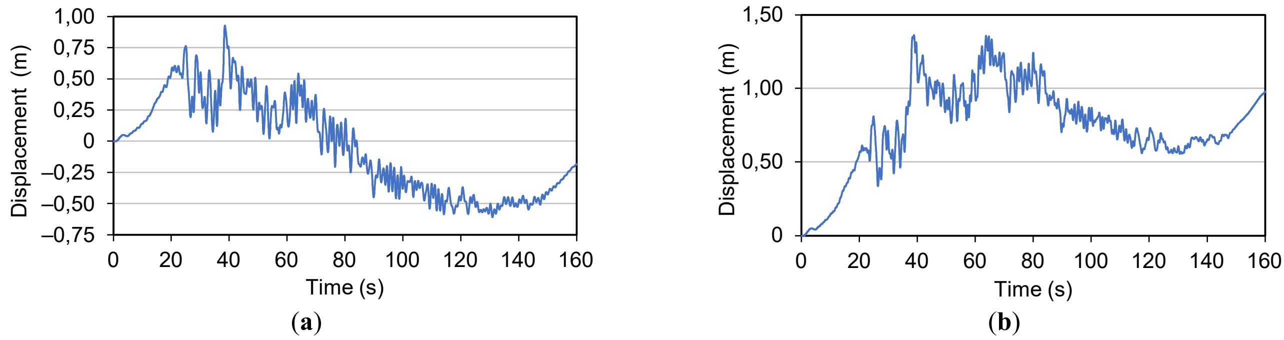

Figure 4.13. PSW horizontal displacement due to the LDW. (a) Scenario 1; (b) Scenario 2.

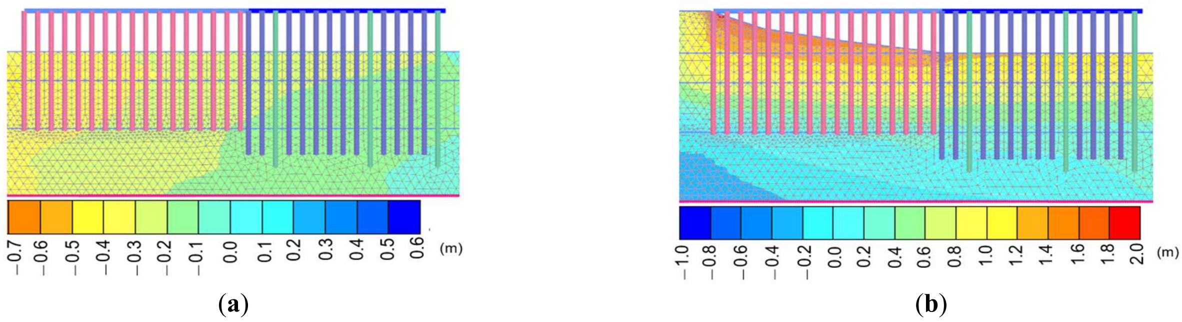

Figure 4.14. Horizontal residual ground displacement due to the LDW. (a) Scenario 1; (b) Scenario 2.

Figure 4.15 and 4.16 depicts the vertical settlement time history of the PSW piles in Scenarios 1 and 2 measured at the bottom of the first pile at the trestle (i.e., P1) and the first pile of the wharf (i.e., P1A), due to LDW and SDW, respectively. For the LDW waveform, scenario 1 produced a maximum trestle settlement of 0.025 m, less than scenario 2's maximum trestle settlement of 0.17 m. Whereas for wharf settlement, scenario 1 produced a settlement of 0.016 m, slightly smaller than scenario 2 of 0.02 m. For the SDW waveform, scenario 1 produced a maximum trestle settlement of 0.020 m, less than scenario 2's maximum trestle settlement of 0.10 m. Whereas for wharf settlement, scenario 1 produced a settlement of 0.010 m, slightly smaller than scenario 2 of 0.018 m.

Comparing results from LDW and SDW waveforms, the latter produced a smaller settlement than the first. The differences occurred due to the different phase characteristics of the waveforms. As depicted in Figures 4.8a and 4.10a, the LDW produces more significant PSW Fourier spectra than the SDW at the natural period of PSW. At all waveform duration, scenario 2 gives a more substantial settlement value than scenario 1 because it considers the soil slope in the analysis, whereas scenario 1 does not. The settlement of the pile at the trestle was more significant than the wharf; the difference is because the pile in the trestle is close to the soil slope, affected more by soil deformation. Moreover, the pile in the trestle rested above the hard soil layer (i.e., friction pile), whereas the pile in the wharf rested inside the hard layer (i.e., end bearing pile); therefore, the pile in the wharf had more lateral and vertical resistance against the soil deformation.

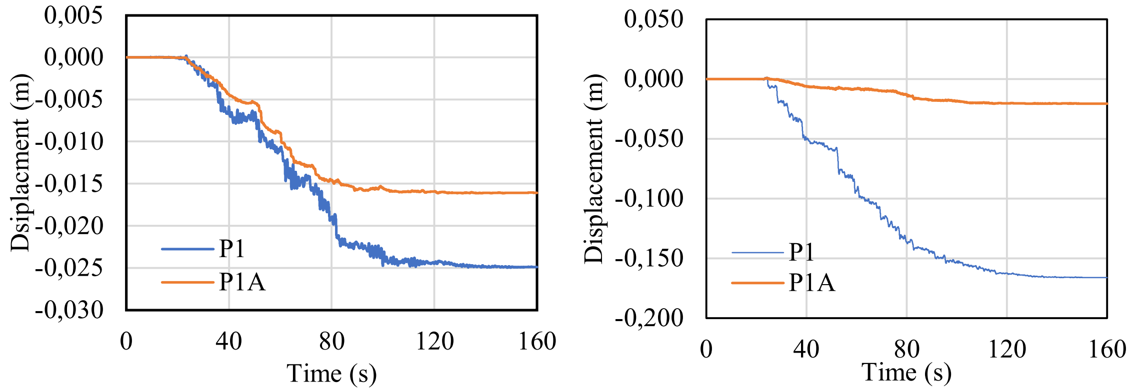

(a) (b)

Figure 4.15. Settlement of pile due to the LDW. (a) Scenario 1; (b) Scenario 2.

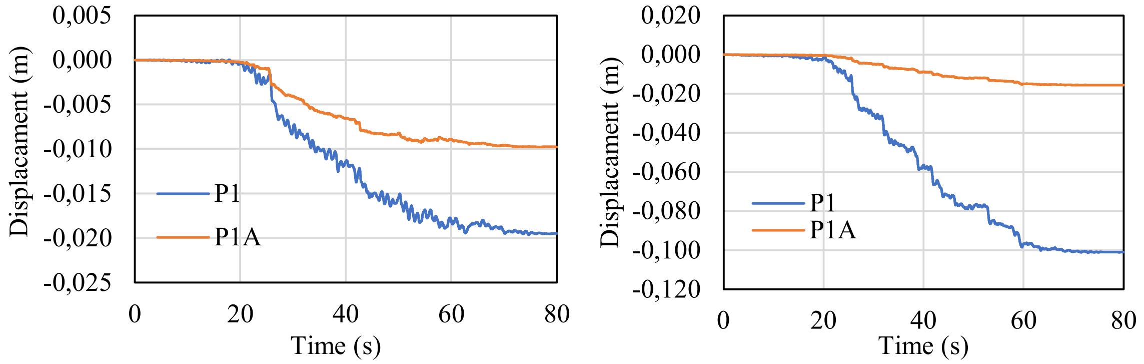

(a) (b)

Figure 4.16. Settlement of pile due to the SDW. (a) Scenario 1; (b) Scenario 2.

4.3.3. Bending moment of piles

Figures 4.17–4.22 depict the pile bending moment distributions resulting from the SDW and LDW. The figures are snapshots in which the pile bending moment reaches its largest value at a particular location within the pile. The piles are numbered consecutively from the left side (lowest number) to the right side (highest number). The Ø1000, Ø1100, and Ø1200 mm piles are labeled P1–P17, P1A–P12A, and P1B–P3B, respectively. The most significant bending moments were measured at the pile heads in every case. Significantly high maximum bending moments were observed in piles with a diameter of 1200 mm.

In Scenario 1, no pile reached the plastic bending moment when the SDW was employed, but the plastic bending moment was reached in the Ø1200 mm pile when the LDW was employed. In Scenario 2, plastic bending moments were reached at piles Ø1000, Ø1100, and Ø1200 mm for SDW and LDW. The bending moment of the Ø1200 mm pile was large in Scenario 1 because the Ø1200 mm pile had the most significant inertia force among the piles due to its highest rigidity. In Scenario 2, in addition to those above, the Ø 1000 mm piles were significantly affected by the ground displacement at the slope, resulting in a significant bending moment, particularly in the piles near the top of the slope.

Concerning the bending moment distribution beneath the ground's surface, scenario 1 specified that the largest bending moment occurs at shallow underground points. This bending moment profile is consistent with that of the beam on the Winkler foundation [83]. Scenario 2 results, on the other hand, did not produce the maximum moment of bending at shallow points in the soil layer. The reason is that the ground's stiffness and subgrade reaction decreased in the shallow portion of the ground due to slope displacement. In contrast, significant bending moments were observed at the interface between Clay 2 and Clay 3 in the results of scenario 2. This exact mechanism caused buckling at the deep underground position of the PSW piles at Kobe Port during the 1995 Kobe Earthquake due to the high impedance contrast between soil layers [84]. Due to the gentle slope of the study's target wharf, plasticization of the pile did not happen in the underground portion. However, it should be noted that seismic design practices disregarding slope displacement may result in unsafe design, even for underground points.

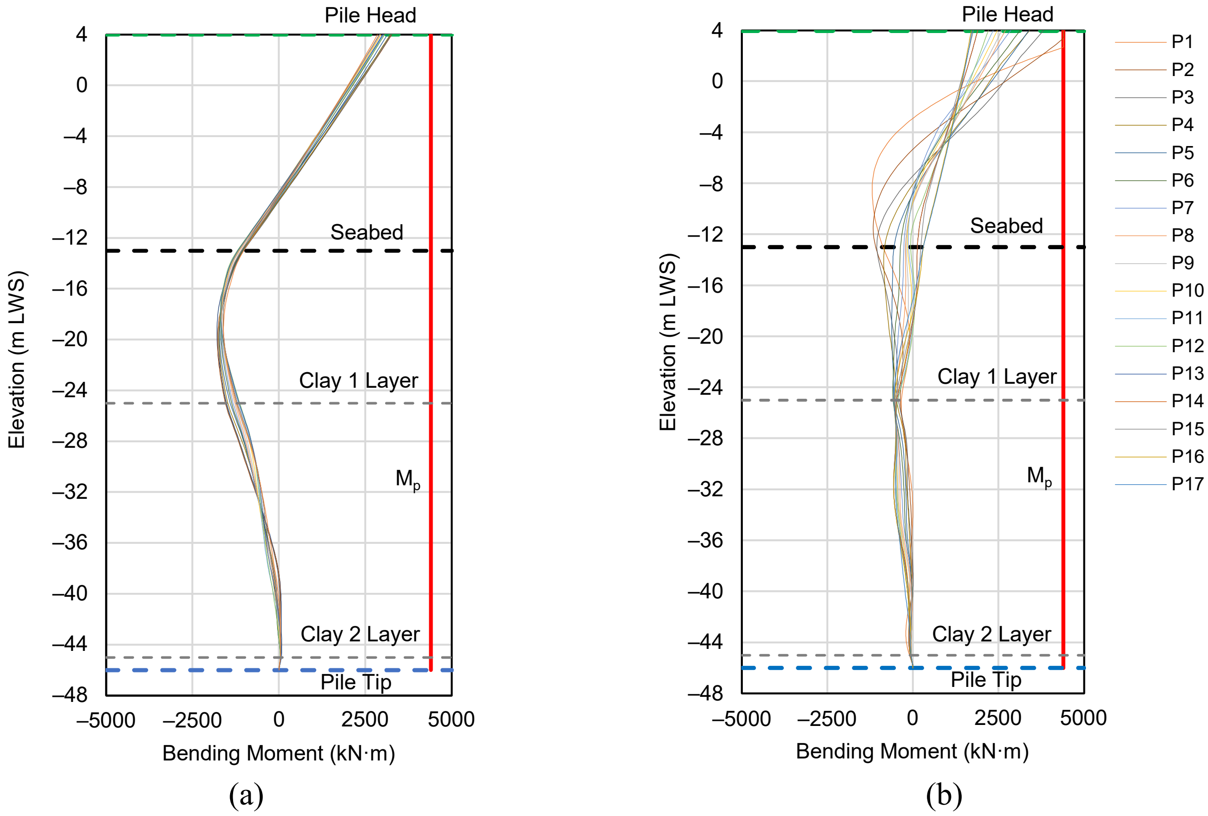

Figure 4.17. Bending moment distribution of Ø1000 mm pile due to the SDW. (a) Scenario 1; (b) Scenario 2.

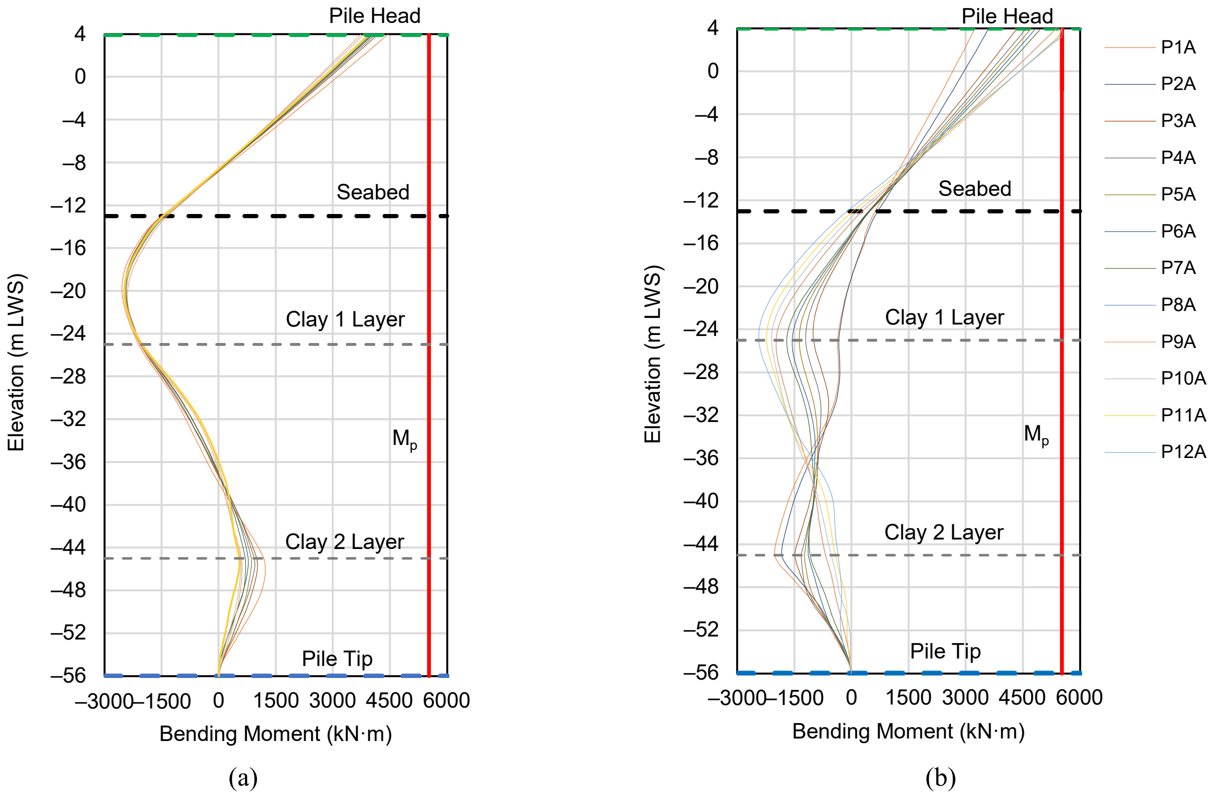

Figure 4.18. Bending moment distribution of Ø1100 mm pile due to the SDW. (a) Scenario 1; (b) Scenario 2.

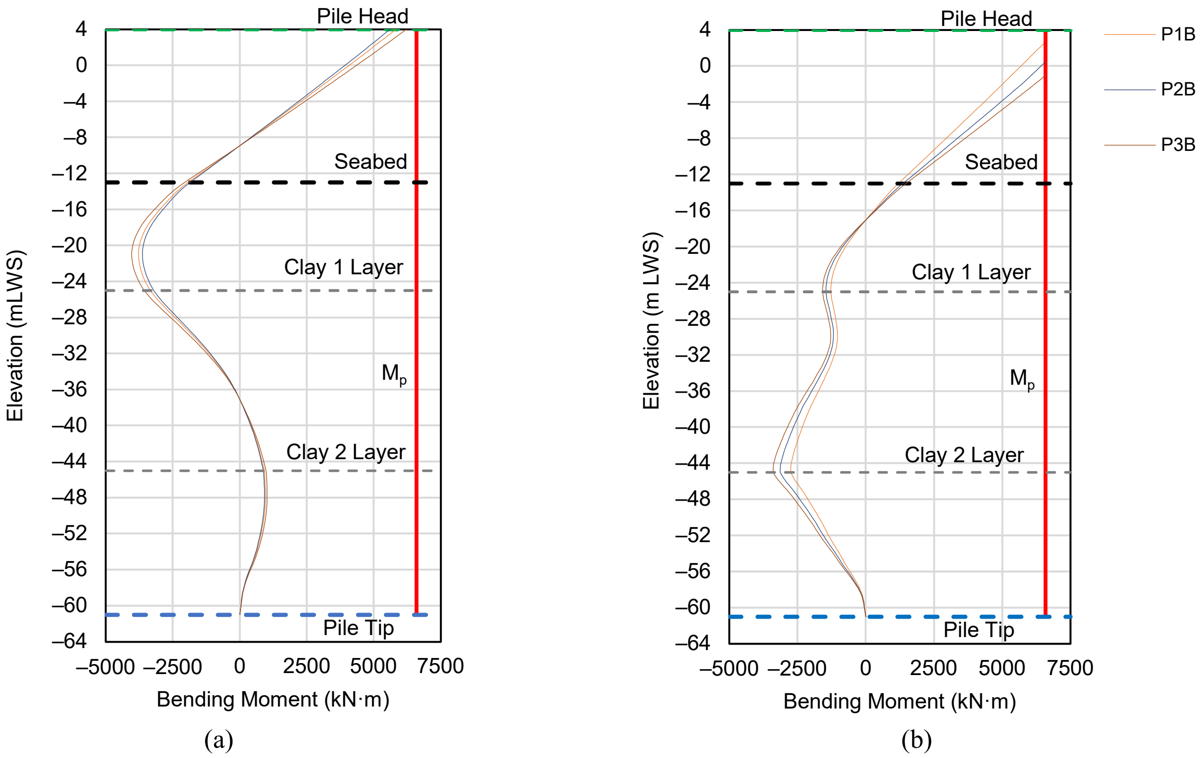

Figure 4.19. Bending moment distribution of Ø1200 mm pile due to the SDW. (a) Scenario 1;(b) Scenario 2.

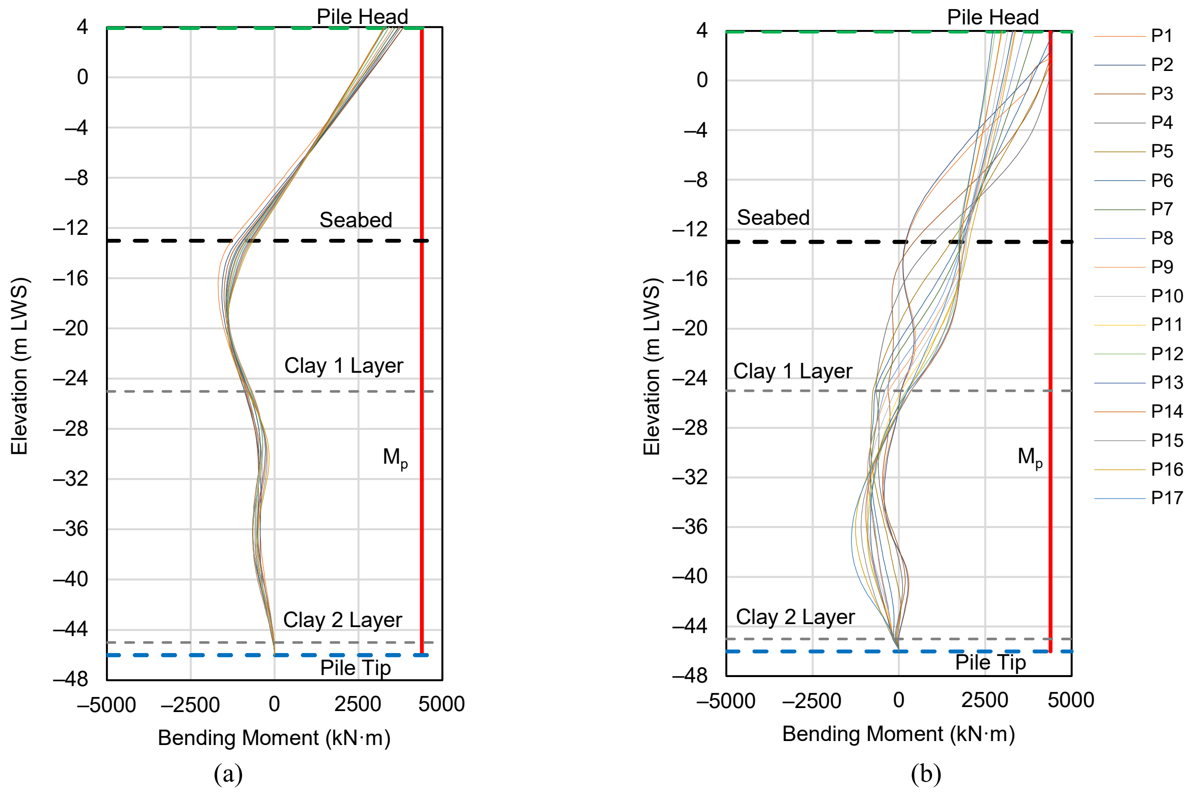

Figure 4.20. Bending moment distribution of Ø1000 mm pile due to the LDW. (a) Scenario 1; (b) Scenario 2.

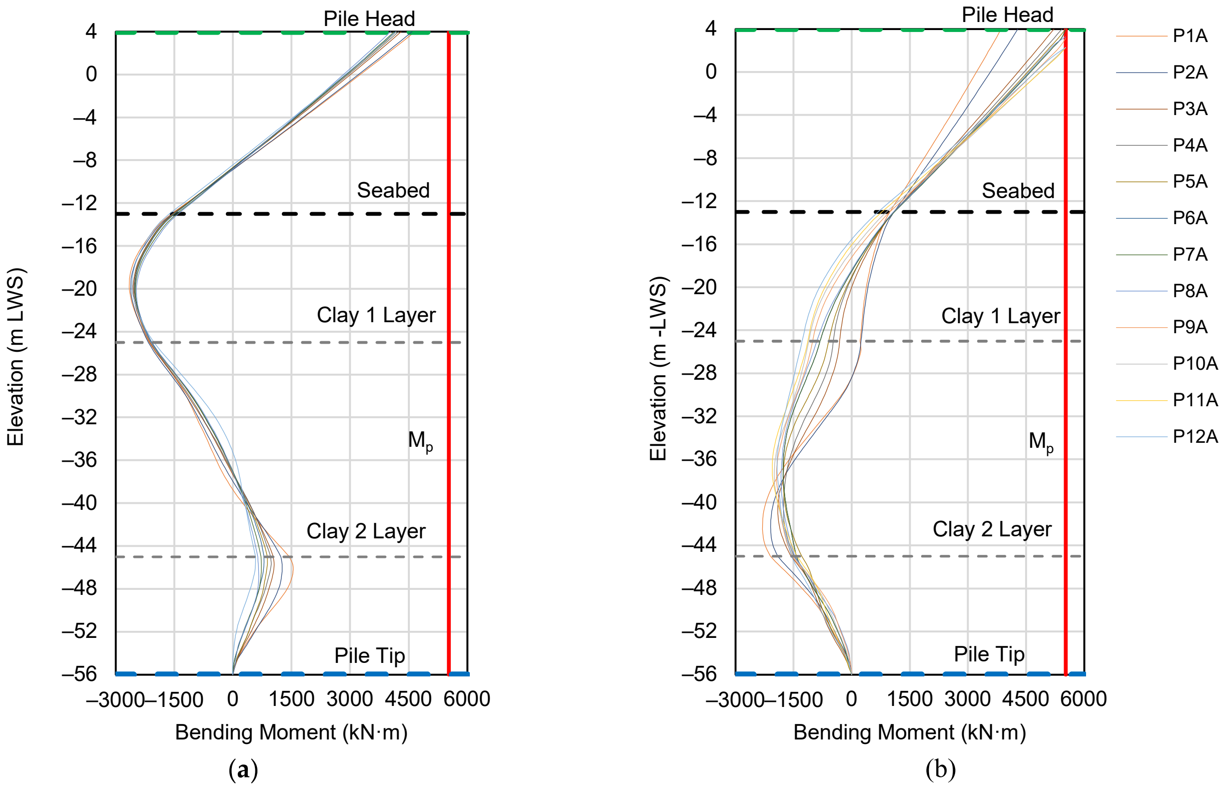

Figure 4.21 Bending moment distribution of Ø1100 mm pile due to the LDW. (a) Scenario 1;(b) Scenario 2.

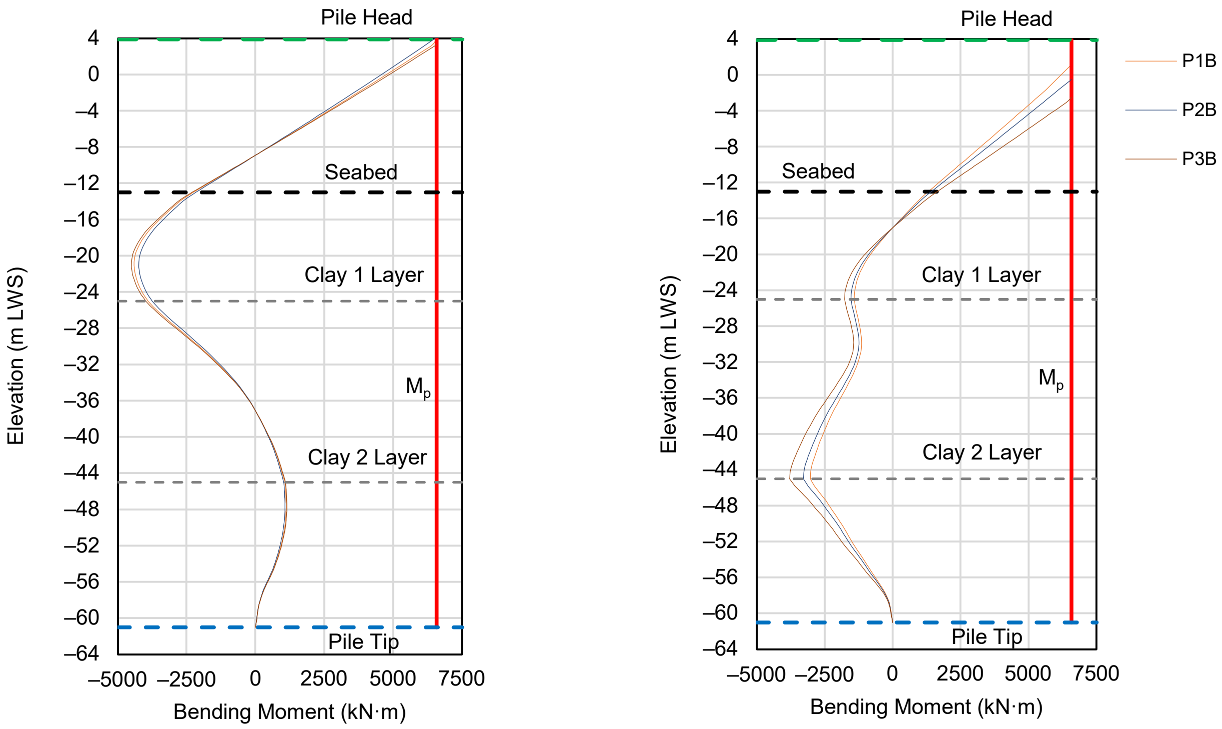

(a) (b)

Figure 4.22 Bending moment distribution of Ø1200 mm pile due to the LDW.
(a) Scenario 1; (b) Scenario 2.

Figures 4.23 and 4.24 depict the time histories of bending moments at the Ø1200 mm pile head resulting from the SDW and LDW, respectively. Comparison of the piles' bending moment time history with the PSW's acceleration and displacement time histories in scenario 1 reveals a relationship between amplitude patterns; significant acceleration and displacement correspond to a considerable bending moment and vice versa. For example, figures 4.7a, 4.11a, and 4.21a display significant acceleration, displacement, and bending moment values for the SDW in scenario 1 over the 17–52 s. At 43 seconds, the maximum values of pile bending moment, PSW acceleration, and displacement coincided. In addition, the smallest value occurred between 0 and 10 seconds. This correlation exists because the structure's inertial force significantly influenced scenario 1's pile bending moments and displacement. This pattern is also present in scenario 1's LDW.

A comparison of the bending moment time history of piles and the acceleration time history of PSW in scenario 2 demonstrates that the bending moment was impacted not only by the inertial force of the structure but also by the displacement of the soil slope, which was not taken into account in scenario 1. Figure 4.23b demonstrates that the bending moment in scenario 2 was not zero at 0 s. The lateral displacement of the soil slope during the static phase causes the additional bending moment value. The horizontal residual ground displacement during the static phase is depicted in Figure 4.25. The largest horizontal residual ground displacement during the static phase of scenario 2 was 0.034 m (Figure 4.25b), which was considerably greater than Scenario 1's 0.0007 m (Figure 4.25a). Consequently, the impact of the soil displacement on the bending moment was more significant in scenario 2 than in scenario 1.

Comparing the bending moment time histories of piles at SDW under scenarios 1 and 2 illustrates the influence of the displacement at the soil slope in scenario 2. Scenario 2's bending moment (Figure 4.23b), PSW acceleration (Figure 4.9a), and PSW displacement (Figure 4.11b) are 8630 kN·m, 0.35 g, and 1.1 m, respectively, at 53 s. Whereas, at 43 s, the bending moment in scenario 1 (Figure 4.21a), PSW acceleration (Figure 4.7a), and PSW displacement (Figure 4.11a) present values of 6315 kN·m, 0.55 g, and 0.55 m, respectively. These values indicate that the smaller acceleration in scenario 2 (i.e., 0.35 g) could result in a more significant bending moment (i.e., 8630 kN·m) due to the impact of the more significant displacement (i.e., 1.1 m). A comparison of Figures 4.23a and 4.24a reveals that the duration of the waveform can affect the large bending moment value. In scenario 1, for instance, LDW produces a greater bending moment of 6950 kN·m (Figure 4.24a) than SDW of 6315 kN·m (Figure 4.23a). Scenario 2 also demonstrates a similar distinction. This difference results from the different phase characteristics of the SDW and LDW used in this study, as shown in Figures 4.8a and 4.10a, in which the LDW produces more significant PSW Fourier spectra than the SDW at the natural period of PSW.

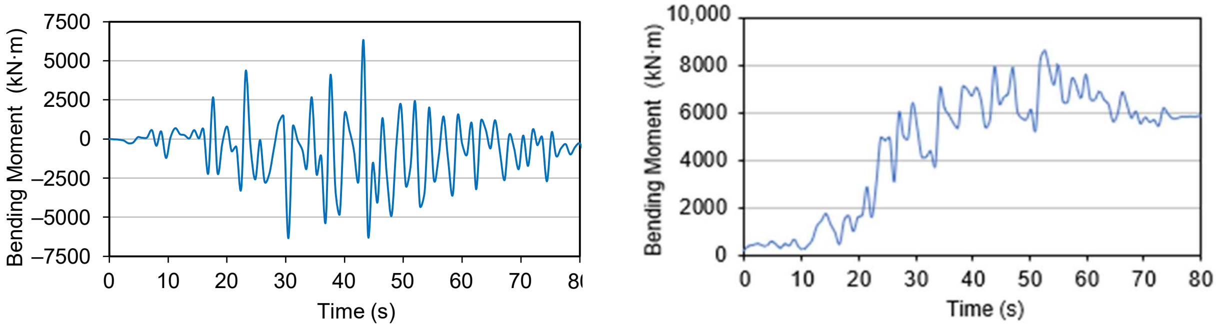

(**a**) (**b**)

Figure 4.23. Bending moment time history of the pile due to the SDW. (a) Scenario 1; (b) Scenario 2.

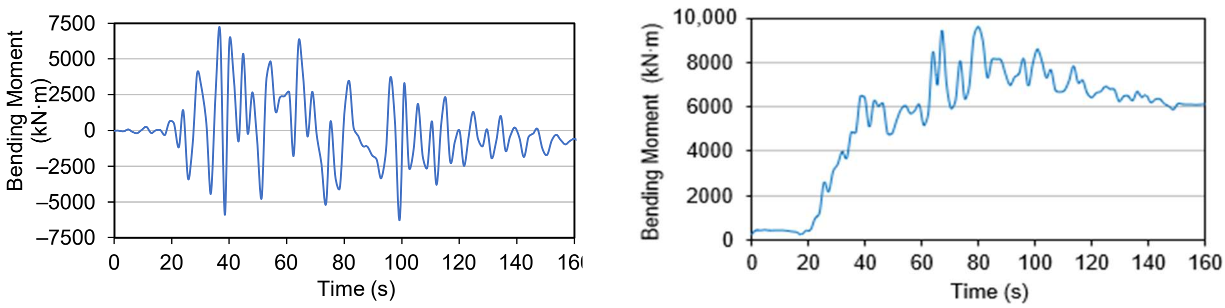

(**a**) (**b**)

Figure 4.24. Bending moment time history of the pile due to the LDW. (a) Scenario 1; (b) Scenario 2.

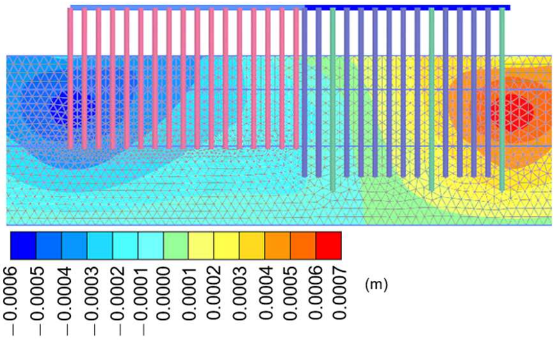

(**a**)

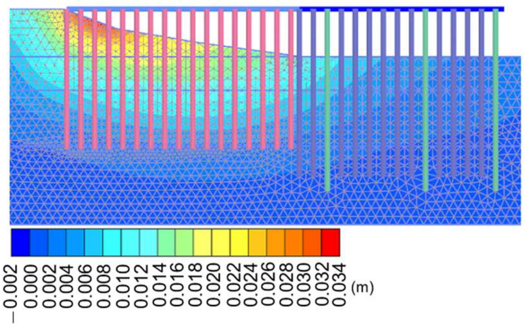

(**b**)

Figure 4.25. Horizontal residual ground displacement before earthquakes. (a) Scenario 1; (b) Scenario 2.

CHAPTER 5. SEISMIC PERFORMANCE EVALUATION OF PILE-SUPPORTED WHARFS USING 2D FRAME ANALYSIS

5.1. Introduction

The piles of PSWs are subject to the inertial force transferred from the wharf's deck and the kinematic force induced by the soil slope's ground movement during earthquakes. In general, the latter is more damaging since the lateral resistance of the pile is reduced during earthquakes [11]. In the case of piles buried in a soil slope, kinematic force generates a considerable bending moment [12]. PSWs with soil slopes have shorter natural periods than PSWs without slopes. In addition, because the amplitude of the spectral acceleration (SA) is often large in the short period range, ignoring the soil slope in seismic design can lead to unsafe design, even if the kinematic force is small.

Using soil-structure FEA, the seismic performance of PSWs can be accurately determined. Earlier chapters have covered the seismic responses of PSWs using this approach. In FEA, the structure and soil layer are modeled, and complicated cases are solved, such as the soil-structure interaction in the case of earthquake-induced lateral spreading. However, FEA is rarely used in design practice since it is time-consuming and requires specialized simulation tools. In contrast, frame analysis (FA) is a less complex approach for studying the seismic response of a PSW; therefore, FA is the typical method used in design practice. However, FA has limitations, such as the inability to account for ground deformation caused by earthquakes.

The SA-estimated inertial force is applied as a static load to the PSW deck. The magnitude of SA depends on the damping coefficient, and the value generally used in PSW engineering design is 0.03–0.05, with a PSW width between 20 and 60 meters. As for PSWs with a width greater than 100 meters, the generally used damping coefficient may not be suitable. Therefore, a procedure for estimating the damping coefficient of wide PSWs must be developed.

Numerous research, including those by Tamura [85] and Smith et al. [86], have found possible aspects that may influence the damping of a structure, such as material damping, structural connections, foundations, building height, and the hysteresis of yielding components. Iwashita and Hakuno [87] discovered that the damping coefficient increases with the depth of the foundation. Tamura [85] proposed prediction methods for the damping coefficient created mainly for buildings. A simplified procedure for estimating the damping coefficient for the PSW's design has not yet been made.

Some researchers have examined the influence of kinematic forces on the design of piles. The Japan Road Association (JRA) formulated a popular formula for calculating kinematic force [88]. The formula assumes a triangular distribution of soil pressure that varies with soil density, pile length, and pile diameter. The JRA code suggests that designers evaluate bending moment separately due to kinematic and inertial forces. Dobry et al. [24] thoroughly investigated the kinematic force by conducting six centrifuge model tests on single-pile and proposed a soil pressure on piles of 10.3 kPa. Based on shaking table test results, He et al. [12] proposed that the soil pressure on piles was equal to the gross overburden pressure. Haigh and Madabhushi [26] measured 16 kPa of homogeneous soil pressure on piles within a liquefiable layer. Using data from a single pile shaking table test, Tang et al. [25] suggested a uniform pressure of 19.5 kPa.

Based on test results, existing models of lateral spreading soil pressure have been developed; nevertheless, considerable disparities have been detected between the soil pressures from previous research. Therefore, deciding on the appropriate kinematic force for pile design is complicated. Moreover, the proposed soil pressure models were derived mostly from the outcomes of single-pile testing. According to the FEA results of PSW pile groups on a mild soil slope, the soil pressure becomes smaller as the distance from the slope's crest increases [27]. Therefore, models of soil pressure based on single-pile tests are inapplicable to pile group situations. Thus, an approach must be established to calculate the kinematic forces acting on pile groups at a soil slope.

In general, only inertial force has been considered in the seismic design of PSWs using FA; the impact of kinematic force on a mild soil slope is frequently ignored. In addition, the difference in the damping coefficient due to a change in PSW width is usually ignored in design practice, which may result in overdesign. Due to the lack of study on the impacts of kinematic force and the damping coefficient on the seismic performance of a wide PSW on a mild slope, this chapter’s purpose is to establish a procedure for predicting these variables.

The damping coefficient applied to determine SA is assumed to change depending on the width of the PSW. Therefore, this research proposes a procedure for determining the optimal damping coefficient for determining SA based on the width of the PSW by using PSW cross sections of varying widths and performing FEA. A procedure for determining the kinematic force to be used in FA was proposed using the FEA results.

5.2 Methods

5.2.1 Target PSW

The target PSW is constructed with a steel pipe piling foundation and a reinforced concrete deck. Fourteen PSW models with varying widths were created. To explore the influence of soil slope displacement, the FEA was applied to scenario 1 without a soil slope and scenario 2 with a soil slope. Figure 5.1 depicts the target PSW and ground configurations for scenario 1, and Figure 5.2 depicts scenario 2. The deck is +4.00 m above the low water spring (LWS). The deck is supported by steel pipe piles with (Ø) 1100 and 1200 mm diameters that rest on the seabed at −13 m LWS. The trestle has a reinforced concrete deck and steel pipe piles measuring 1000 mm in diameter. The wharf and trestle are interconnected and respond to earthquakes as a unit. The soil properties used in this chapter were the same as in the previous chapter (Table 4.2).

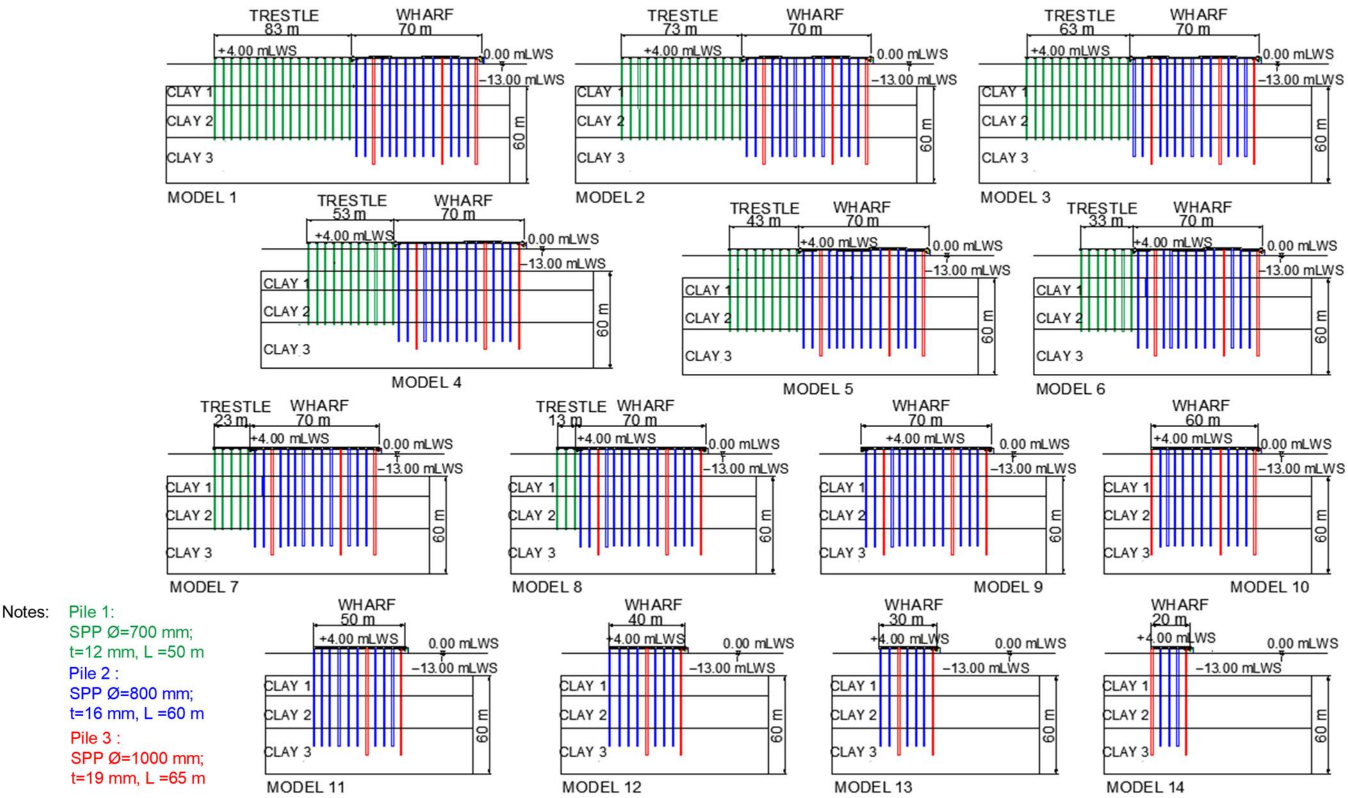

Figure 5.1 Scenario 1 (without a soil slope) pile-supported wharf configurations.

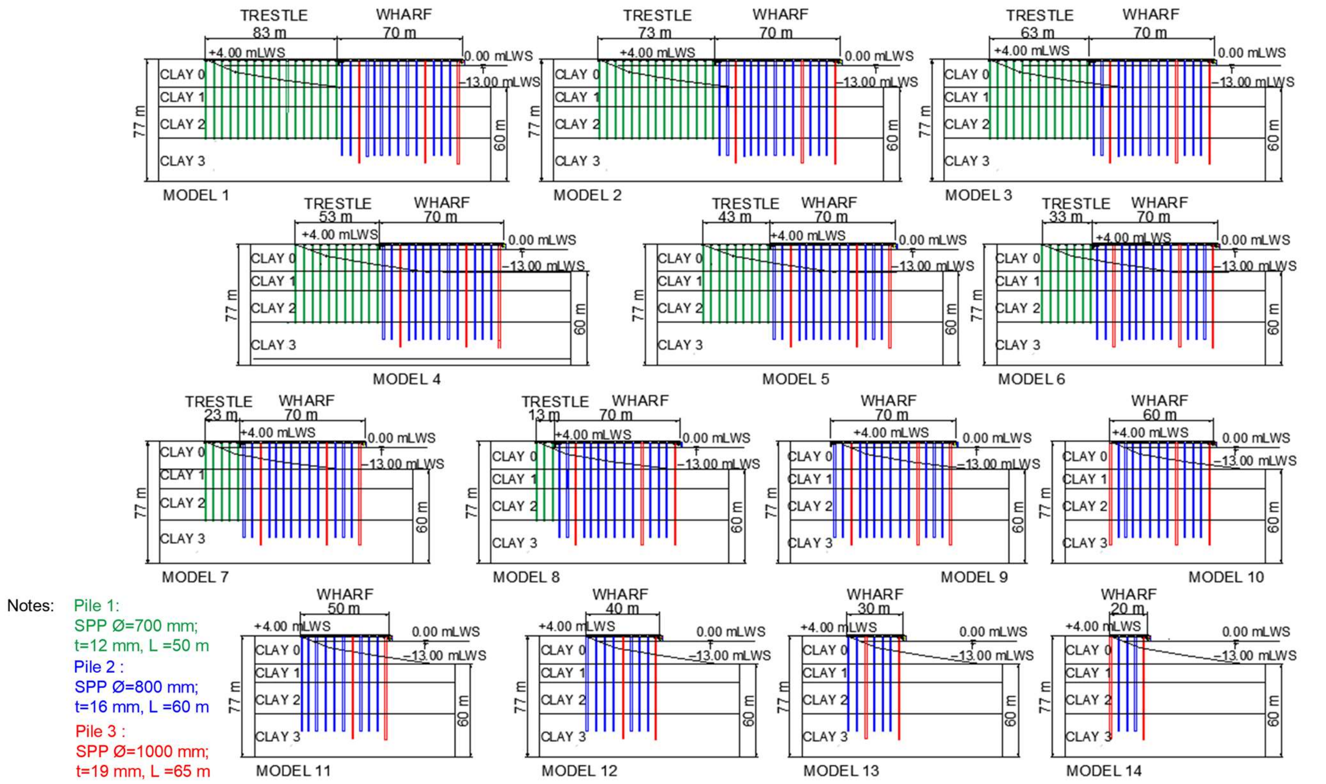

Figure 5.2 Scenario 2 (with a soil slope) pile-supported wharf configurations.

5.2.2 Finite element and frame analysis modeling

The PLAXIS 2D [69] program was used to create a 2D FEA model. The typical model developed in PLAXIS was the same as in Figure 4.2. The configuration in loading phases, boundaries, mesh coarseness, soil models, and structural elements used in the PLAXIS was the same as in previous Chapter 4.

The models utilized two waveforms with distinct characteristics: the 1968 Tokachi-Oki earthquake (TE) and the 2020 Mentawai earthquake (ME). The ME waveform was altered to fit the target SA from SNI site class SE [81]. As depicted in Figure 5.3, these waveforms were deconvoluted at the bedrock, and the maximum acceleration and duration were 0.210 g and 19 s for the TE and 0.215 g and 130 s for the ME, respectively. Numerous vital structures (e.g., PSW) have been constructed to maintain their elasticity during earthquakes, as the inelastic behavior of the structure might have fatal effects. Focusing on the elastic response of the PSW, the waveforms were multiplied by 0.8 to limit their amplitude, ensuring that the structural elements evaluated during the earthquake remained in an elastic condition.

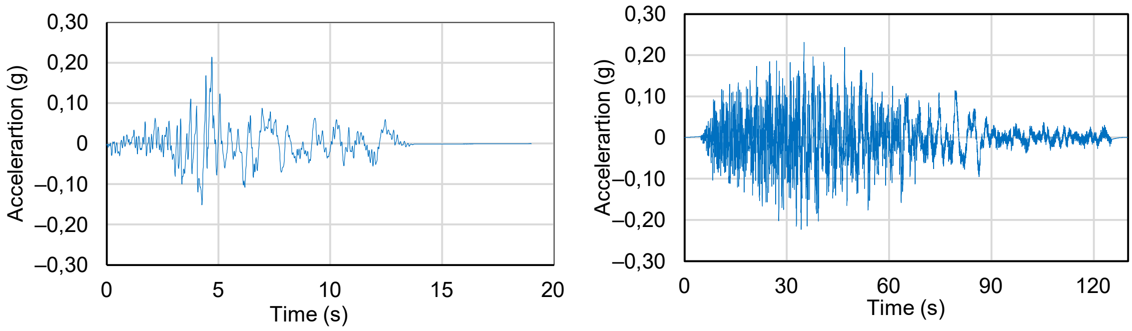

(a) TE waveform (b) ME waveform

Figure 5.3 Input waveforms

The SAP 2000 [89] program was utilized to develop a 2D FA model (Figure 5.4). As rigidly connected frame elements, piles and beams were modeled. To model the relationship between the soil reaction (P) and lateral displacement (Y) around the piles for each soil layer, soil spring elastic-plastic P-Y curves were utilized. The P-Y curve used in the spring properties was computed with the L-PILE [90] software developed using Matlock research [91]. The P-Y curves at various depths beneath the seabed are depicted in Figures 5.5–5.7. Figure 5.5 illustrates that the greatest soil resistance for the Ø1000 mm pile at a depth of 1 m for scenario 1 is 26.5 kN, and for scenario 2, it is 11.1 kN. This discrepancy is due to the different properties of the surface soil layers in scenarios 1 and 2, with the undrained cohesion of the surface layer (Clay 1) in scenario 1 being larger than the surface layer in scenario 2 (Clay 0). The undrained cohesion was established using a correlation equation with N-SPT [92]. Figures 5.6 and 5.7 depict the largest soil resistance for the Ø 1100 and Ø 1200 mm piles at 1 m depth, which was 29 kN for scenario 1 and 31 kN for scenario 2. Generally, the P-Y curve indicates that the greater the pile diameter, the greater the soil resistance.

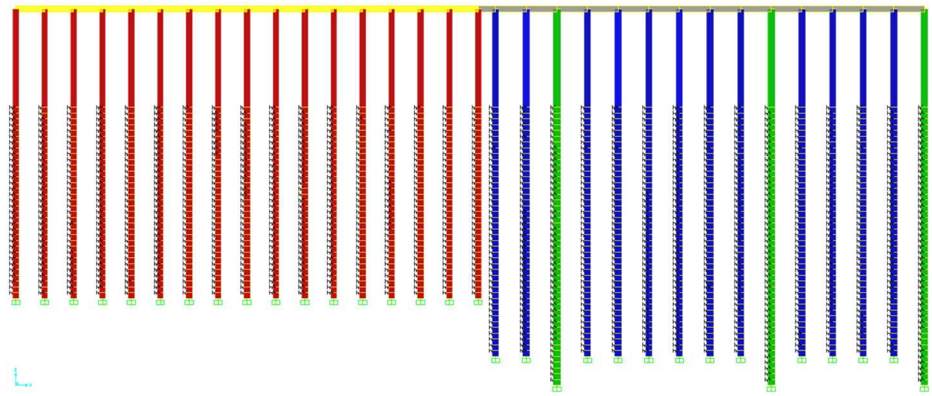

(a) Scenario 1

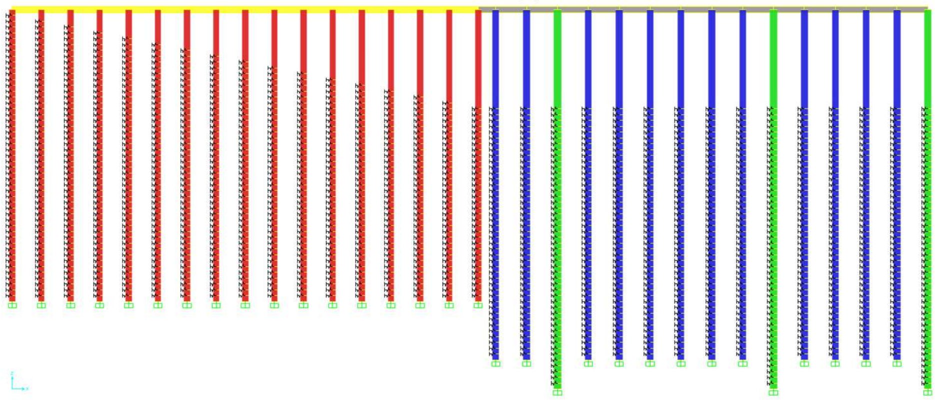

(b) Scenario 2

Figure 5.4 Typical FA model of the PSW.

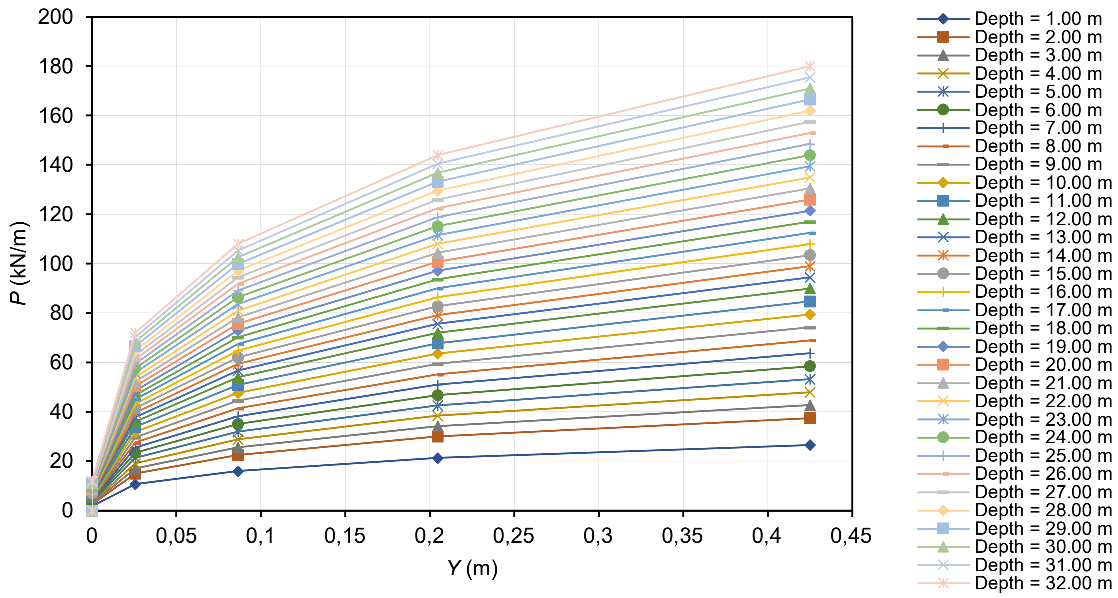

(a) Scenario 1

Figure 5.5 *Cont.*

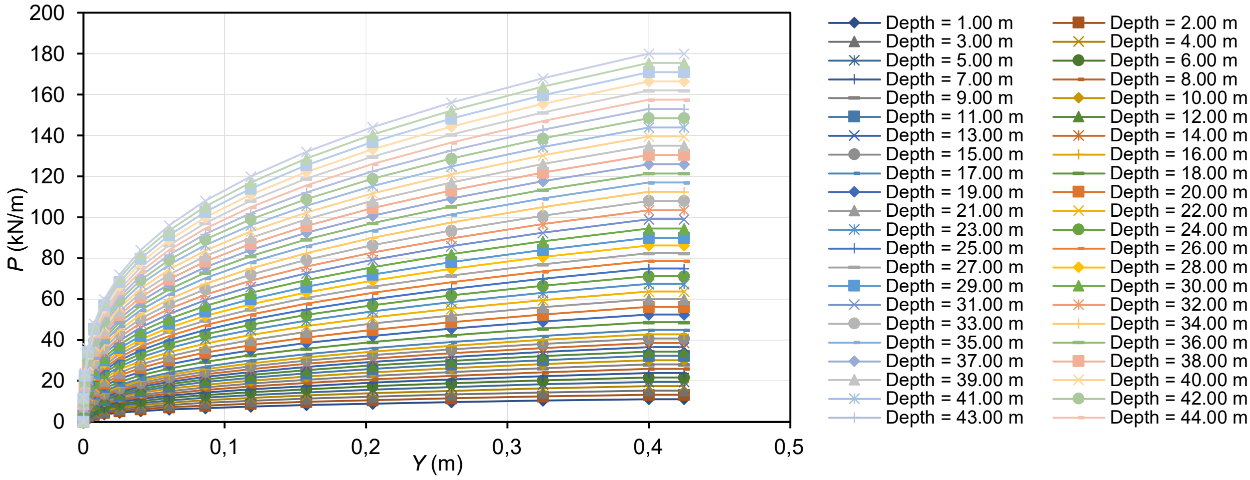

(b) Scenario 2

Figure 5. 5 P-Y curves for Pile 1 (Ø1000 mm)

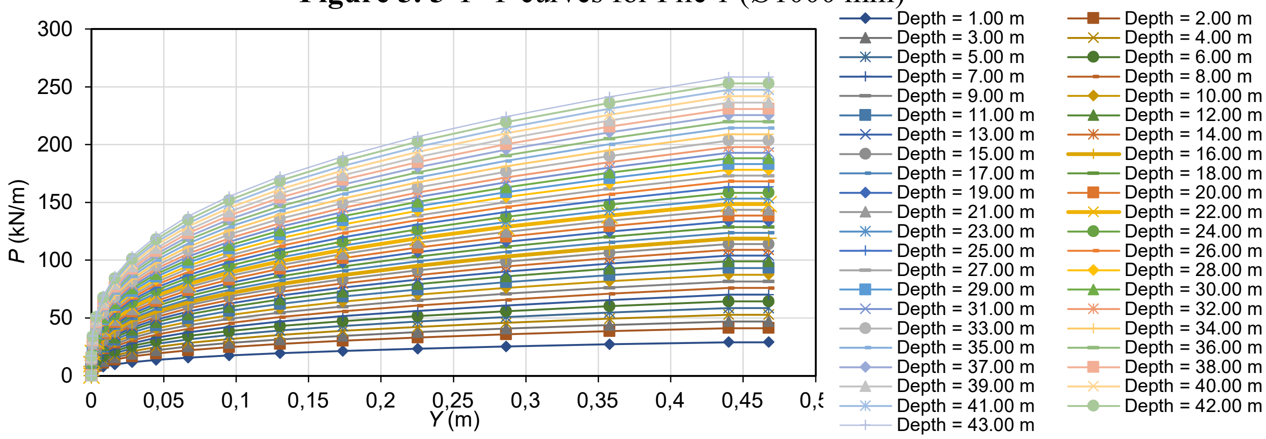

Figure 5.6. P-Y curves for Pile 2 (Ø1100 mm).

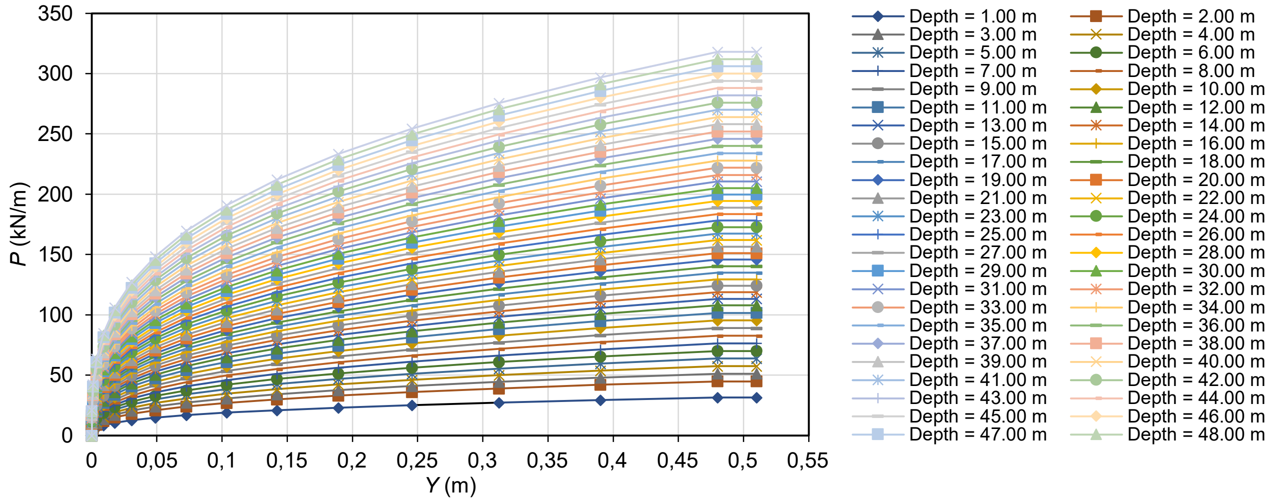

Figure 5.7. P-Y curves for Pile 3 (Ø1200 mm).

5.2.3 Method for determining the inertial force.

Using the static equivalent method, the PSW's inertial force can be calculated as a product of the PSW's total mass above the seabed and the SA at the PSW's natural period. For the FA, the inertial force was employed as a lateral force in the seaward direction at the landward end of the PSW.

For calculating the inertial force, the mass of the PSW was initially determined utilizing different PSW widths. The elastic deflection was acquired by employing a small lateral load to the PSW, and the PSW spring constant was calculated by dividing the lateral load by the deflection. Equation 5.1 was used to calculate the PSW's natural period.

$$Tn = 2\pi\sqrt{\frac{M}{K}} \qquad \text{(Eq.5.1)}$$

where *Tn* is the PSW's natural period, *K* is the PSW's spring constant, and *M* is the PSW's mass.

The ground surface waveform was then determined by conducting a 1D soil–column seismic response analysis. Utilizing DEEPSOIL software [55], a frequency domain analysis considering soil nonlinearity was performed. Vucetic and Dobry [54] were referred for the shear modulus and damping coefficient dependences on the shear strain for cohesive soil. Multiple SAs were produced at the ground's surface with various damping coefficients to calculate the inertial forces. Using these inertial forces, the damping coefficient that gives the best match between the FEA acceleration and the FA acceleration was determined.

5.2.4 Method for determining the kinematic force.

To account for slope displacement in the FA, the kinematic force was calculated employing the soil residual displacement distribution in front of the pile according to FEA results. The kinematic force was calculated using the P-Y curves depicted in Figures 5.5–5.7. Regarding the residual displacement from the FEA, the soil reaction value in the P-Y curve was set as the kinematic force.

This chapter also compared kinematic loading utilizing the JRA method [87]. Considering a single pile, the JRA method depicted in Equation 5.2 was utilized to determine the triangular-shaped distribution of soil pressure alongside the pile.

$$ql = Cs \times CL \times \gamma L \times z \times D \qquad \text{(Eq.5.2)}$$

where *Cs* is the modification factor, which is set to 1 for pile lengths less than 50 m, 0.5 for pile lengths between 50 and 100 m, and 0 for pile lengths larger than 100 m, *CL* is the lateral pressure factor, which is generally set to 0.3, L is the average unit weight of the soft soil layer (kN/m^3), *z* is the pile depth beneath the ground surface (m), and *D* is the pile diameter (m).

5.3 Results and discussion

5.3.1 Inertial force

Table 5.1 displays the PSW masses and natural periods determined using Equation 5.1. Model 1 has the most significant PSW mass due to its largest width. Scenario 2 generates a lesser PSW mass and natural period than scenario 1 due to scenario 2's shorter pile height above the seabed.

Table 5.1. PSW masses and natural periods.

Model Number	Scenario 1		Scenario 2	
	M (kg)	*Tn* (s)	*M* (kg)	*Tn* (s)
1	870,522	1.209	830,765	1.015
2	823,790	1.206	788,711	1.014
3	777,059	1.208	746,657	1.010
4	730,327	1.213	704,603	1.008
5	683,596	1.212	662,549	1.002
6	636,865	1.223	620,495	0.997
7	590,133	1.227	578,440	0.996
8	543,402	1.238	536,386	0.995
9	478,910	1.242	466,804	0.994
10	412,878	1.231	402,790	0.991
11	344,646	1.230	335,567	0.990
12	278,615	1.224	271,553	0.989
13	212,584	1.209	207,540	0.987
14	146,553	1.208	143,526	0.986

Note: *Tn* is the natural period of the PSW, and *M* is the mass of the PSW.

Figures 5.8 and 5.9 depict the SAs produced by the 1D soil–column seismic response analysis employing TE and ME waveforms with a damping coefficient (ξ) of 0.01–0.07, respectively. Figure 5.8 displays that the TE waveform has a significant SA for periods shorter than 1.0 s, with the maximum SA occurring at 0.6 s and measuring 1.0 g. The ME waveform has a significant SA for periods longer than 1.0 s, with the maximum SA measuring 1.75 g at 1.75 s, as depicted in Figure 5.9.

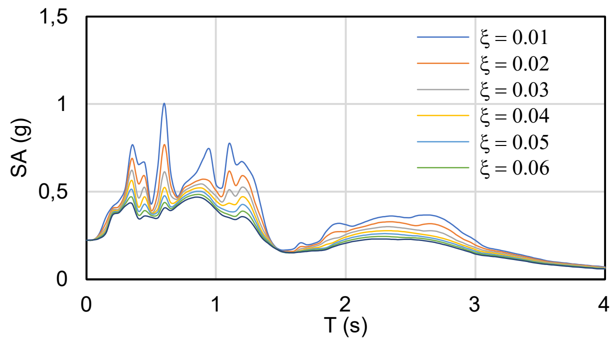

Figure 5.8. Ground surface SA of the TE waveform.

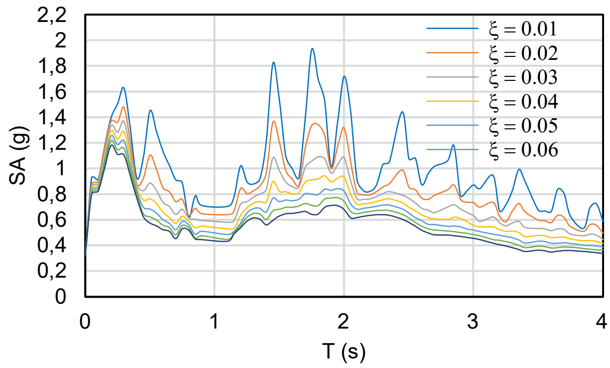

Figure 5.9. Ground surface SA of the ME waveform.

Table 3 displays the inertial force values for Scenario 1 using the TE and ME waveforms. The ME waveform produced a more significant inertial force than the TE waveform because its SA at the PSW's natural period was greater.

Table 5.2. Inertial forces for Scenario 1.

Model	ξ	*Fi* (kN)		Model	ξ	*Fi* (kN)	
		TE	ME			TE	ME
1	0.04	4553	5603	8	0.04	2802	3536
	0.05	4248	5306		0.05	2564	3220
	0.06	3880	5045		0.06	2347	2998
	0.07	3437	4814		0.07	1831	2812
2	0.04	4308	5302	9	0.04	2470	3116
	0.05	4020	5021		0.05	2259	2837
	0.06	3671	4774		0.06	2069	2642
	0.07	3252	4555		0.07	1614	2478
3	0.04	4064	5002	10	0.04	2139	2803
	0.05	3792	4736		0.05	1970	2616
	0.06	3463	4503		0.06	1802	2455
	0.07	3068	4297		0.07	1471	2316
4	0.04	3820	4701	11	0.04	1786	2339
	0.05	3564	4451		0.05	1645	2184
	0.06	3255	4233		0.06	1505	2050
	0.07	2883	4039		0.07	1228	1934
5	0.04	3575	4400	12	0.04	1450	1886
	0.05	3336	4166		0.05	1344	1779
	0.06	3047	3962		0.06	1229	1682
	0.07	2699	3780		0.07	1046	1596
6	0.04	3315	4311	13	0.04	1112	1368
	0.05	3073	4067		0.05	1037	1296
	0.06	2809	3846		0.06	947	1232
	0.07	2392	3648		0.07	839	1176
7	0.04	3058	4006	14	0.04	766	943
	0.05	2816	3739		0.05	715	893
	0.06	2576	3509		0.06	653	849
	0.07	2102	3311		0.07	579	810

Note: *Fi* is the inertial force, and ξ is the damping coefficient.

5.3.2 Kinematic force

Figures 5.10 and 5.11 depict the FEA residual displacements of the TE and ME waveforms, respectively. As the distance from the slope's top increased, the displacement decreased. The largest displacement at the top of the slope due to TE and ME waveform were 0.13 m and 0.25 m, respectively.

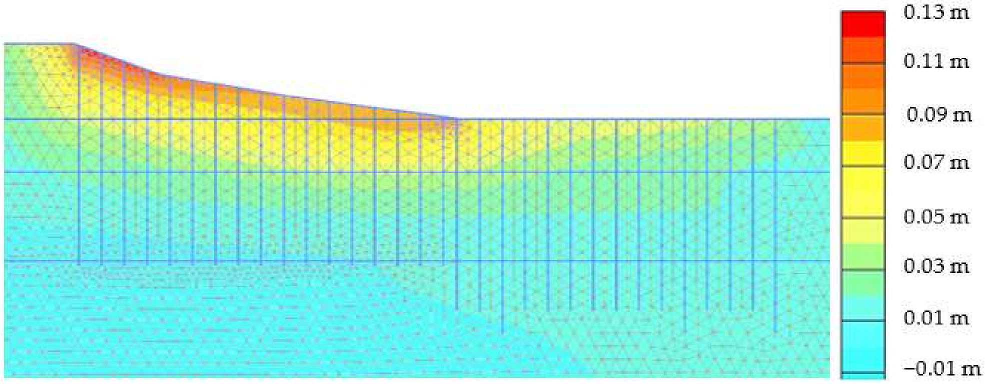

Figure 5.10. FEA of the TE waveform: Residual displacement.

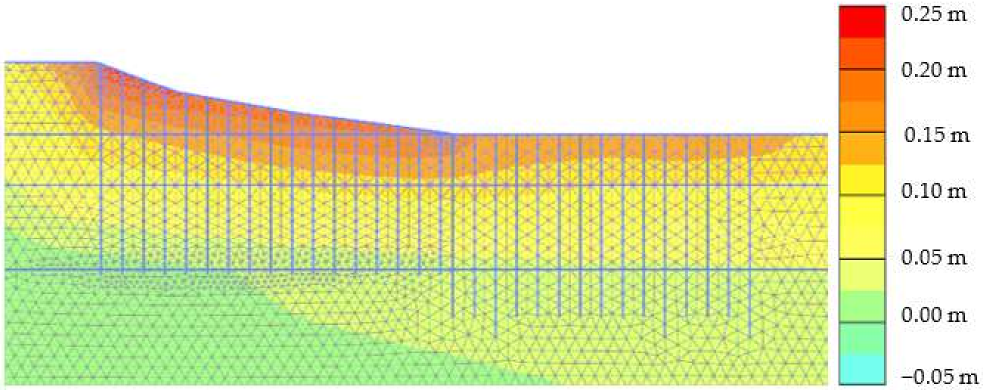

Figure 5.11. FEA of the ME waveform: Residual displacement.

Figures 5.12 and 5.13 illustrate kinematic force distributions determined utilizing the proposed and JRA methods. The JRA equation yields a minimal kinematic force (21 kN) more conservative than the proposed method (6.2 kN). The JRA equation produces the constant kinematic force regardless of distance from the slope's top. In contrast, the proposed method reveals that the kinematic force is less at the base of the slope than at the top because the ground displacement decreases with distance from the top. TE and ME waveforms generate different kinematic forces. Due to its more significant ground displacement, the ME generates a significant kinematic force than the TE (Figure 5.11). The JRA equation does not consider waveform properties; it only considers soil unit weight and depth. Figure 5.13 illustrates the triangular form of the JRA kinematic force distribution, whereas Figure 5.12 illustrates the trapezoidal form of the proposed kinematic force distribution. The JRA equation was derived from the assumption that ground displacement takes place in the soft soil layer. Therefore, the distribution of kinematic forces is calculated at the base of the Clay 2 soil layer. In contrast, the kinematic force distribution in the proposed method is based on the FEA-determined ground displacement. Therefore, when there is no displacement, kinematic force is not computed.

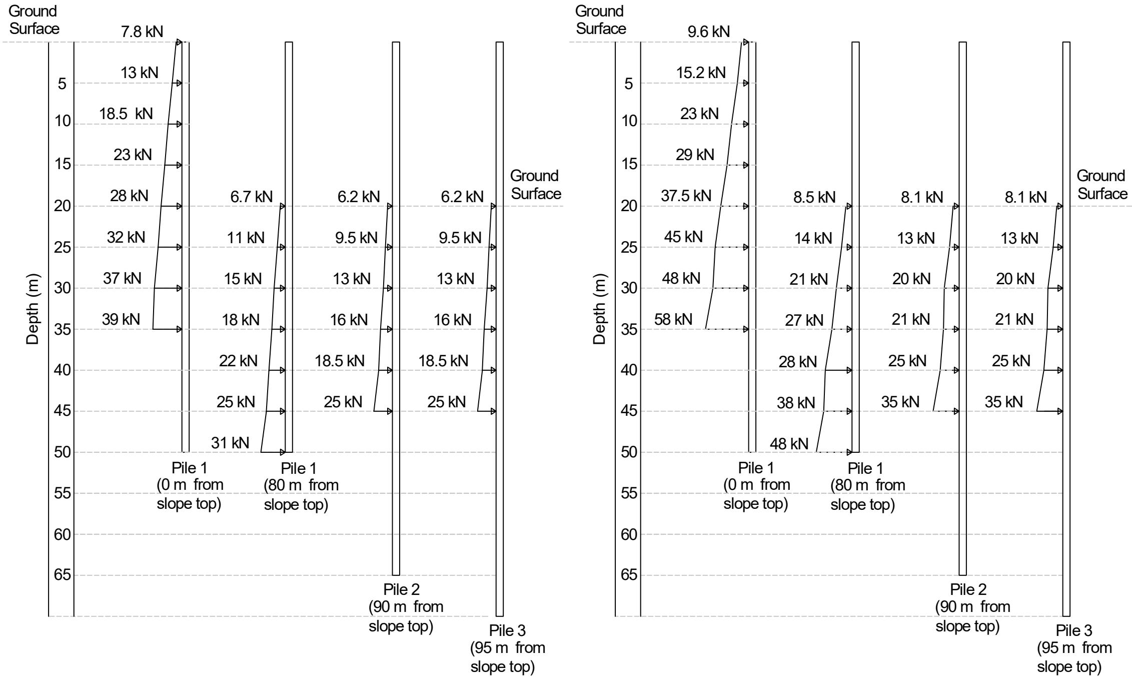

(a) TE (b) ME

Figure 5.12. Examples of kinematic forces using the proposed method.

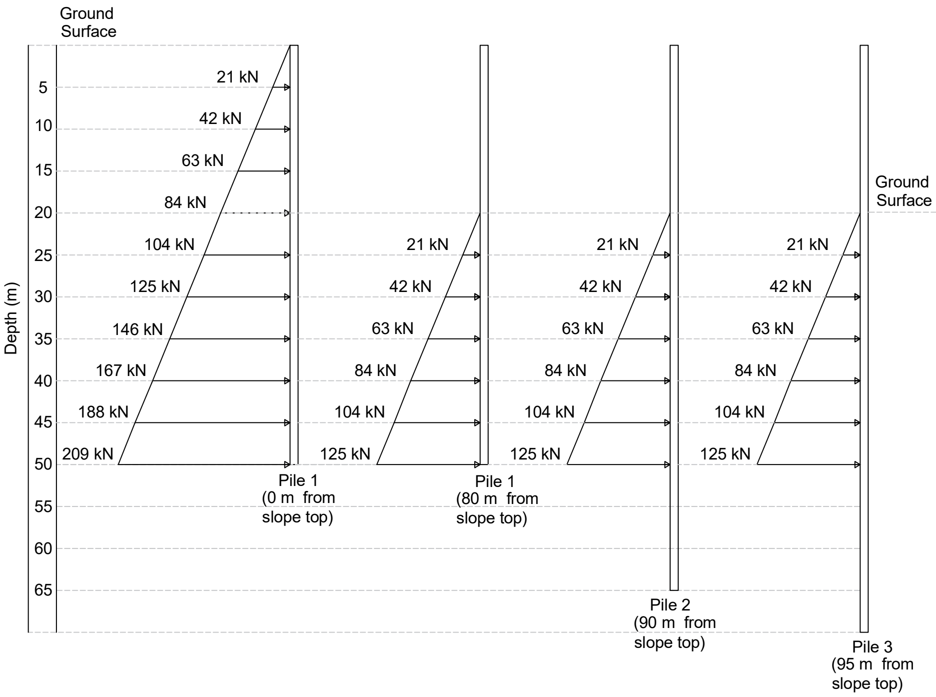

Figure 5.13. Examples of kinematic forces using the JRA method.

5.3.3 Application of the proposed method

Figure 5.14 illustrates the SAs in the upper left corner of the soil model for Scenario 1 for the different damping coefficients derived by the FEA. The TE waveform has a significant SA in periods less than 1.0 s, while the ME waveform has a significant SA in periods greater than 1.0 s.

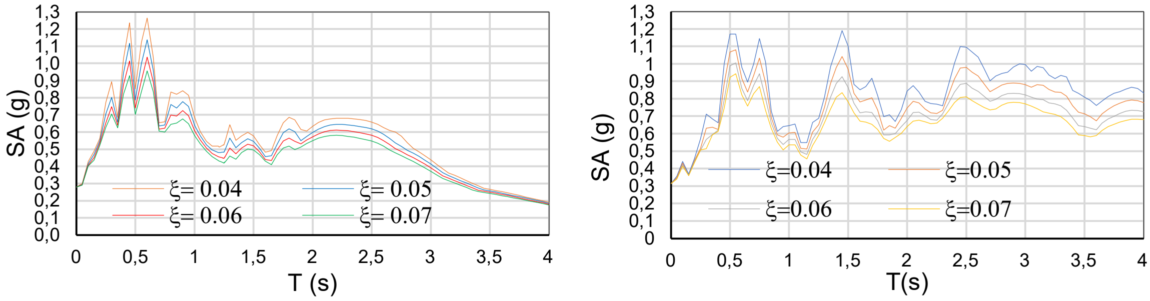

(a) TE waveform (b) ME waveform

Figure 5.14. FEA: Ground surface SAs with various damping coefficients.

Table 5.3 describes the FEA outcome for Scenario 1, applying the TE and ME waveforms. The largest PSW acceleration was derived from the outcome of the FEA. The predominant frequency of the Fourier spectrum determined the natural period of the PSW. The PSW largest acceleration and Fourier spectrum for the PSW deck's upper right (seaward) end were generated. As shown in Figure 5.14, the PSW damping coefficients in Table 5.3 were established so that the maximum FEA accelerations at the deck matched the SAs produced by the FEA ground surface motions. The natural period of the PSW in Scenario 1 was around 1.20 s. Based on the FEA results, the largest acceleration at the deck increased as the PSW became narrower. This is because as the PSW narrows, its structural rigidity decreases, increasing PSW deformation and acceleration. As the width of the PSW decreases, the damping coefficient decreases.

Table 5.3. FEA results for Scenario 1.

Model	TE					ME				
	Width (m)	*Tn* (s)	*fn* (Hz)	*A-FEA* (m/s^2)	ξ	Width (m)	*Tn* (s)	*fn* (Hz)	*A-FEA* (m/s^2)	ξ
1	153	1.242	0.805	3.93	0.07	153	1.227	0.815	5.37	0.07
2	143	1.243	0.805	4.01	0.07	143	1.226	0.816	5.35	0.07
3	133	1.243	0.804	4.10	0.07	133	1.226	0.816	5.40	0.07
4	123	1.244	0.804	4.18	0.07	123	1.227	0.815	5.41	0.07
5	113	1.245	0.803	4.26	0.06	113	1.227	0.815	5.71	0.06
6	103	1.246	0.803	4.34	0.06	103	1.227	0.815	5.72	0.06
7	93	1.248	0.801	4.42	0.06	93	1.229	0.814	5.75	0.06
8	83	1.249	0.801	4.50	0.06	83	1.238	0.808	5.75	0.06
9	70	1.267	0.789	4.45	0.06	70	1.238	0.808	5.80	0.06
10	60	1.252	0.799	4.65	0.05	60	1.226	0.816	6.07	0.05
11	50	1.250	0.800	4.75	0.05	50	1.226	0.816	6.09	0.05
12	40	1.241	0.806	4.91	0.05	40	1.226	0.816	6.10	0.05
13	30	1.227	0.815	5.03	0.04	30	1.226	0.816	6.39	0.04
14	20	1.215	0.823	5.15	0.04	20	1.226	0.816	6.43	0.04

Note: Tn is the natural period of the PSW, fn is the PSW's natural frequency, A-FEA is the deck's maximum acceleration from the FEA, and ξ is the PSW's damping coefficient.

The FA results using the TE and ME waveforms are displayed in Table 5.4. The largest acceleration of the largest deck in Model 14 was 5.38 m/s^2 for the TE waveform and 6.53 m/s^2 for the ME waveform. In contrast, the minimum values for the TE and ME in Model 1 were 3.61 and 5.29 m/s^2, respectively.

Using equations 5.3 and 5.4, the largest acceleration for the PSW was determined based on the FA results for various damping coefficients:

$$\text{A-FA} = \left(\frac{2\pi}{T_d}\right)^2 Dd \qquad \text{(Eq.5.3)}$$

$$T_d = \frac{1}{fn\sqrt{1-\xi^2}} \qquad \text{(Eq.5.4)}$$

where *Dd* is the PSW's displacement, acquired from the FA; *Td* is the damped natural period; ξ is the PSW's damping coefficient; and *fn* is the PSW's natural frequency.

The next step was determining the damping coefficients that best fit the FEA and FA results for the deck's maximum acceleration. The damping coefficients that yield the closest values were chosen as the damping coefficients of the PSW. Table 5.4 outlines the maximum accelerations of the deck from the FA that is most similar to the FEA outcomes.

Table 5.4. FA results for Scenario 1.

Model	TE					ME				
	fn (Hz)	ξ	*Td* (s)	*Dd* (m)	*A-FA* (m/s^2)	*fn* (Hz)	ξ	*Td* (s)	*Dd* (m)	*A-FA* (m/s^2)
1	0.827	0.07	1.21	0.13	3.61	0.827	0.07	1.21	0.20	5.29
2	0.829	0.07	1.21	0.14	3.75	0.829	0.07	1.21	0.20	5.42
3	0.828	0.07	1.21	0.14	3.80	0.828	0.07	1.21	0.20	5.44
4	0.825	0.07	1.22	0.15	3.89	0.825	0.07	1.22	0.20	5.45
5	0.825	0.06	1.21	0.16	4.38	0.825	0.06	1.21	0.22	5.78
6	0.818	0.06	1.23	0.17	4.41	0.818	0.06	1.23	0.22	5.82
7	0.815	0.06	1.23	0.17	4.45	0.815	0.06	1.23	0.22	5.85
8	0.808	0.06	1.24	0.17	4.46	0.808	0.06	1.24	0.23	5.82
9	0.805	0.06	1.24	0.17	4.43	0.805	0.06	1.24	0.23	5.84
10	0.812	0.05	1.23	0.19	4.91	0.812	0.05	1.23	0.24	6.20
11	0.813	0.05	1.23	0.19	4.94	0.813	0.05	1.23	0.24	6.17
12	0.817	0.05	1.23	0.19	4.98	0.817	0.05	1.23	0.23	6.00
13	0.827	0.04	1.21	0.20	5.31	0.827	0.04	1.21	0.24	6.48
14	0.828	0.04	1.21	0.20	5.38	0.828	0.04	1.21	0.24	6.53

Note: *fn* is the natural frequency of the PSW, *ξ* is the PSW's damping coefficient, *Td* is the PSW's damped natural period, *Dd* is the PSW's displacement obtained from the FA, and *A-FA* is the deck's maximum accelerations from the FA.

Comparing the FEA (Table 5.3) and FA (Table 5.4) findings reveals a good agreement. Both analyses indicated that the natural period of the PSW is approximately 1.20 s. Models 1–4, 5–9, 10–12, and 13–14 had damping coefficients of 0.07, 0.06, 0.05, and 0.04, respectively. This result demonstrates that the PSW exhibits consistent damping coefficients regardless of the characteristics of the analyzed waveforms. This is due to the fact that the damping coefficients were predominantly affected by structural properties such as shape, material, and foundation.

Then, a parametric study was performed to discover the variables that influence the PSW damping coefficient. Multiple linear regression was used to conduct a statistical analysis of the PSW's width, mass, natural period, and spring constant as independent variables. A multicollinearity test with the variance inflation factor (VIF) method was performed to prevent highly correlated independent variables in the regression model. The multicollinearity test revealed that the width, mass, and spring constant of the PSW have high VIF values of 1396, 6249, and 10,558, respectively. This outcome is predictable since the model's structural elements increase as the PSW's width increases, causing the mass and spring constant to rise. The strongly correlated variables (i.e., mass and spring constants) were eliminated to minimize multicollinearity problems. Using multilinear regression analysis, the following equation was established to estimate the damping coefficient:

$$\xi = 0.00025w + 0.178Tn - 0.18 \qquad \text{(Eq.5.6)}$$

where w is the PSW's width (m), and Tn is the PSW's natural period (s).

Equation 5.6 has a 94 % determination coefficient (R^2) and a standard error of less than 0.002, indicating that the equation can accurately predict the damping coefficient. The independent variable's probability, or P-value, was less than 0.05, showing that the variable was statistically substantial. This research indicates that the width of the PSW has a substantial effect on the damping coefficient. Incorporating more structural elements (i.e., piles and beams) into the model as the PSW's width increases might result in a greater contribution of material damping to the structural damping, hence raising it. To apply the proposed method to FA Scenario 2, the damping coefficient was calculated using Equation 5.6. Then, using Figures 5.8 and 5.9, the SA was determined using Table 5.1's PSW natural period and Equation 5.6's damping coefficient. Multiplying the obtained SA by the PSW mass from Table 5.1 produced the inertial force. Table 5.5 displays the inertial forces for scenario 2 using the TE and ME waveforms. Because of its greater SA at the PSW's natural period, the ME waveform delivered a greater inertial force than the TE waveform.

Table 5.5. Inertial force for Scenario 2.

Model	ξ	*Fi (kN)*	
		TE	ME
1	0.04	3257	4324
2	0.04	3092	4105
3	0.03	3000	4180
4	0.03	2900	3944
5	0.03	2791	3708
6	0.02	2736	3717
7	0.02	2664	3465
8	0.02	2470	3424
9	0.01	2287	3117
10	0.01	2013	2690
11	0.01	1677	2241
12	0.01	1410	1813
13	0.01	1098	1386
14	0.01	759	958

Note: *Fi* is the inertial force, and ξ is the damping coefficient of the PSW.

Figures 5.15 and 5.16 illustrate the bending moment distributions at scenario 2 caused by the TE and ME waveforms, respectively. The red line denotes the result of the FEA, whereas the black and blue lines denote the findings of the FA using kinematic force calculated by the proposed method (Figure 5.12) and the JRA equation (Figure 5.13), respectively. The FA yields a bending moment consistent with the FEA results using the proposed method. Using the JRA equation, the FA bending moment delivered by the kinematic force yields more conservative results. In Figure 5.15b, for instance, the FEA generated the largest bending moment of 1222 kNm, whereas the FA using the proposed and JRA methods generated 1154 kNm and 1559 kNm, respectively.

Due to the triangular distribution of the kinematic force, the JRA method's bending moment becomes excessive at a depth of 36–40 m. Figures 5.15c, d, and 5.16c,d illustrate the variations in bending moments in piles outside the slope area. The proposed method's bending moment yielded acceptable results compared to the FEA. Figure 5.15c demonstrates that the JRA equation produced a bending moment of 1,723 kNm at a depth of 40 m, whereas the proposed method and FEA yielded bending values of 166 kNm and 115 kNm, respectively. Note that the analyses depicted in Figures 5.15 and 5.16 were analyzed, taking inertial and kinematic forces into account. Consequently, though the kinematic forces of the JRA (Figure 5.13) utilized to generate Figures 5.15 and 5.16 were the same, the outcome was not. This is because the inertial force was computed utilizing distinct ground surface waveforms (Table 5.5).

Figures 5.17 and 5.18 compare the FA bending moment distributions for scenario 2, considering only the inertial force and the FEA results caused by the TE and ME waveforms, respectively. The FA bending moment generated by inertial force is approximately half of the FEA bending moment. This suggests that incorporating kinematic force into the calculation is essential for determining the precise bending moment for a PSW on a mild slope.

The response of piles exposed only to inertial force was similar to the responses generated by the beam on the Winkler foundation or the cantilever when the free length of the pile was considered (Figures 5.17 and 5.18), where the main factors are the cantilever's flexural stiffness and the pile's free length. The bending moment caused by the kinematic force is primarily influenced by the soil/pile stiffness ratio, the impedance contrast of the two soil layers, and the natural frequency of the soil stratum concerning the input waveform. At the border between soil layers, the bending moment under the combined kinematic and inertial loads shows a considerable value (Figures 5.15 and 5.16), indicating that the addition of the kinematic load to the analysis could reveal the effect of the impedance difference concerning the two soil layers.

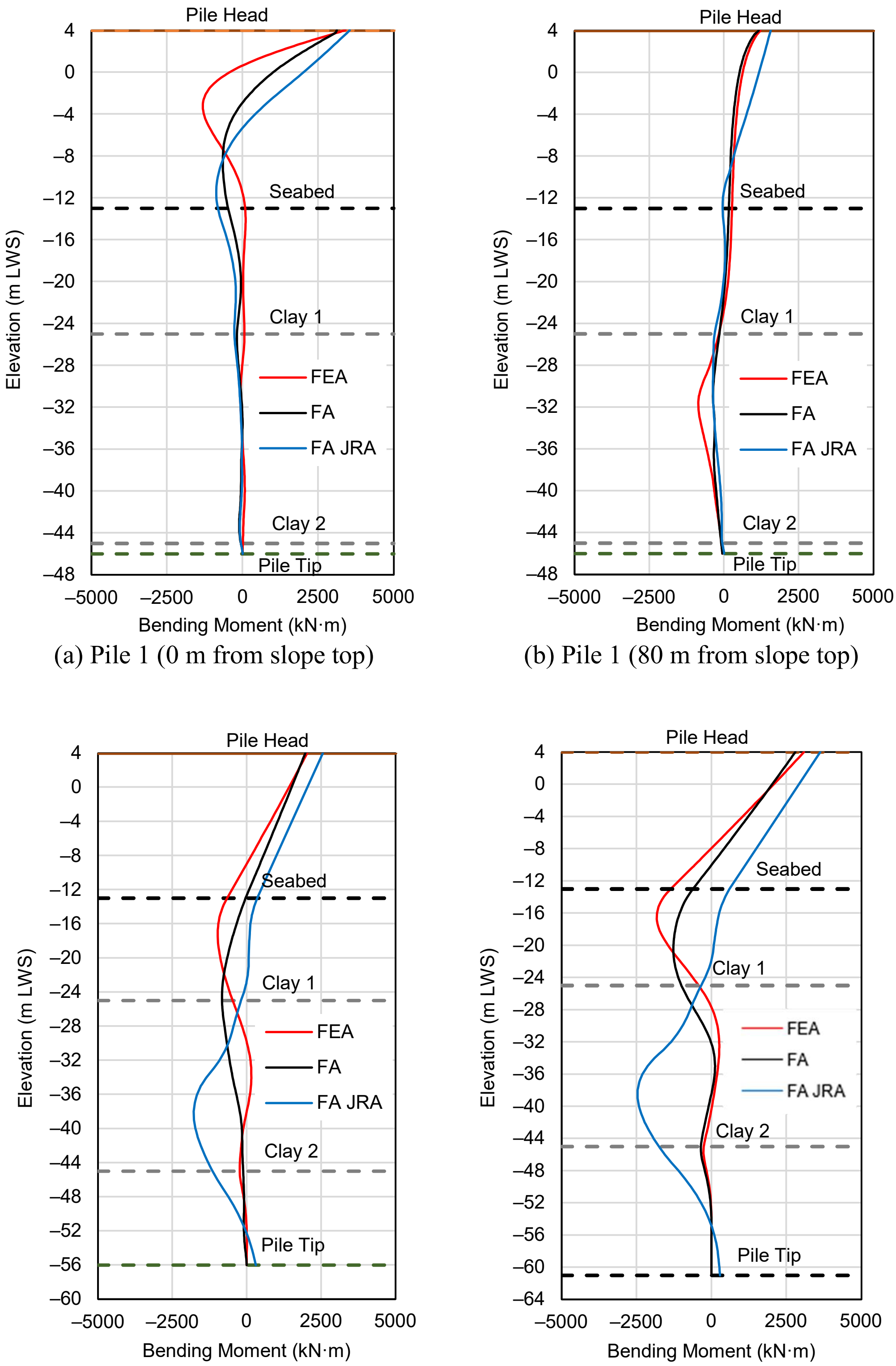

(a) Pile 1 (0 m from slope top)

(b) Pile 1 (80 m from slope top)

(c) Pile 2 (90 m from slope top)

(d) Pile 3 (95 m from slope top)

Figure 5.15. Bending moment distribution of the PSW considering the inertial and kinematic forces due to the TE waveform (Scenario 2).

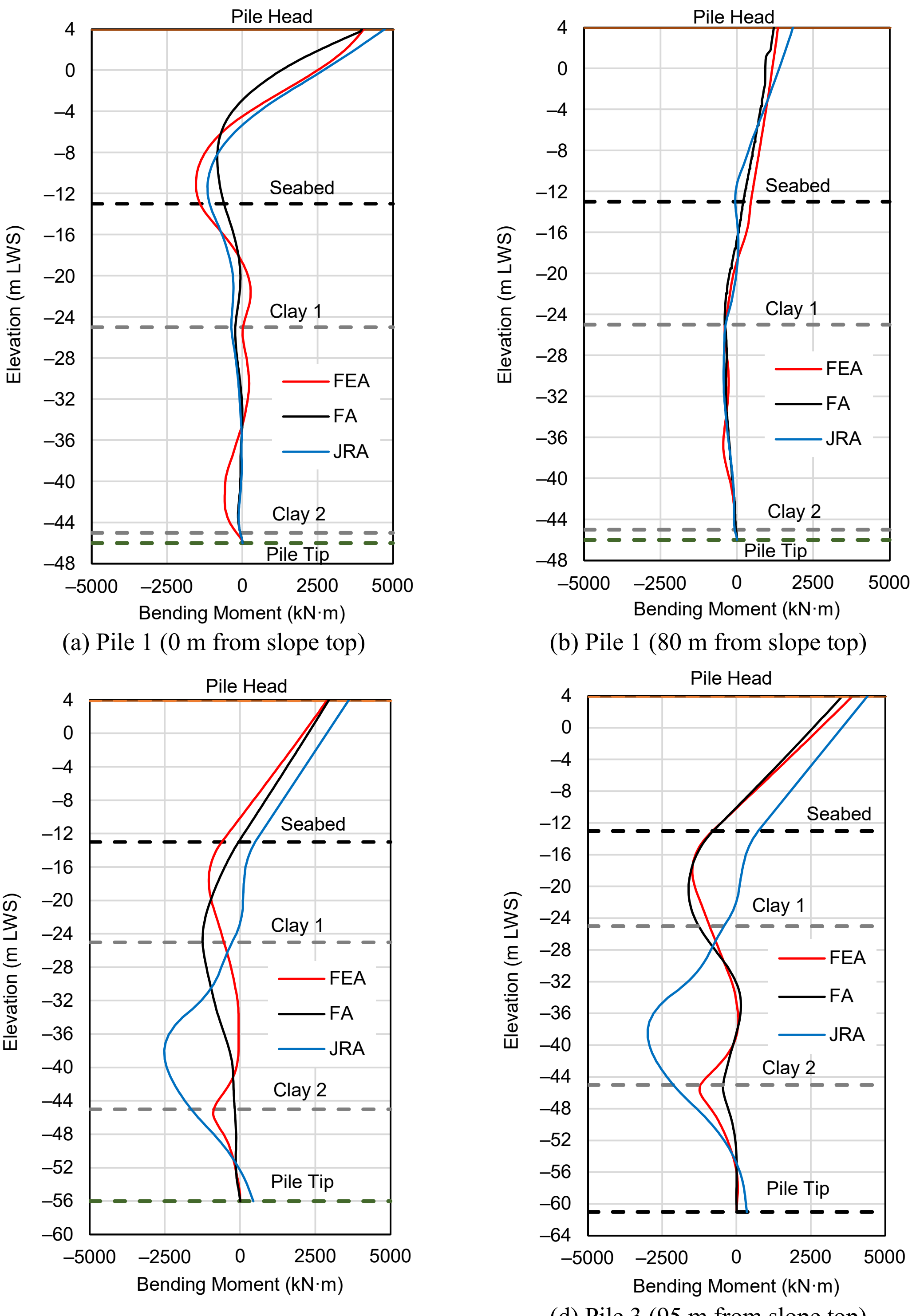

(a) Pile 1 (0 m from slope top)

(b) Pile 1 (80 m from slope top)

(c) Pile 2 (90 m from slope top)

(d) Pile 3 (95 m from slope top)

Figure 5.16. Bending moment distribution of the PSW considering the inertial and kinematic forces due to the ME waveform (Scenario 2).

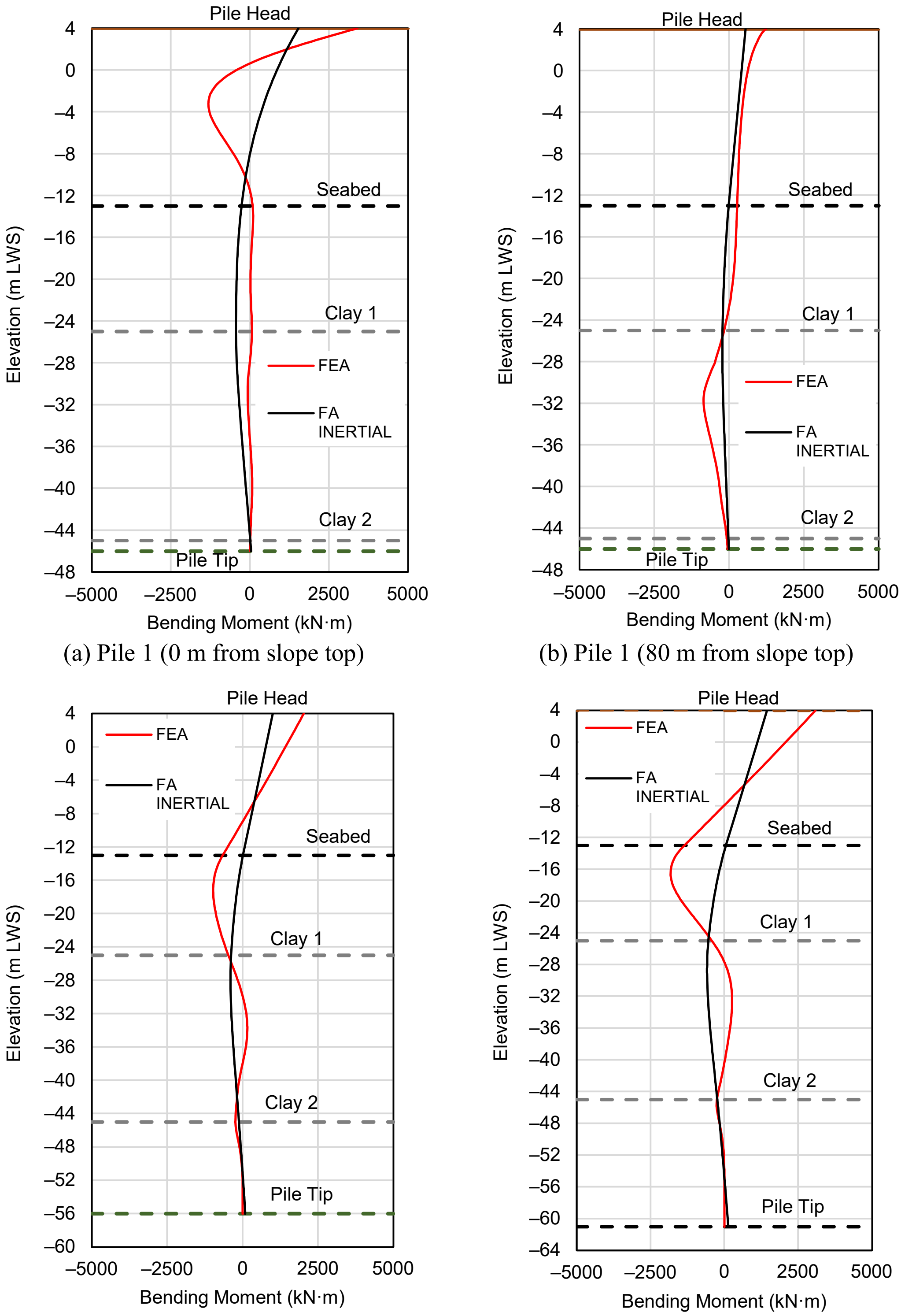

(a) Pile 1 (0 m from slope top) (b) Pile 1 (80 m from slope top)

(c) Pile 2 (90 m from slope top) (d) Pile 3 (95 m from slope top)

Figure 5.17. Bending moment distribution of the PSW considering the inertial forces due to the TE waveform (Scenario 2).

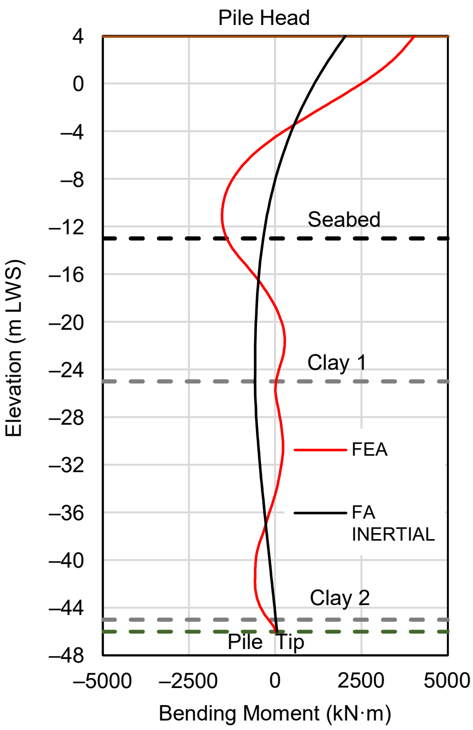

(a) Pile 1 (0 m from slope top)

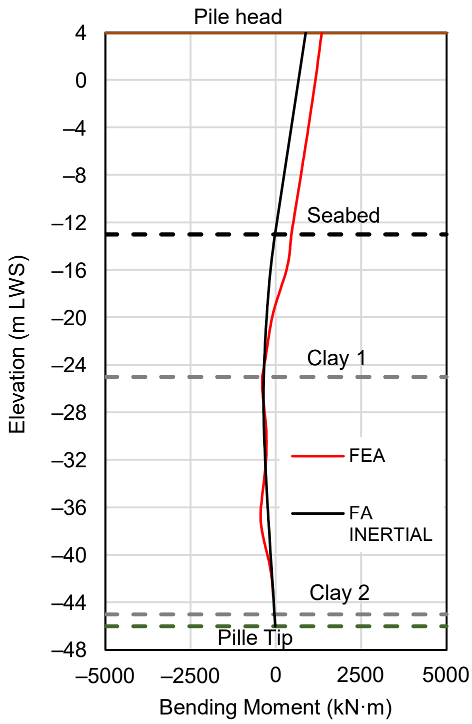

(b) Pile 1 (80 m from slope top)

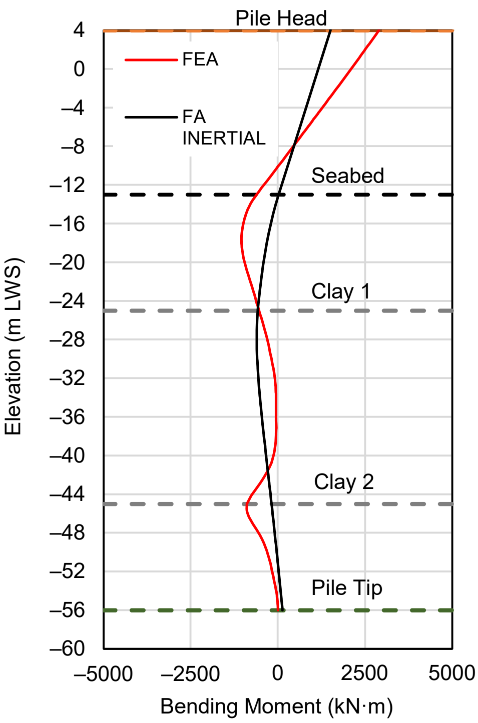

(c) Pile 2 (90 m from slope top)

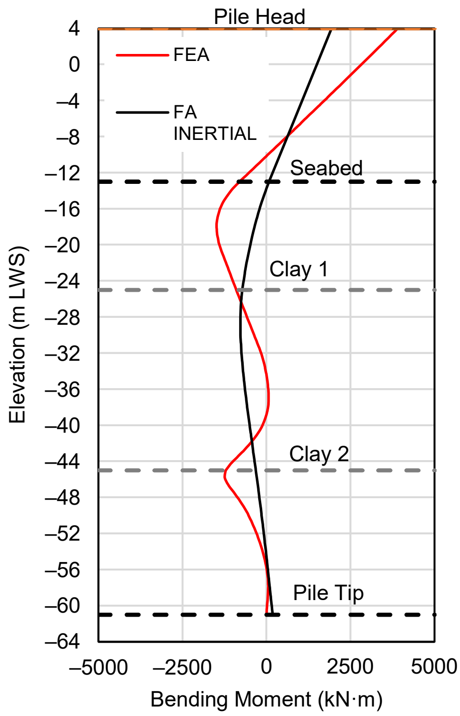

(d) Pile 3 (95 m from slope top)

Figure 5.18. Bending moment distribution of the PSW considering the inertial forces due to the ME waveform (Scenario 2).

CHAPTER 6. APPLICATION OF 2D FRAME ANALYSIS USING 1D ANALYSIS TO DETERMINE KINEMATIC FORCE

6.1 Introduction

The kinematic force on a pile-supported wharf (PSW) pile in the 2D frame analysis could be computed using the ground displacement and the P–Y curve. The corresponding value of the soil reaction *P* obtained from the ground displacement *Y* (as determined by 2D-FEA) could be employed as a kinematic force with satisfactory results. However, this method is ineffective in practice as the FEA analysis must be conducted beforehand to obtain the residual displacement. Therefore, a simple procedure that can predict ground displacement without 2D or 3D analysis is required.

The previous chapter investigated the effect of the combination of inertial and kinematic forces on a PSW pile. The former was calculated based on the maximum acceleration, and the latter was calculated based on the residual ground deformation. The residual bending moment was found by combining values at various times. This chapter combines the inertial and kinematic forces for the same period to replicate the FEA maximum bending moment result.

The validity of this procedure must first be confirmed by comparing the acceleration time history of the deck with the time histories of the bending moments of several pile heads and the ground–surface displacement at several points close to the slope, where the ground displacement is significant. This chapter uses the same target PSW, soil properties, and FEA model as in Chapter 5 (Scenario 2, Model 1). The model utilizes two waveforms with distinct characteristics: the 1968 Tokachi-Oki earthquake (TE) and the 2020 Mentawai earthquake (ME). The ME waveform was altered to fit the target SA from SNI site class SE as used in Chapter 5.

6.2 FEA result

Figures 6.1–6.3 show the time histories of the PSW acceleration, bending moment, and soil displacement, respectively, from the FEA results using the TE and ME waveforms. Figures 6.1a, 6.2a, and 6.3a show the peak acceleration, bending moment, and displacement due to the TE waveform coinciding at 11 s. In contrast, for the ME waveform, these coincide at 40 s (Figures 6.1b, 6.2b, and 6.3b). Figures 6.2 and 6.3 show the bending moment and displacement values at distances 0 m, 5 m, and 10 m from the slope top. As seen in the figures, the values decrease with increasing distance from the slope top. The maximum values of the bending moment and displacement are shown in Table 6.1. The ME waveform generates larger bending moment and displacement values than the TE waveform.

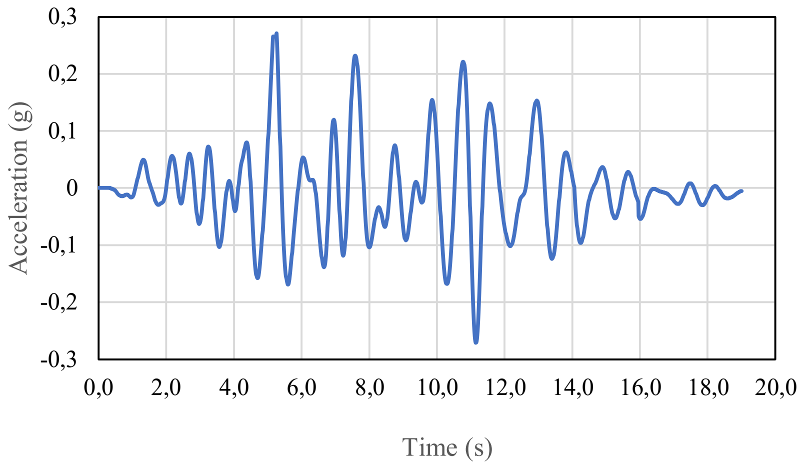

a. TE

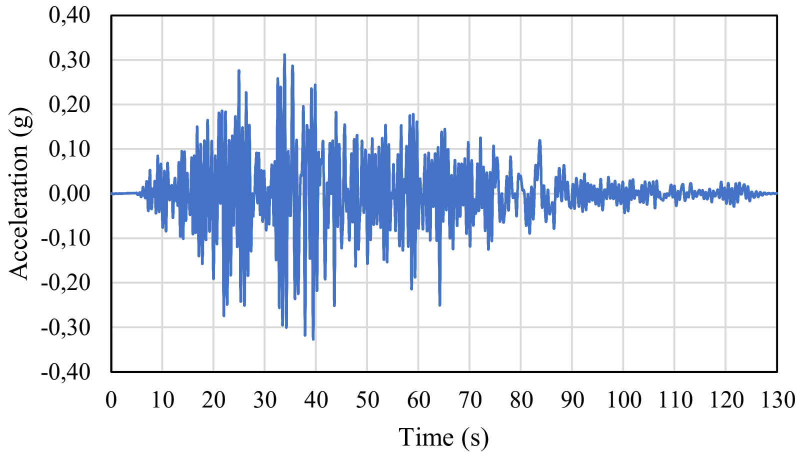

b. ME

Figure 6.1 Acceleration time history of PSW

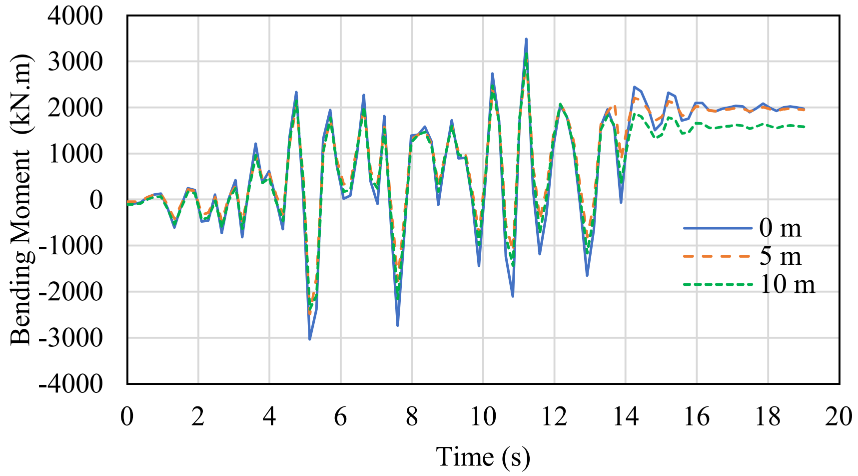

a. TE

Figure 6.2 *Cont.*

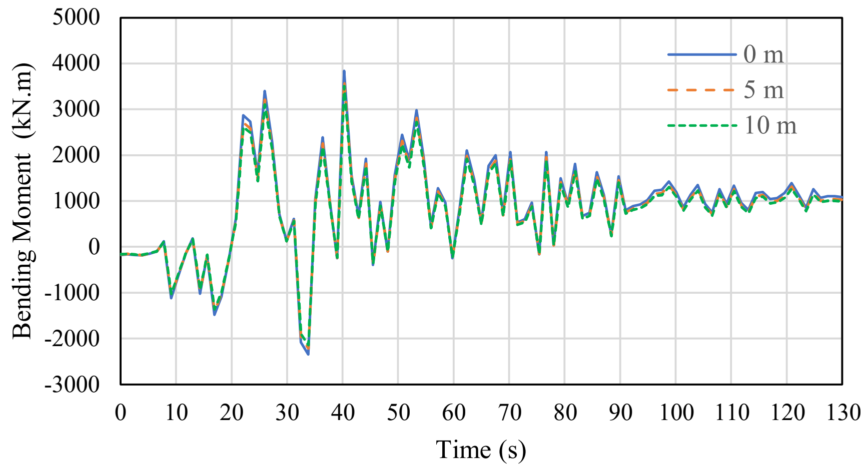

b. ME

Figure 6.2 Bending moment time histories of PSW

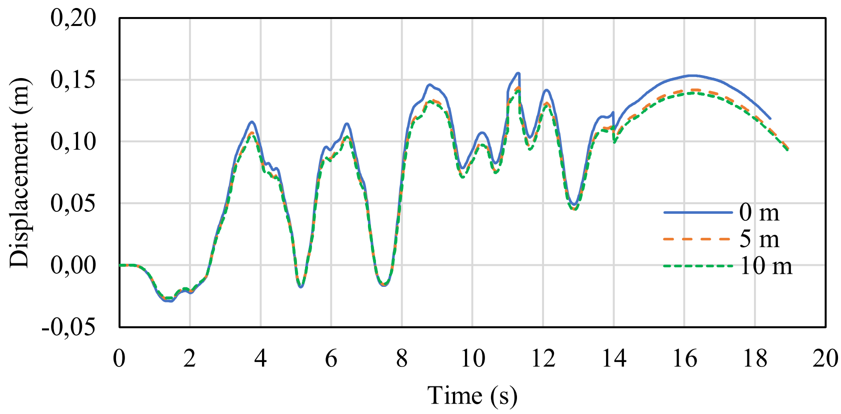

a. TE

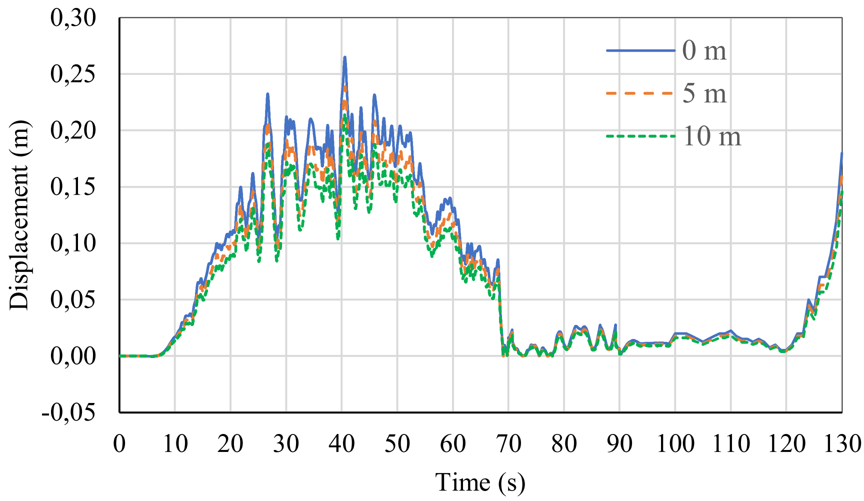

b. ME

Figure 6.3. Maximum soil displacement near pile time histories

Table 6.1 Maximum bending moment and soil displacement

Pile location	Bending moment (kN.m)		Displacement (m)	
	TE	ME	TE	ME
Pile 1 (0 m from slope top)	3493	3881	0.154	0.27
Pile 1 (5 m from slope top)	3292	3629	0.145	0.26
Pile 1 (10 m from slope top)	3171	3508	0.140	0.25

The next step involves applying inertial and kinematic loads to the FA model. The inertial load obtained in Chapter 5 (Scenario 2, Model 1) was 3,257 kN. The displacement distributions used to calculate the kinematic force from the FEA results are shown in Tables 6.2 and 6.3.

Table 6.2 Soil displacement at 11 s using TE

Horizontal Distance from slope top (m)	1	5	10
Depth (m)	Displacement (m)		
1	0.155	0.145	0.14
5	0.15	0.14	0.13
10	0.14	0.13	0.13
15	0.14	0.13	0.12
20	0.13	0.12	0.11
25	0.11	0.11	0.10
30	0.10	0.09	0.08
35	0.09	0.08	0.07

Table 6.3 Soil displacement at 40 s using ME

Horizontal Distance from slope top (m)	1	5	10
Depth (m)	Displacement (m)		
1	0.28	0.26	0.25
5	0.25	0.24	0.23
10	0.20	0.19	0.18
15	0.19	0.18	0.17
20	0.17	0.16	0.15
25	0.15	0.14	0.13
30	0.13	0.12	0.11
35	0.12	0.11	0.1

Tables 6.4 and 6.5 show the kinematic force obtained from the displacement values in Tables 6.2 and 6.3 in conjunction with the P–Y curve shown in Figure 5.5b. The results indicate that the ME waveform produced a larger kinematic force than the TE waveform due to its larger displacement.

Table 6.4 Kinematic Force using TE

Horizontal Distance from slope top (m)	1	5	10
Depth (m)	Kinematic force (kN)		
1	7.8	7.5	7
5	13	12	11
10	18.5	18	17.5
15	23	22	21
20	28	27	26
25	32	31	30
30	37	36	35
35	39	37	36

Table 6.5 Kinematic Force using ME

Horizontal Distance from slope top (m)	1	5	10
Depth (m)	Kinematic force (kN)		
1	9.6	9.4	9.2
5	15.2	14.3	13.2
10	23	22	21
15	29	28	27
20	37.5	36.3	35.2
25	45	44	43
30	48	47	46
35	58	56	55

The pile bending moment was calculated using the inertial force of 3,257 kN and the values of the kinematic force due to soil displacement listed in Tables 6.4 and 6.5. Figures 6.4–6.6 compare the FEA and FA bending moment values, demonstrating that when using the maximum displacement as the base to calculate the inertial force, the FA can produce a maximum bending moment similar to the FEA.

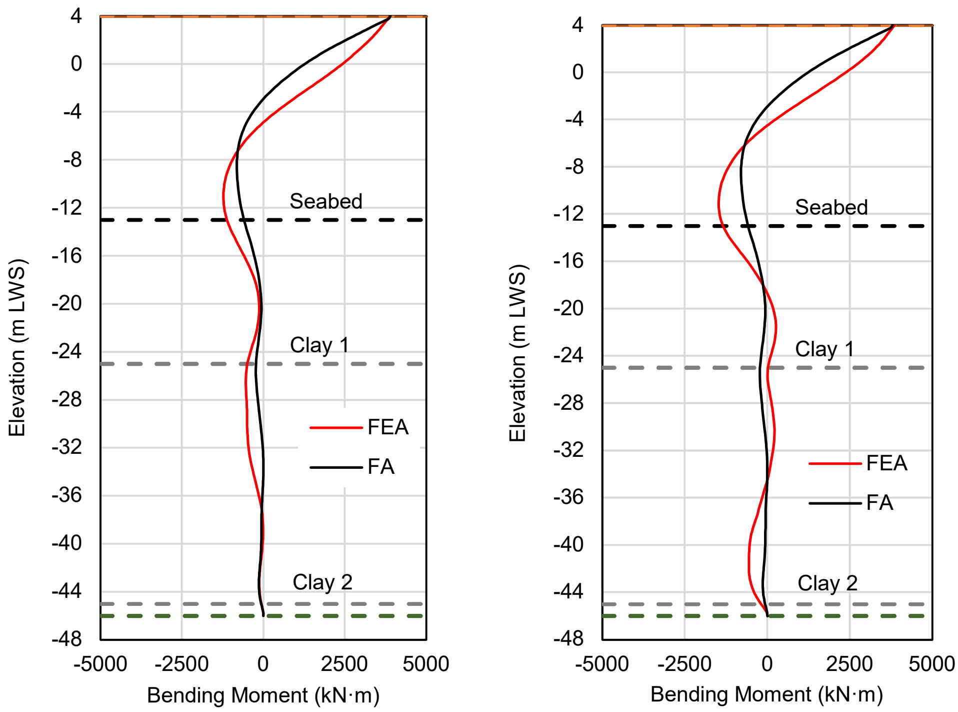

a. TE b. ME

Figure 6.4. Bending Moment of Pile 1 (0 m from slope top)

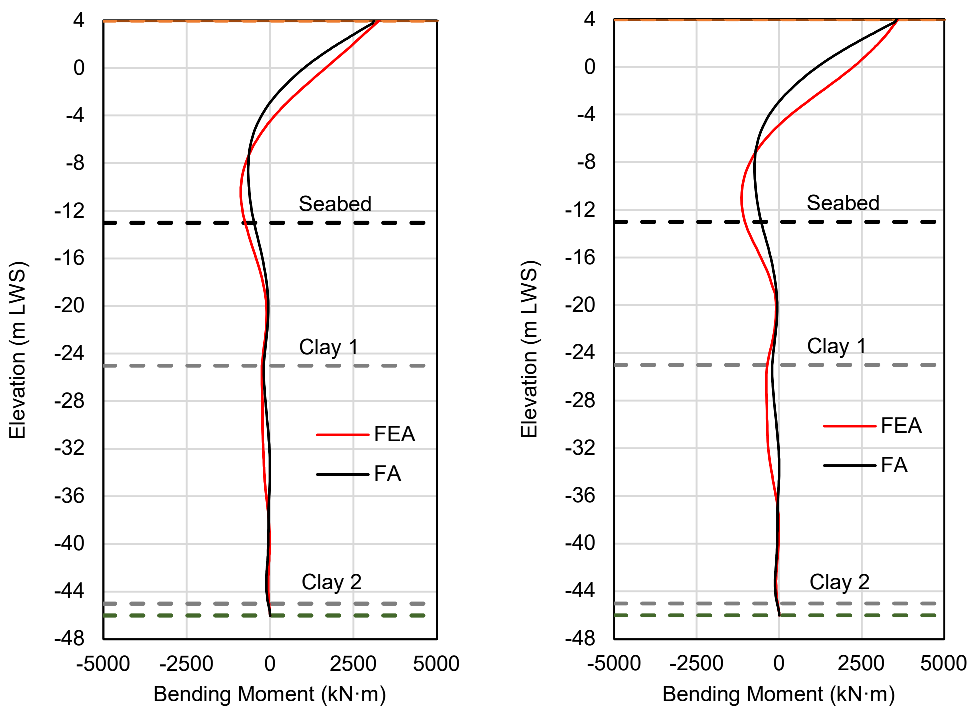

a. TE b. ME

Figure 6.5. Bending Moment of Pile 1 (5 m from slope top)

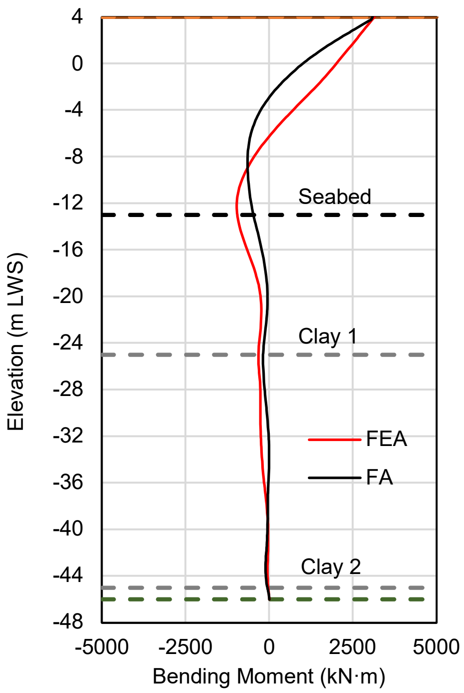

a. TE

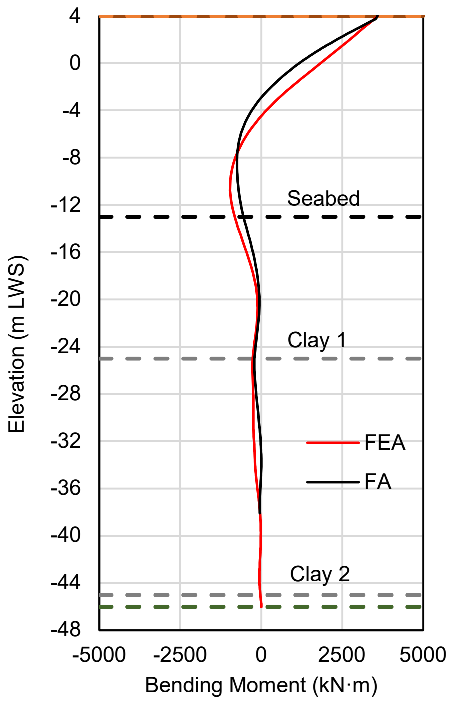

b. ME

Figure 6.6. Bending Moment of Pile 1 (10 m from slope top)

6.3 1D seismic response analysis for estimating maximum soil layer displacement.

Next, a 1D equivalent linear frequency domain analysis was conducted using DEEPSOIL to estimate the maximum soil layer displacement. The 1D seismic response analysis simulations used the TE and ME waveforms as the input motion in the bedrock. The equivalent linear model employs an iterative procedure to select the shear modulus and damping ratio soil properties. These properties can be defined either at discrete points or by specifying the soil parameters that define the backbone curve of one of the non-linear models. For the dependence of the shear modulus and the damping coefficient on the shear strain, the Vucetic and Dobry curves for cohesive soil were used as references. Figure 6.7 displays examples of the backbone curves used in the analysis.

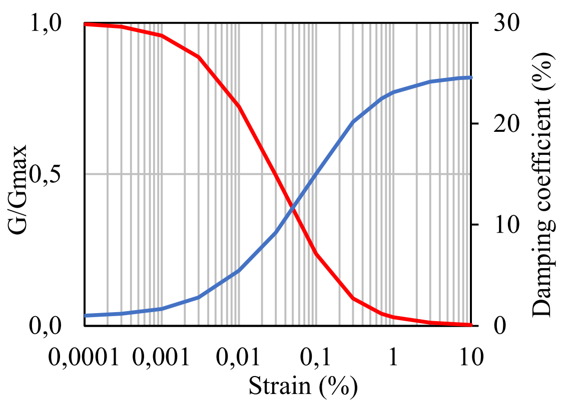

a.Layer 0

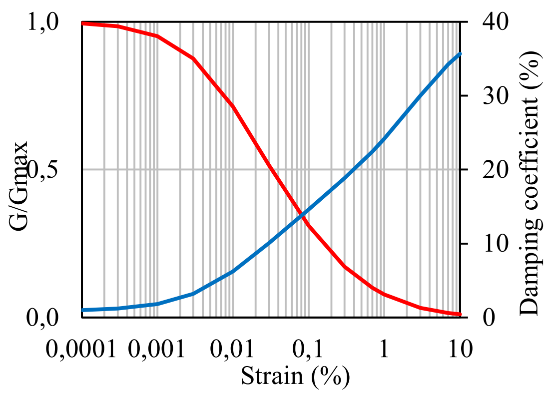

b.Layer 1

Figure 6.7. *Cont.*

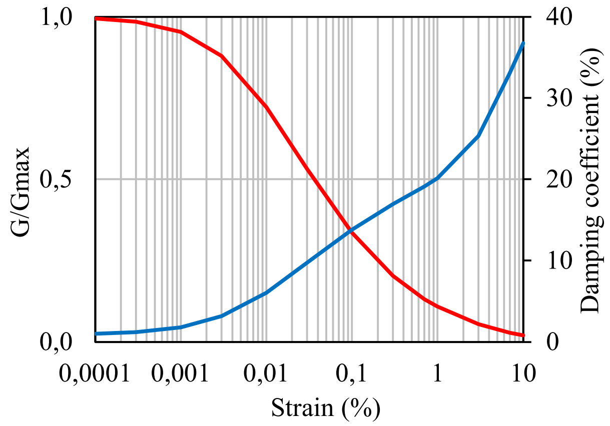

c. Layer 2

Figure 6.7. The backbone curves used in the analysis

Figures 6.8 and 6.9 show the maximum displacement due to the TE and ME waveforms in three soil layers, calculated using equivalent linear frequency domain analysis. In this step, the soil column was modeled at 0, 5, and 10 m from the slope top. The maximum displacement occurred at the surface layer, that is, in the soil model closest to the slope top. The maximum acceleration and displacement coincide at 11 s for the TE waveform and at 40 s for the ME waveform (i.e., similar to the FEA).

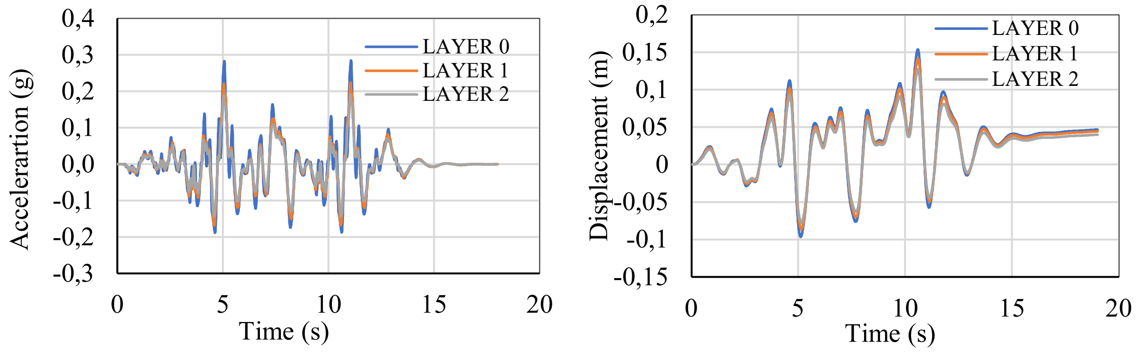

a. Acceleration and displacement time histories at 0 m from the slope top

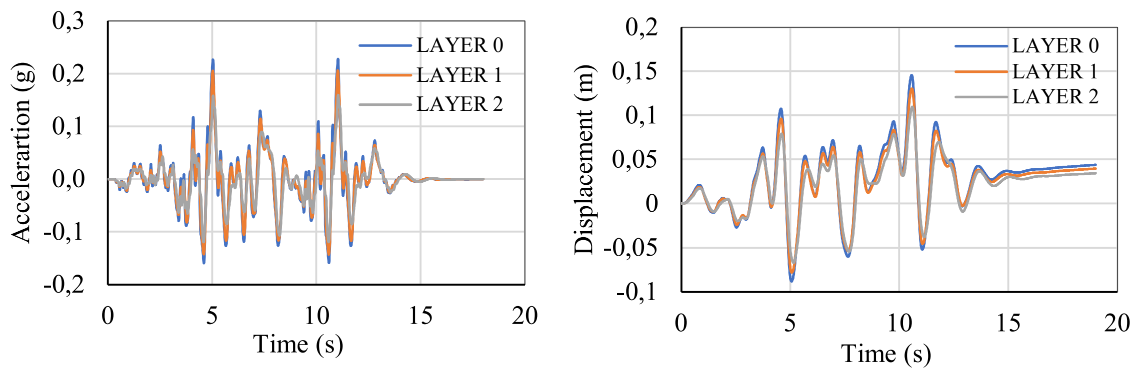

b. Acceleration and displacement time histories at 5 m from the slope top

Figure 6.8. *Cont.*

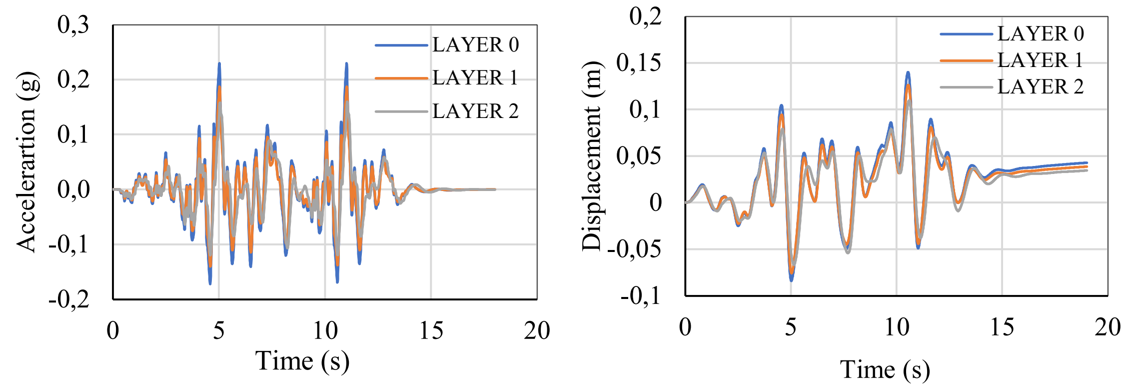

c. Acceleration and displacement time histories at 10 m from the slope top

Figure 6.8 Acceleration and displacement time history due to TE waveform

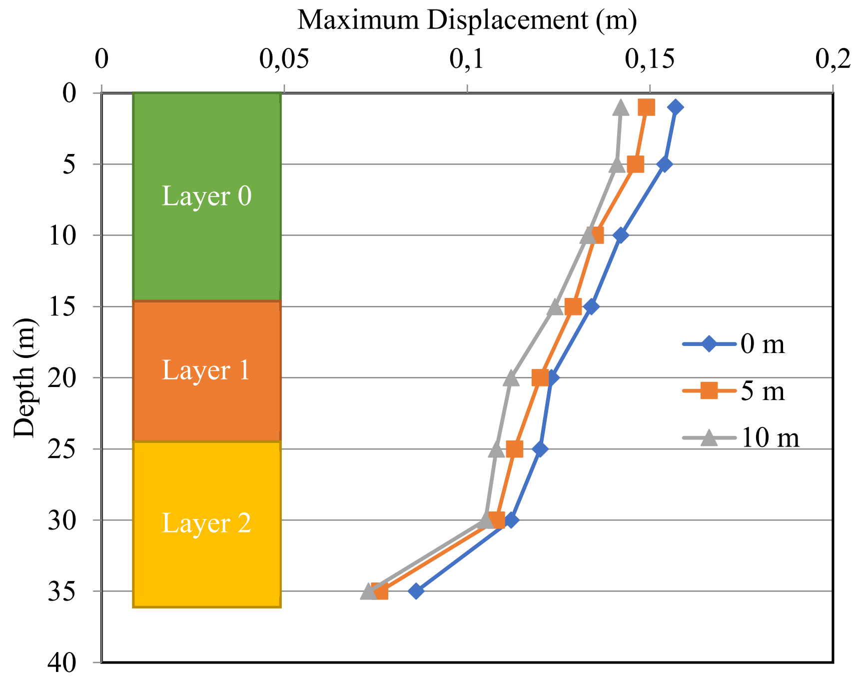

Figure 6.9. Maximum slope displacement due to TE waveform

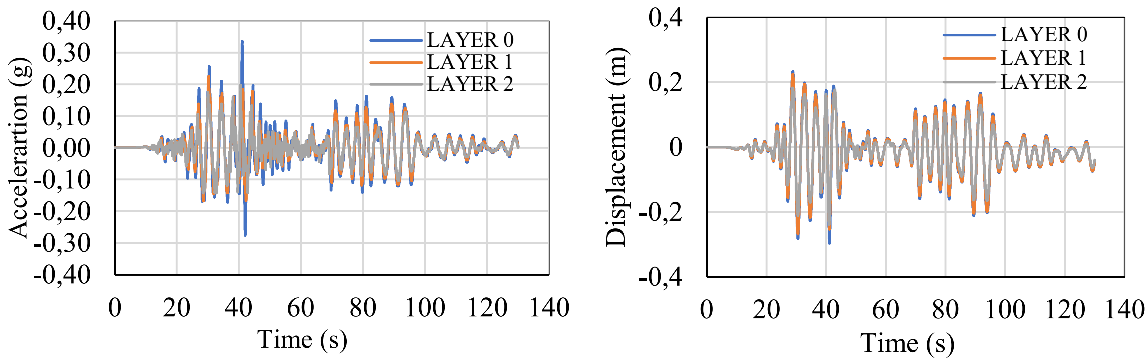

a. Acceleration and displacement time histories at 0 m from the slope top

Figure 6.10. *Cont*

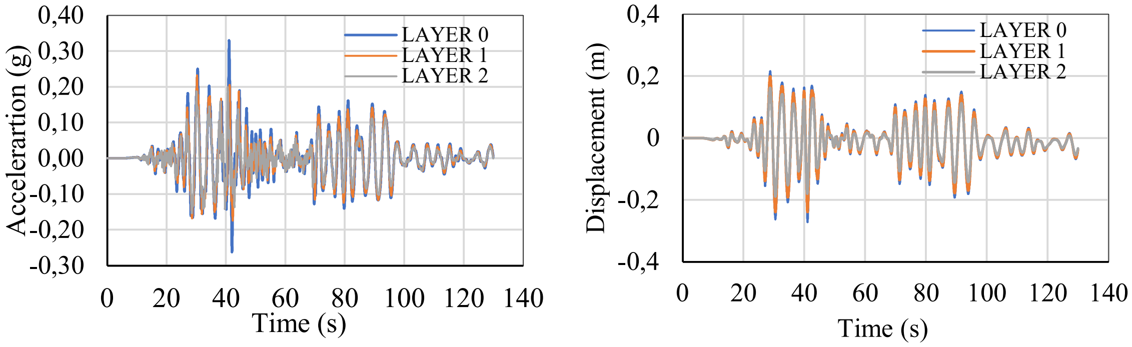

b. Acceleration and displacement time histories at 5 m from the slope top

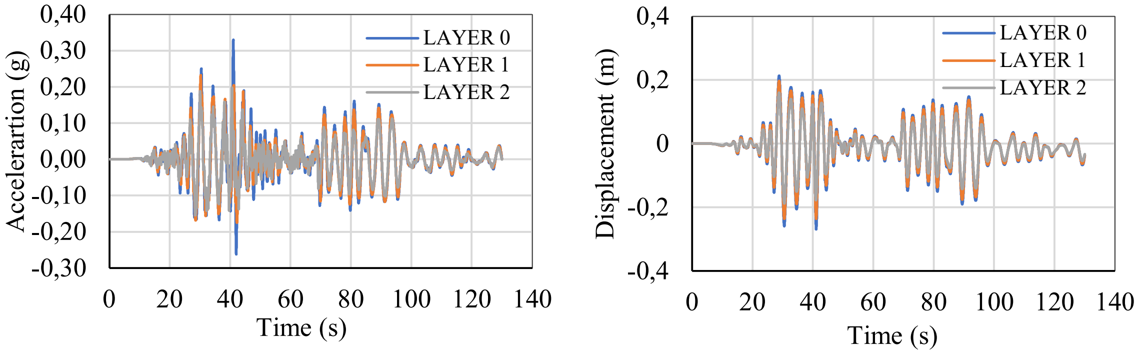

c. Acceleration and displacement time histories at 10 m from the slope top

Figure 6.10 Acceleration and displacement time histories due to ME waveform

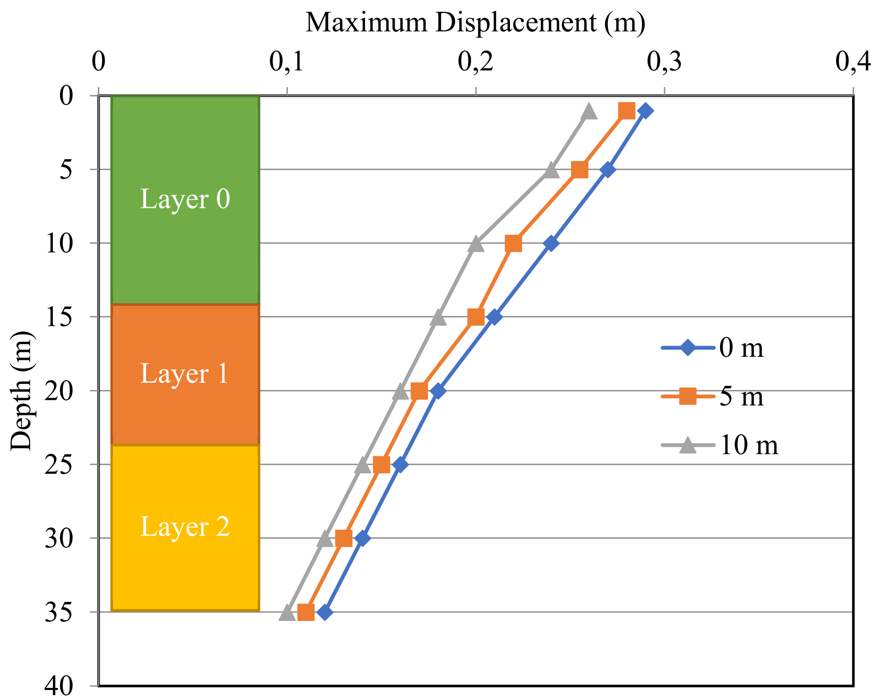

Figure 6.11. Maximum slope displacement due to ME waveform

6.4 Result comparison

The output shows that a 1D seismic response analysis using several soil column models can capture the decrease in soil displacement with increasing distance from the slope top. Comparing the maximum displacement using FEA and 1D seismic response analysis reveals the similarity of the results obtained from the two methods, as shown in Tables 6.6 and 6.7. Since the soil displacements obtained from the FEA and 1D seismic response analysis are similar, the kinematic force values developed from them are also similar. Tables 6.8 and 6.9 show the kinematic force values calculated using the displacements due to the TE and ME waveforms, respectively, from the FEA and 1D seismic response analysis. The results show similarities in the kinematic force values obtained.

Table 6.6. Maximum soil displacement due to TE waveform from FEA and 1D seismic response analysis.

Horizontal Distance from slope top (m)	1		5		10	
Depth (m)	Displacement					
	FEA	1D	FEA	1D	FEA	1D
1	0.155	0,157	0.145	0,149	0.14	0,142
5	0.15	0,154	0.14	0,146	0.13	0,141
10	0.14	0,142	0.13	0,135	0.13	0,133
15	0.14	0,134	0.13	0,129	0.12	0,124
20	0.13	0,123	0.12	0,12	0.11	0,112
25	0.11	0,12	0.11	0,113	0.1	0,108
30	0.1	0,112	0.09	0,108	0.08	0,105
35	0.09	0,086	0.08	0,076	0.07	0,073

Table 6.7. Maximum soil displacement due to ME waveform from FEA and 1D seismic response analysis.

Horizontal Distance from slope top (m)	1		5		10	
Depth (m)	Displacement					
	FEA	1D	FEA	1D	FEA	1D
1	0.28	0,29	0.26	0,28	0.25	0,26
5	0.25	0,27	0.24	0,255	0.23	0,24
10	0.20	0,24	0.19	0,22	0.18	0,2
15	0.19	0,21	0.18	0,2	0.17	0,18
20	0.17	0,18	0.16	0,17	0.15	0,16
25	0.15	0,16	0.14	0,15	0.13	0,14
30	0.13	0,14	0.12	0,13	0.11	0,12
35	0.12	0,12	0.11	0,11	0.1	0,1

Table 6.8. Kinematic force using displacement due to TE waveform from FEA and 1D seismic response analysis.

Horizontal Distance from slope top (m)	1		5		10	
Depth (m)	Kinematic force (kN)					
	FEA	1D	FEA	1D	FEA	1D
1	7.8	8	7.5	7.3	7	7.1
5	13	13.5	12	12.5	11	11.5
10	18.5	19	18	18.5	17.5	18
15	23	22.5	22	21.5	21	21.5
20	28	27	27	26.5	26	26.2
25	32	32.5	31	31.5	30	29.5
30	37	37	36	37	35	36
35	39	38.5	37	36	36	36.5

Table 6.9. Kinematic force using displacement due to ME waveform from FEA and 1D seismic response analysis.

Horizontal Distance from slope top (m)	1		5		10	
Depth (m)	Kinematic force (kN)					
	FEA	1D	FEA	1D	FEA	1D
1	9.6	9.7	9.4	9.6	9.2	9.4
5	15.2	16	14.3	15.3	13.2	14.3
10	23	24	22	23.5	21	23
15	29	31	28	30	27	28
20	37.5	38	36.3	37.5	35.2	36.3
25	45	45.5	44	45	43	44
30	48	49	47	48	46	47
35	58	48	56	56	55	55

Figures 6.12–6.14 compare the bending moments of the FEA (red line), FA using the FEA displacement to calculate kinematic load (black line), and FA using the 1D displacement to calculate kinematic load (blue line). As seen in the figures, when using the maximum displacement, the FA bending moments obtained using 1D equivalent linear analysis and FEA to calculate the kinematic load can produce a maximum bending moment similar to the FEA.

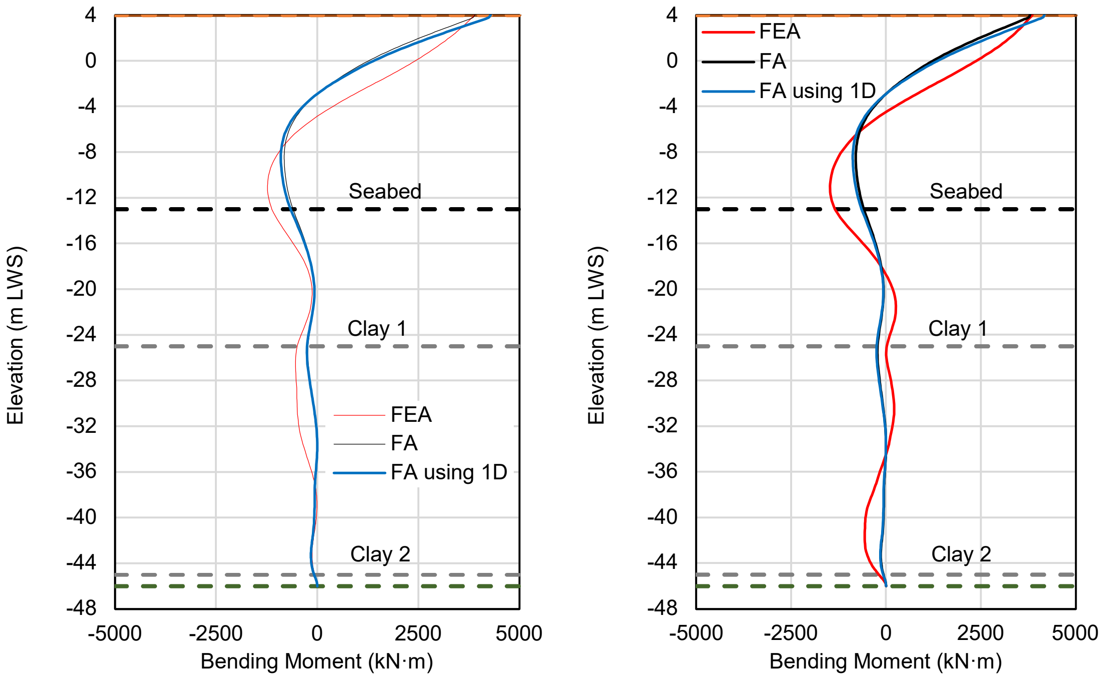

a. TE b. ME

Figure 6.12. Bending Moment of Pile 1 (0 m from slope top)

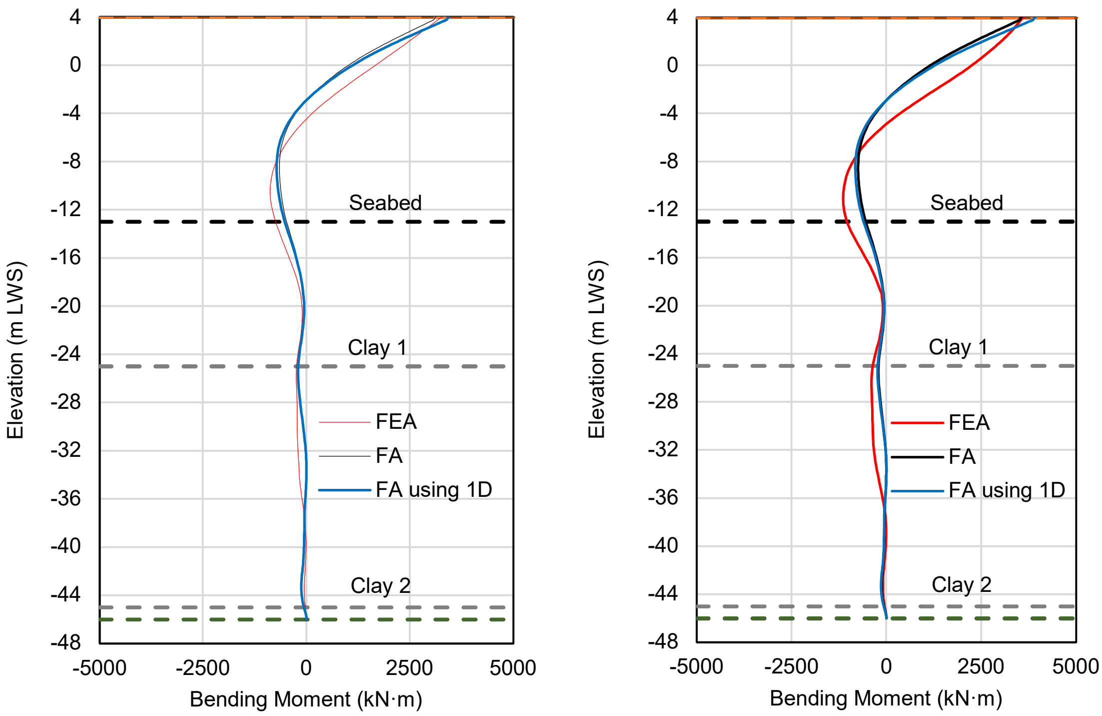

a. TE b. ME

Figure 6.13. Bending Moment of Pile 1 (5 m from slope top)

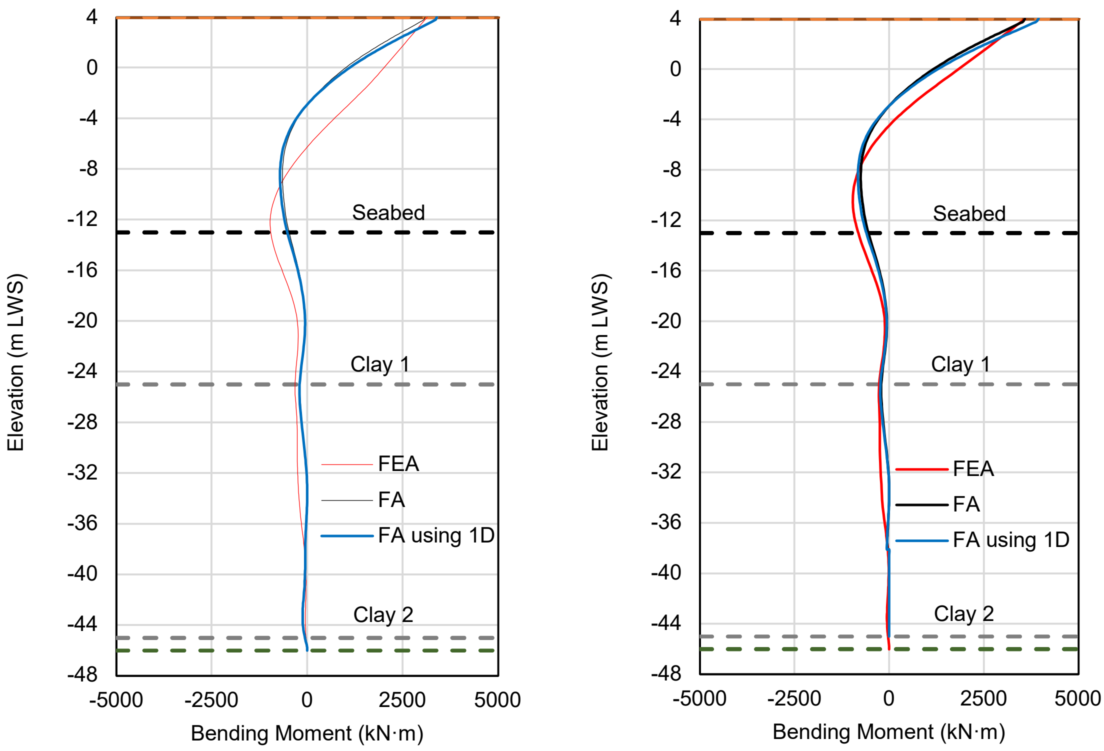

a. TE b. ME

Figure 6.14. Bending Moment of Pile 1 (10 m from slope top)

CHAPTER 7. CONCLUSIONS

This research aims to obtain a novel procedure for assessing the seismic performance of PSW in Indonesia. A new seismic performance assessment for wharves using FA that considers inertial force, kinematic force, and PSW damping coefficient is proposed to achieve this objective. This study proposed a method to calculate kinematic force using soil reaction from the P-Y curve in conjunction with soil displacement. This study also proposed using a 1D site-specific analysis in design practice for estimating the maximum soil displacement required to calculate the kinematic force. Through statistical processing, this study also proposed earthquake ground motions (EGMs) for the seismic design of PSW in Indonesia and compared the recommended EGMs to those in the present design code.

In the first part of the research, site-specific EGMs for the seismic design of port facilities in Indonesia were established by analyzing the seismic response of 144 models using EGM records and Indonesian soil data. The study discovered that the site-specific SAs exhibited a significant difference, particularly in the period range of a PSW. When the predominant frequency of the input EGM in the bedrock matched the natural frequency of the soil layer, the SAs became very large. The site-specific EGMs must be analyzed using a seismic response analysis that considers the location's ground characteristics. In addition, nonlinear soil features must be taken into account.

This research examined the site-specific EGMs for seismic design in conditions where detailed soil properties data at the studied location could not be acquired. The recommended SA targeted the outliers of the analysis's average SAs. In the period range of 0.2–2.0 s for site class SD and 1.0 s or longer for site class SE, the proposed SAs are more significant than those in the SNI. For site class SD, the SNI underrates the amplification factor of the EGMs. Furthermore, the SNI fails to consider the nonlinear characteristics of the soft sediment layers for site class SE. Using the proposed SAs made developing an acceptable seismic design of port facilities for both site classes possible.

The PSW seismic design approach frequently disregards the influence of soil displacement at gentle slopes. In consequence, just the framed structural element was analyzed in the general case. Using a 2D FEA, the seismic performance of a large PSW considering soil-structure dynamic interaction was analyzed. The study determined that the 2D soil-structure FEA was a good tool for evaluating PSW's seismic performance and is successful at accounting for the influence of soil displacement and waveform durations. Seismic codes typically specify only SA as seismic load; however, multiple time history waveforms are possible for the same SA. Different waveforms caused the pile's largest PSW displacement and bending moment to vary significantly. When conducting seismic design, it is necessary to consider various time-history waveforms and pay close consideration to the phase characteristics.

Different FEA modeling scenarios (i.e., with or without soil slope consideration) produced various pile bending moments and PSW residual displacements. Even when the slope of the soil beneath the PSW is moderate, the influence of the soil slope displacement is substantial. Therefore, special consideration should be given to soil displacement in the design procedure. Different FEA modeling scenarios also resulted in distinct PSW vibration characteristics. When soil slope is considered, the PSW's natural period decreases as the pile's free length in the soil slope decreases. Consequently, it is crucial to determine the appropriate natural period of the PSW. When soil slope is considered, a comparatively large bending moment appears at the interface among soil layers. Therefore, consideration must be given to the relatively large bending moment produced at the interface of soil layers with a large impedance difference.

In order to examine the seismic performance of a wide PSW with a mild soil slope, our study proposes an FA approach that takes into account both inertial and kinematic forces considering the PSW damping coefficient. The FA provides a quick and dependable analysis procedure for evaluating the seismic performance of PSWs, and it can account for the impact of kinematic forces. Additionally, it can generate bending moments similar to those generated by FEA.

The standard damping coefficient used in seismic PSW design is 0.05. According to this study, a wide PSW has a larger damping coefficient than a regular PSW with a narrower width. This research provided a formula for determining the PSW damping coefficient using its width and natural periods. A combination of inertial and kinematic forces generates a PSW pile's bending moment. The bending moment generated by inertial force is only about fifty percent of the FEA bending moment. Combining the kinematic force with the calculation could establish the effect of soil displacement and the difference in stiffness among the two soil layers, yielding a similar outcome to the FEA. The bending moment may be underestimated if inertial forces were the only force considered for PSWs on a slope. Kinematic force still has a substantial effect even in a PSW on a gentle slope.

Seismic performance assessments using only the inertial force, or the kinematic force (JRA method) are inappropriate, whereas seismic evaluations employing the recommended method are highly applicable. The piles' bending moment distribution revealed that the JRA method was incapable of estimating the kinematic force. At a certain depth, the bending moment became excessively large due to the triangular distribution of the kinematic force. Therefore, research must develop a justification factor for the JRA equation that considers soil-structure geometric parameters and hazard characteristics to improve its precision.

The kinematic force in the FA can be calculated using soil displacement and soil spring characteristics. The soil reaction value can be applied as a kinematic force in conjunction with the ground displacement (as determined by FEA). This research also shows that using maximum displacement, the FA bending moments using 1D site specific using equivalent linear analysis for calculating kinematic load could produce a maximum bending moment similar to the FEA's.

REFERENCE

1. Kayen, R.E.; Mitchell, J.K.; Seed, R.B.; Nishio, S. Soil Liquefaction in the East Bay during the Earthquake. *US Geological Survey Professional Paper* 1998.
2. Werner, S.; McCullough, N.; Bruin, W.; Augustine, A.; Rix, G.; Crowder, B.; Tomblin, J. Seismic Performance of Port de Port-Au-Prince during the Haiti Earthquake and Post-Earthquake Restoration of Cargo Throughput. *Earthquake Spectra* 2011, *27*, 387–410, doi:10.1193/1.3638716.
3. Chang, S.E. Disasters and Transport Systems: Loss, Recovery and Competition at the Port of Kobe after the 1995 Earthquake. *J Transp Geogr* 2000, *8*, 53–65, doi:10.1016/S0966-6923(99)00023-X.
4. Erdik, M.; Uckan, E. Earthquake Damage and Fragilities of Industrial Facilities. In Proceedings of the Seismic Design of Industrial Facilities; Springer Fachmedien Wiesbaden: Wiesbaden, 2014; pp. 3–13.
5. Mavroulis, S.; Triantafyllou, I.; Karavias, A.; Gogou, M.; Katsetsiadou, K.N.; Lekkas, E.; Papadopoulos, G.A.; Parcharidis, I. Primary and Secondary Environmental Effects Triggered by the 30 October 2020, Mw = 7.0, Samos (Eastern Aegean Sea, Greece) Earthquake Based on Post-Event Field Surveys and Insar Analysis. *Applied Sciences (Switzerland)* 2021, *11*, doi:10.3390/app11073281.
6. Natawidjaja, D.H. Neotectonics of the Sumatran Fault And Paleogeodesy of the Sumatran Subduction Zone, California Institute of Technology: Pasadena, California, 2002.
7. Ghobarah, A.; Saatcioglu, M.; Nistor, I. The Impact of the 26 December 2004 Earthquake and Tsunami on Structures and Infrastructure. *Eng Struct* 2006, *28*, 312–326, doi:10.1016/j.engstruct.2005.09.028.
8. Lorito, S.; Romano, F.; Piatanesi, A.; Boschi, E. Source Process of the September 12, 2007, M W 8.4 Southern Sumatra Earthquake from Tsunami Tide Gauge Record Inversion. *Geophys Res Lett* 2008, *35*, L02310, doi:10.1029/2007GL032661.
9. Wilkinson, S.M.; Alarcon, J.E.; Mulyani, R.; Whittle, J.; Chian, S.C. Observations of Damage to Buildings from M w 7.6 Padang Earthquake of 30 September 2009. *Natural Hazards* 2012, *63*, 521–547, doi:10.1007/s11069-012-0164-y.
10. Newman, A. V.; Hayes, G.; Wei, Y.; Convers, J. The 25 October 2010 Mentawai Tsunami Earthquake, from Real-Time Discriminants, Finite-Fault Rupture, and Tsunami Excitation. *Geophys Res Lett* 2011, *38*, n/a-n/a, doi:10.1029/2010GL046498.
11. Ko, Y.Y.; Lin, Y.Y. A Comparison of Simplified Modelling Approaches for Performance Assessment of Piles Subjected to Lateral Spreading of Liquefied Ground. *Geofluids* 2020, *2020*, doi:10.1155/2020/8812564.
12. Li, X.; Tang, L.; Man, X.; Qiu, M.; Ling, X.; Cong, S.; Elgamal, A. Liquefaction-Induced Lateral Load on Pile Group of Wharf System in a Sloping Stratum: A Centrifuge Shake-Table Investigation. *Ocean Engineering* 2021, *242*, 110119, doi:10.1016/j.oceaneng.2021.110119.
13. Mondal, G.; Rai, D.C. Performance of Harbour Structures in Andaman Islands during 2004 Sumatra Earthquake. *Eng Struct* 2008, *30*, 174–182, doi:10.1016/j.engstruct.2007.03.015.
14. Johnson, G. *ASCE 61-14: A NEW SEISMIC DESIGN STANDARD FOR PIERS AND WHARVES*; 2014;

15. Su, L.; Lu, J.; Elgamal, A.; Arulmoli, A.K. Seismic Performance of a Pile-Supported Wharf: Three-Dimensional Finite Element Simulation. *Soil Dynamics and Earthquake Engineering* 2017, *95*, 167–179, doi:10.1016/j.soildyn.2017.01.009.
16. Heidary-Torkamani, H.; Bargi, K.; Amirabadi, R.; McCllough, N.J. Fragility Estimation and Sensitivity Analysis of an Idealized Pile-Supported Wharf with Batter Piles. *Soil Dynamics and Earthquake Engineering* 2014, *61–62*, 92–106, doi:10.1016/j.soildyn.2014.01.024.
17. Hamrouni, A.; Deghoul, L.; Gabi, S. The Influence of the Soil Constitutive Models on the Seismic Analysis of Pile-Supported Wharf Structures with Batter Piles in Cut-Slope Rock Dike. *Studia Geotechnica et Mechanica* 2020, *42*, 191–209, doi:10.2478/sgem-2019-0050.
18. Nagao, T.; Lu, P. A Simplified Reliability Estimation Method for Pile-Supported Wharf on the Residual Displacement by Earthquake. *Soil Dynamics and Earthquake Engineering* 2020, *129*, 105904, doi:10.1016/j.soildyn.2019.105904.
19. Gao, S.; Gong, J.; Feng, Y. Equivalent Damping Ratio Equations in Support of Displacement-Based Seismic Design for Pile-Supported Wharves. *Journal of Earthquake Engineering* 2017, *21*, 493–530, doi:10.1080/13632469.2016.1172377.
20. Boroschek, R.L.; Baesler, H.; Vega, C. Experimental Evaluation of the Dynamic Properties of a Wharf Structure. *Eng Struct* 2011, *33*, 344–356, doi:10.1016/j.engstruct.2010.10.014.
21. Chen, Y.; Sun, H.; Feng, Z.; Chen, Y.; Sun, H.; Feng, Z. Study on Seismic Isolation of Long Span Double Deck Steel Truss Continuous Girder Bridge. 2022, doi:10.3390/app12052567.
22. Stehmeyer, Edward.H. Seismic Vulnerability Assessments of Marine Structures Using Non-Linear Static Analysis Procedures. *Structures Congress 2011* 2011, 2297–2308, doi:https://doi.org/10.1061/9780784411711.
23. Widyastuti, H.; Lumantarna, E.; Sofi, M.; Ramli, M.I.; Oktavianus, Y.; Rajabifard, A. Earthquake Vulnerability of Port Structures in Indonesia. *IOP Conf Ser Earth Environ Sci* 2020, *419*, doi:10.1088/1755-1315/419/1/012001.
24. Dobry, R.; Abdoun, T.; O'Rourke, T.D.; Goh, S.H. Single Piles in Lateral Spreads: Field Bending Moment Evaluation. *Journal of Geotechnical and Geoenvironmental Engineering* 2003, *129*, 879–889, doi:10.1061/(asce)1090-0241(2003)129:10(879).
25. Tang, L.; Ling, X.; Zhang, X.; Su, L.; Liu, C.; Li, H. Response of a RC Pile behind Quay Wall to Liquefaction-Induced Lateral Spreading: A Shake-Table Investigation. *Soil Dynamics and Earthquake Engineering* 2015, *76*, 69–79, doi:10.1016/j.soildyn.2014.12.015.
26. Haigh, S.K.; Madabhushi, S.P.G. Centrifuge Modelling of Lateral Spreading Past Pile Foundations. In Proceedings of the International Conference on Physical Modelling in Geotechnics. 2002.; 2022.
27. Boyke, C.; Nagao, T. Seismic Performance Assessment of Wide Pile-Supported Wharf Considering Soil Slope and Waveform Duration. *Applied Sciences (Switzerland)* 2022, *12*, doi:10.3390/app12147266.
28. ATC ATC 40 Seismic Evaluation and Retrofit of Concrete Buildings. *Seismic safety commisionsion* 1996, *1*, 334.
29. ASCE FEMA 356-PRESTANDARD AND COMMENTARY FOR THE SEISMIC REHABILITATION OF BUILDINGS. *Federal Emergency Management Agency* 2000, *FEMA 356*, 519.

30. ASCE/CORPRI *ASCE 61-14. Seismic Design of Piers and Wharves Seismic Design of Piers and Wharves*; American Society of Civil Engineers: Reston,Virginia, 2014; ISBN 9780784413487.
31. Shibata, A.; Sozen, M.A. Substitute-Structure Method for Seismic Design in R/C. *Journal of the Structural Division* 1976, *102*, 1–18, doi:10.1061/JSDEAG.0004250.
32. Zacchei, E.; Lyra, P.H.C.; Stucchi, F.R. Nonlinear Static Analysis of a Pile-Supported Wharf. *IBRACON STRUCTURES AND MATERIALS JOURNAL* 2019, *12*, 998–1009.
33. Shafieezadeh, A.; Desroches, R.; Werner, S.D.; Rix, G.J. Seimic Response of Pile-Supported Container Wharves. In Proceedings of the TCLEE 2009: Lifeline Earthquake Engineering in a Multihazard Environment; 2009; pp. 878–887.
34. Vamvatsikos, D.; Cornell, C.A. The Incremental Dynamic Analysis and Its Application To Performance-Based Earthquake Engineering. *European Conference on Earthquake Engineering* 2002, 10.
35. FEMA *FEMA-351,Recommended Seismic Evaluation and Upgrade Criteria for Existing Welded Steel Moment-Frame Buildings*; Venture, S.J., Ed.; Federal Emergency Management Agency: Washington D.C, 2020;
36. Sobhan, M.S.; Rofooei, F.R.; Attari, N.K.A. Buckling Behavior of the Anchored Steel Tanks under Horizontal and Vertical Ground Motions Using Static Pushover and Incremental Dynamic Analyses. *Thin-Walled Structures* 2017, *112*, 173–183, doi:10.1016/j.tws.2016.12.022.
37. Soltani, M.; Amirabadi, R. Sensitivity Analysis of Pile Supported Wharves against Directional Uncertainty of Earthquakes Using Fragility Curves. *INTERNATIONAL JOURNAL OF MARITIME TECHNOLOGY* 2019, *11*.
38. Nazri, F.M.; Saruddin, S.N.A. Seismic Fragility Curves for Steel and Reinforced Concrete Frames Based on Near-Field and Far-Field Ground Motion Records. *Arab J Sci Eng* 2015, *40*, 2301–2307, doi:10.1007/s13369-015-1758-y.
39. Zafarkhah, E.; Raissi Dehkordi, M. Extending the Modal Incremental Dynamic Analysis Method for Structures Equipped with Viscoelastic Dampers. *Journal of Vibroengineering* 2017, *19*, 783–800, doi:10.21595/jve.2016.17181.
40. BSN *SNI 1726:2019 Tata Cara Perencanaan Ketahanan Gempa Untuk Struktur Bangunan Gedung Dan Non Gedung*; Jakarta, 2019;
41. ASCE *Minimum Design Loads and Associated Criteria for Buildings and Other Structures*; American Society of Civil Engineers: Reston, VA, 2017; ISBN 9780784414248.
42. Irsyam, M.; Cummins, P.R.; Asrurifak, M.; Faizal, L.; Natawidjaja, D.H.; Widiyantoro, S.; Meilano, I.; Triyoso, W.; Rudiyanto, A.; Hidayati, S.; et al. Development of the 2017 National Seismic Hazard Maps of Indonesia. *Earthquake Spectra* 2020, *36*, 112–136, doi:10.1177/8755293020951206.
43. Stewart, J.P.; Seyhan, E. Semi-Empirical Nonlinear Site Amplification and Its Application in NEHRP Site Factors. *Pacific Earthquake Engineering Research Center* 2013.
44. Nagao, T.; Fukushima, Y. Source- and Site-Specific Earthquake Ground Motions. *Engineering, Technology & Applied Science Research* 2020, *10*, 5882–5888, doi:10.48084/etasr.3612.
45. Kim, D.K.; Park, H.G.; Sun, C.G. Design Earthquake Response Spectrum Affected by Shallow Soil Deposit. *Advances in Civil Engineering* 2019, *2019*, doi:10.1155/2019/4079217.

46. Nguyen, V.; Aaqib, M.; Nguyen, D.; Luat, N.; Park, D. A Site-Specific Response Analysis : A Case Study in Hanoi Vietnam. *Applied Sciences (Switzerland)* 2020, *10*.
47. Nagao, T. Maximum Credible Earthquake Ground Motions with Focus on Site Amplification Due to Deep Subsurface. *Engineering, Technology & Applied Science Research* 2021, *11*, 6873–6881, doi:10.48084/etasr.3991.
48. Nagao, T. Seismic Amplification by Deep Subsurface and Proposal of a New Proxy. *Engineering, Technology & Applied Science Research* 2020, *10*, 5157–5163, doi:10.48084/etasr.3276.
49. Smerzini, C.; Pitilakis, K.; Hashemi, K. Evaluation of Earthquake Ground Motion and Site Effects in the Thessaloniki Urban Area by 3D Finite-Fault Numerical Simulations. *Bulletin of Earthquake Engineering* 2017, *15*, 787–812, doi:10.1007/s10518-016-9977-5.
50. Hassan, H.M.; Fasan, M.; Sayed, M.A.; Romanelli, F.; ElGabry, M.N.; Vaccari, F.; Hamed, A. Site-Specific Ground Motion Modeling for a Historical Cairo Site as a Step towards Computation of Seismic Input at Cultural Heritage Sites. *Eng Geol* 2020, *268*, 105524, doi:10.1016/j.enggeo.2020.105524.
51. Chieffo, N.; Fasan, M.; Romanelli, F.; Formisano, A.; Mochi, G. Physics-Based Ground Motion Simulations for the Prediction of the Seismic Vulnerability of Masonry Building Compounds in Mirandola (Italy). *Buildings* 2021, *11*, 667, doi:10.3390/buildings11120667.
52. Paolucci, R.; Gatti, F.; Infantino, M.; Smerzini, C.; Güney Özcebe, A.; Stupazzini, M. Broadband Ground Motions from 3D Physics-Based Numerical Simulations Using Artificial Neural Networks. *Bulletin of the Seismological Society of America* 2018, *108*, 1272–1286, doi:10.1785/0120170293.
53. Seed, H.B.; Idriss, I.M. *Soil Moduli and Damping Factors for Dynamic Response Analyses*; Earthquake Engineering Research Center, Ed.; University of California: Berkeley, 1970;
54. Vucetic, M.; Dobry, R. Effect of Soil Plasticity on Cyclic Response. *Journal Geotecth Engineering* 1991, *117*, 89–107.
55. Hashash, Y.M.A.; Musgrove, M.I.; Harmon, J.A.; Ilhan, O.; Xing, G.; Groholski, D.R.; Phillips, C.A.; Park, D. *DEEPSOIL 7.0, User Manual*; Board of Trustees of University of Illinois at Urbana-Champaign.: Urbana IL, 2020;
56. Imai, T.; Tonouchi, K. Correlation of N Value with S-Wave Velocity and Shear Modulus. In Proceedings of the Penetration Testing, Proceedings of the second European symposium on penetration testing; Routledge: Amsterdam, February 12 1982; pp. 67–72.
57. Kramer, S.L. *Geotechnical Earthquake Engineering*; 1996;
58. Liang, Q.; Zhao, C.; Hu, J.; Zeng, H. An Analytical Method for Elastic Seismic Response of Structures Considering the Effect of Ground Motion Duration. *Appl. Sci* 2021, *2021*, 10949, doi:10.3390/app112210949.
59. Dobry, R., I.; Idriss, M.; Ng, E. Duration Characteristics of Horizontal Components of Strong-Motion Earthquake Records. *Bulletin of the Seismological Society of America* 1978, *68*, 1487–1520.
60. Shoji, Y.; Tanii, K.; Kamiyama, M. A Study on the Duration and Amplitude Characteristics of Earthquake Ground Motions. *Soil Dynamics and Earthquake Engineering* 2005, *25*, 505–512, doi:10.1016/j.soildyn.2004.11.033.
61. Barbosa, A.R.; Ribeiro, F.L.A.; Neves, L.C. Effects of Ground-Motion Duration on the Response of a 9-Story Steel Frame Building. In Proceedings of the 10th U.S. National Conference on Earthquake Engineering.; Anchorage ,AK, 2014.

62. Ou, Y.-C.; Song, J.; Wang, P.-H.; Adidharma, L.; Chang, K.-C.; Lee, G.C. Ground Motion Duration Effects on Hysteretic Behavior of Reinforced Concrete Bridge Columns. *Journal of Structural Engineering* 2014, *140*, 04013065, doi:10.1061/(ASCE)ST.1943-541X.0000856.
63. Romney, K.T.; Barbosa, A.R.; Mason, H.B. Developing a Soil Bridge- Interaction Model for Studying the Effects of Long-Duration Earthquake Motions. In Proceedings of the 10th U.S. National Conference on Earthquake Engineering; Anchorage , AK, 2014.
64. Mantawy, A.; Anderson, J.C. Effect of Long-Duration Earthquakes on the Low-Cycle Fatigue Damage in RC Frame Buildings. *Soil Dynamics and Earthquake Engineering* 2018, *109*, 46–57, doi:10.1016/j.soildyn.2018.01.013.
65. Chandramohan, R. Duration of Earthquake Ground Motion: Influence on Structural Collapse Risk And Integration in Design and Assessment Practice, Standford University, 2016.
66. Chiou, J.S.; Chiang, C.H.; Yang, H.H.; Hsu, S.Y. Developing Fragility Curves for a Pile-Supported Wharf. *Soil Dynamics and Earthquake Engineering* 2011, *31*, 830–840, doi:10.1016/j.soildyn.2011.01.011.
67. ZACCHEI, E.; LYRA, P.H.C.; STUCCHI, F.R. Nonlinear Static Analysis of a Pile-Supported Wharf. *Revista IBRACON de Estruturas e Materiais* 2019, *12*, 998–1009, doi:10.1590/s1983-41952019000500003.
68. Zacchei, E.; Lyra, P.H.C.; Stucchi, F.R. Pushover Analysis for Flexible and Semi-Flexible Pile-Supported Wharf Structures Accounting the Dynamic Magnification Factors Due to Torsional Effects. *Structural Concrete* 2020, *21*, 2669–2688, doi:10.1002/suco.202000137.
69. PLAXIS company (Plaxis bv) *PLAXIS CONNECT Edition V21.00 General Information Manual*; Delft, 2021; ISBN 9789076016276.
70. Toma, M.A. Earthquake Response Analysis of Pile Supported Structures Correspondence of PLAXIS 2D with Eurocode 8, Norwegian University of Science and Technology, 2017.
71. PLAXIS company (Plaxis bv) *PLAXIS CONNECT Edition V21.00-Material Models Manual*; 2021;
72. Dao, T.P.T. Validation of PLAXIS Embedded Piles for Lateral Loading, Delft University of Technology, 2011.
73. Kwaak, B. van der Modelling of Dynamic Pile Behaviour during an Earthquake Using PLAXIS 2D: Embedded Beam (Row), Delft University of Technology, 2015.
74. Sluis, J.; Besseling, F.; Stuurwold, P.; Lengkeek, A. Validation and Application of the Embedded Pile Row Feature in PLAXIS 2D. *Plaxis Bulletin, issue 34/Autumn 2013* 2013, 10–13.
75. Bowles, J.E. *Physical and Geotechnical Properties of Soils*; McGraw-Hill Education, 1984; ISBN 0070661944.
76. Obaji, N.O.; Komolafe, O.O.; Oke, J.A. Prediction of Initial Void Ratio from the Natural Moisture Content of Cohesive Soils. *Uniabuja Journal of Engineering and Technology* 2020, *1*, 1–13.
77. Benz, T. Small-Strain Stiffness of Soils and Its Numerical Consequences, 2007.
78. Broms, B.B. Lateral Resistance of Piles in Cohesive Soils. *Journal of the Soil Mechanics and Foundations Division* 1964, *90*, 27–63, doi:10.1061/jsfeaq.0000611.
79. Décourt, L. Prediction of the Bearing Capacity of Piles Based Exclusively on N Values of the SPT. In *Penetration Testing*; Routledge, 1982; p. 6 ISBN 9780203743959.

80. Décourt, L.; Quaresma, A. Capacidade de Carga de Estacas a Partir de Valores de SPT. *Congresso Brasileiro de Mecânica dos Solos e Engenharia de Fundações* 1978, 5–53.
81. Boyke, C.; Refani, A.N.; Nagao, T. Site-Specific Earthquake Ground Motions for Seismic Design of Port Facilities in Indonesia. *Applied Sciences (Switzerland)* 2022, *12*, doi:10.3390/app12041963.
82. Boore, D.M. *TSPP A Collection of FORTRAN Programs for Processing and Manipulating Time Series*; 2009;
83. Hirai, H. A Winkler Model Approach for Vertically and Laterally Loaded Piles in Nonhomogeneous Soil. *Int J Numer Anal Methods Geomech* 2012, *36*, 1869–1897, doi:10.1002/nag.1078.
84. Tokimatsu, K.; Asaka, Y. Effects Of Liquefaction-Induced Ground Displacements On Pile Performance In The 1995 Hyogoken-Nambu Earthquake. *Soils and Foundations* 1998, *38*, 163–177, doi:10.3208/sandf.38.Special_163.
85. Tamura, Y. Amplitude Dependency of Damping in Buildings and Critical Tip Drift Ratio. *International Journal of High-Rise Buildings* 2012, *1*, 1–13.
86. Smith, R.; Merello, R.; Willford, M. Intrinsic and Supplementary Damping in Tall Buildings. *Proceedings of the Institution of Civil Engineers: Structures and Buildings* 2010, *163*, 111–118, doi:10.1680/stbu.2010.163.2.111.
87. Iwashita, K.; Hakuno, M. Damping Coefficient of Structural Foundation Analyzed By 3-D Fem With Non-Reflecting Boundary. *Structural Eng./Earthquake Eng.* 1987, *4*, 233–236, doi:10.2208/jscej.1987.380_259.
88. Association, J.R. *Specifications for Highway Bridges, Part V Seismic Design*; 2019; Vol. 228;.
89. CSI SAP2000 Integrated Solution for Structural Analysis and Design. *Computers & Structures Inc* 2016, 556.
90. Isenhower, W.M.; Wang, S. *User's Manual for LPile 2018*; 2018;
91. Matlock, H. Correlations for Design of Laterally Loaded Piles in Soft Clay. In Proceedings of the Proceedings of the Annual Offshore Technology Conference; Houston, Texas, 1970; Vol. 1970-April, p. No. OTC 1204,577-594.
92. Terzaghi, K.; Peck, R.; Mesri, G. *Soil Mechanics in Engineering Practice*; John Wiley and Sons Inc: New York, 1996; ISBN 978-0-471-08658-1.

Doctoral Dissertation, Kobe University
“Seismic Performance Evaluation Method of Wide Pile-Supported Wharfs Considering Kinematic and Inertial Forces”, 87 pages
Submitted on July, 12, 2023